ELECTRON MOBILITY AND SCATTERING IN COLD, DENSE HELIUM^4 AND HYDROGEN GASES

by

Harold Roger Harrison

A dissertation submitted in partial fulfillment
of the requirements for the degree of
Doctor of Philosophy
(Physics)
in The University of Michigan
1971

Doctoral Committee:

Assistant Professor Brian E. Springett, Chairman
Professor Chihiro Kikuchi
Professor Oliver E. Overseth
Professor T. Michael Sanders, Jr.
Professor Jens C. Zorn

ABSTRACT

ELECTRON MOBILITY AND SCATTERING IN COLD, DENSE HELIUM^4 AND HYDROGEN GASES

by

Harold Roger Harrison

Chairman: Brian E. Springett

We have made measurements of electron mobility in helium-4 at temperatures from 4.2-300K, and at densities up to 30×10^{20} cm^{-3}, and in normal hydrogen at temperatures from 26.0-31.7K, and at densities up to 45×10^{20} cm^{-3}. Measurements were made by a single-gate switching technique with the current-frequency curves traced directly by a chart recorder.

The data in helium-4 extend our knowledge of the systematics of electronic bubbles in that species. The data in normal hydrogen were severely restricted by the maximum density obtainable in the gas phase below the critical temperature (33.2K). Data at the 31.7K isotherm in particular showed the coexistence of two species, differing in mobility by a factor of 10^3, over an appreciable range of density. This is in complete contrast to the data in helium-4, which never exhibit two species of different mobility simultaneously.

The data are discussed in the light of published theories of electron transport in random systems and of electronic bubbles. A new bubble model potential $U=-U_o/\cosh^2(r/r_o)$ is presented and it is shown that a reasonable explanation of the data can be obtained, although the theoretical fit to the data shows that our understanding of the problem is still incomplete.

Suggestions for further experiments are presented which are aimed at elucidating some of the difficulties arising out of the present work.

ACKNOWLEDGMENTS

I wish to express my appreciation in particular to Professor B.E. Springett for his assistance and patience throughout all phases of this work, both experimental and theoretical. He has given far more of his time than could ever have been reasonably asked.

I would like to thank Professor T.M. Sanders for his bringing to our attention the new bubble model treated in this thesis, as well as for numerous other suggestions. Thanks are also owed to Professor L.M. Sander for his great assistance in developing the theory of this new bubble model. I would also like to thank Mr. L. Thurston for his fine draftsmanship of the figures, and the members of the Physics Instrument Shop and the Physics Student Shop for their assistance in the construction of apparatus.

Special thanks are due my family for their continued support through all the years of my graduate training.

The support of the bulk of this work by the United States Atomic Energy Commission is gratefully acknowledged. Funds for a germanium thermometer and for partial fellowship support from the Rackham School of Graduate Studies of the University of Michigan is also acknowledged.

Cattle die, kinsmen die,
one day you die yourself;
but the words of praise will not perish
when a man wins fair fame.

—Odin

in Sayings of the High One

TABLE OF CONTENTS

LIST OF TABLES AND FIGURES

I. INTRODUCTION

The interaction of electrons with simple systems (all of the parameters of which are known) is a problem of considerable physical importance, both for its own sake, and for the light it sheds on the interaction of electrons with more complicated systems such as metal-ammonia solutions or alkali atom-rare gas mixtures. This particular study is concerned with the simple non-polar gases helium-4 and hydrogen. The interaction between them and electrons is probed by measuring the electron mobility, the mobility being defined by

$$\mu = \lim_{\mathcal{E}\to 0} v_d/\mathcal{E} \qquad (1\text{-}1)$$

where v_d=drift (steady state) velocity
$\mathcal{E}$=applied electric field

The electron mobility in helium-4 gas has previously been measured over a narrow range of temperatures near the boiling point by Levine and Sanders.[1,2] They observed a departure from the kinetic theory prediction of three or four orders of magnitude. They explained their data qualitatively in terms of the bubble model, discussed by other workers in connection with electrons[3] and positronium[4] in <u>liquid</u> helium and other systems. (Note that the data for positive ion mobility, on the other hand, has been successfully interpreted on the basis of clusters of atoms, formed by induced polarization arising from the initial charged ion. The electron's behavior is qualitatively different because, being so much lighter than an atom, or even a proton, its zero-point energy is significantly larger.)

In this thesis, I will present more extensive data (covering a wider temperature range mainly) of electron mobility in helium-4 gas, which reveal more clearly the systematics of the problem. I also will

present data of electron mobility in hydrogen gas at low temperatures and high densities. These latter data show two distinct branches, separated by about three orders of magnitude, a totally unexpected phenomenon. These data are presented after a chapter on the experimental apparatus and measurement techniques used. (Note that hydrogen was picked for study to test the theory of Springett, Jortner, and Cohen,[5] a theory which predicts whether bubbles will be observed in a particular non-polar fluid or not. It was planned to study neon as well, the other gas besides helium-4 and hydrogen predicted to have electronic bubbles,[5,6] but time did not permit.) I have not attempted to give a full and detailed treatment of all of the experimental aspects of this study; rather, I have skipped what is common to most low temperature experiments (things which are covered much better than I could hope to treat them in books on low temperature techniques[7,8]) and discussed only what is peculiar to mine. In the chapter on theory, I will review some scattering theories and the spherical square well bubble model, and present a treatment of a new bubble model potential. Thanks largely to the work of Levine,[2] it is now pretty well accepted that the bubble model (for electrons only) is substantially correct, and so it is not necessary to consider alternative explanations such as cluster ions or impurity ions in the case of helium-4. The predictions of these theories will be compared with experimental results (one curve only needs to be considered). Also some remarks will be made about the very different sort of electron behavior in hydrogen, and possible explanations will be presented for that data (that is, whether the low mobility object is a bubble or not).

Finally, in the concluding chapter it will be noted that this

thesis raises at least as many questions as it answers. Suggestions will be made there on experiments that might next be performed.

II. EXPERIMENTAL APPARATUS AND MEASUREMENT TECHNIQUES

2.1 The Electron Source

2.1.1 Attempted Use of Cold Cathodes

The first problem to be considered in any experiment involving charged particles is, what is to be the source of these charged particles? There are several possible ways for generating electrons in experiments involving insulating materials, namely

(i) Thermionic emission from a hot wire,
(ii) Field emission from a cold metal,
(iii) Photo-electron emission,
(iv) Cold cathodes,
(v) Radioactive sources.

I will not comment on thermionic emission, as it is not generally considered to be very practical for low temperature experiments. Field emission has the drawback that very intense electric fields (about 10^3-10^4 V/cm) are required to produce an appreciable current, thus requiring extremely good shielding from the rest of the apparatus (all in the space of a few centimeters) which typically operates at electric field strengths lower by a factor of perhaps 10^2-10^3 or even more. However, McClintock[9] has produced large currents (about 10^{-7} amperes, compared to 10^{-14}-10^{-12} amperes from a radioactive source) in liquid helium by field emission; also, the electrons come from a point source. Clearly, for some experiments this method is essential, despite the shielding problems in the experimental cell. The photo-electric effect has been used in experiments[1,2] that require the ability to carefully control the electron energy. For these experiments, this method, despite its difficulties, may be essential. Obvious difficulties are the careful fabrication techniques needed and the provision of a means for light to enter a sealed apparatus inside

a dewar (although the use of light-emitting diodes might get around this latter problem[10]). Also, precautions are necessary to insure great purity of the gases used to avoid poisoning of the photo-surfaces.

Metal-insulator-metal cold cathode tunnel junctions are now being used by a number of workers. (Silver and his colleagues are using them to study the processes involved in thermalization of the electrons after they are injected into liquid helium,[11] for example.) There are several advantages over radioactive sources (discussed in the next section):

(i) The electrons are emitted with only a few eV of energy, not several KeV (or even MeV) as is the case with alpha, beta, or gamma radiation. The high energies from radioactive sources lead to two potential problems--(1) generation of many species in the fluid, such as ions, atoms, or molecules in very highly excited states, and (2) for beta particles, for example, there may be an appreciable range before thermalization takes place.

(ii) There would be no problems with handling radioactive materials.

(iii) The device could be switched on and off; however, the switching speed will be severely limited because the cold cathode is a capacitor-like structure, with C≈1000 pf, typically.

(iv) Under optimum conditions, a cold cathode can deliver electron currents some orders of magnitude larger than those produced by a typical radioactive source. Thus, many of the problems associated with working with a small electron source current (problems discussed later in this chapter), which take a large fraction of the experimenter's time, could be avoided.

Along with the above advantages is the problem that the manufacture and operation of cold cathodes is still something of a black art rather than a science, although this is rapidly changing. We manufactured Al-Al_2O_3-Au cold cathodes by evaporating aluminum and gold in a metals evaporator of standard design. The Al_2O_3 was formed by anodizing the base layer of aluminum to the desired thickness; Formvar was painted along the edges where the layers became thin to

prevent electrical breakdown. Now there are two currents to be considered in the operation of cold cathodes, the circulating current and the emission current. The circulating current is just the usual current flowing in an electrical circuit, the circuit in this case consisting of a driving voltage and the cold cathode (which acts as a resistive element, but one whose I-V characteristic is highly non-linear, and which in fact exhibits negative resistance over some voltage ranges). The emission current is that small fraction of the circulating current which passes directly through the top gold layer and outside of the cathode structure into space, rather than returning to the battery along the wire connected to the gold layer. Circulating currents are usually of the order of milliamperes (after the device has undergone the process known as "forming" which appears to involve the injection of traps between the valence and conduction bands of the insulator, these traps then providing the means for electrons to hop, or tunnel, from one trap to the next and finally to get through the insulator). Figure 1 shows the forming process taking place in a cold cathode operated at 77K. For this case, the circulating current is of smaller magnitude than usual, but at the end of the last trace is an illustration of another problem, that of catastrophic breakdown to a much lower impedance state. Emission currents are naturally much smaller, and vary widely in their magnitude, but they are generally of the order of nanoamperes. Figure 2 shows both circulating and emission currents, measured simultaneously, for a cold cathode operated at 4.2K. Notice that the emission current is rising exponentially with applied voltage. (No emission current was detected below about 5 volts.) No attempt has been made in this plot to show the noisiness of the emission, but it is

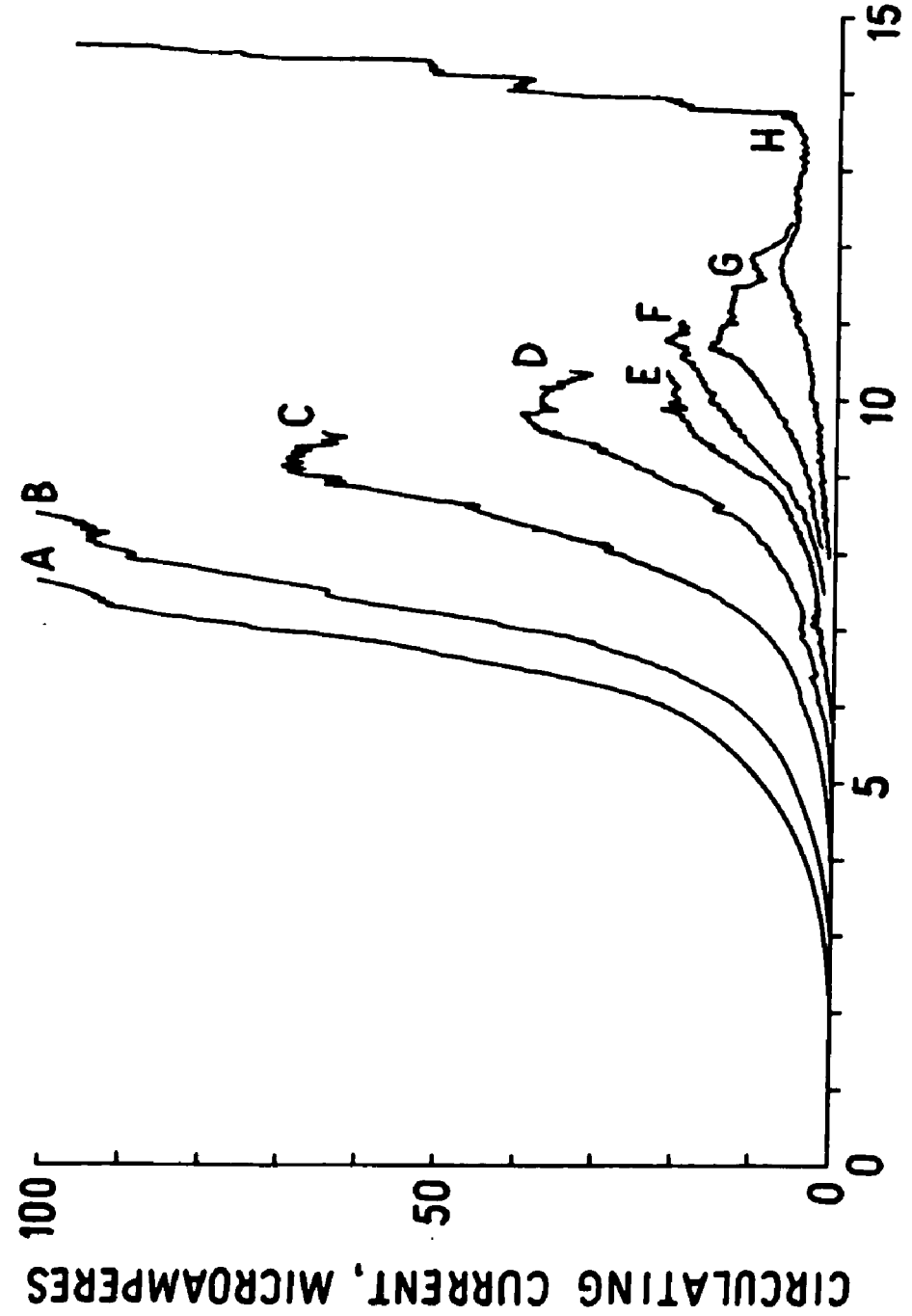

Fig. 1: Draftsman's copy of circulating current versus applied voltage for a cold cathode operated at 77K. Curves traced successively in the order A-H, illustrating the "forming" process. (Pen lifted and applied voltage switched off at the end of each trace.) Notice the catastrophic breakdown at the end of trace H.

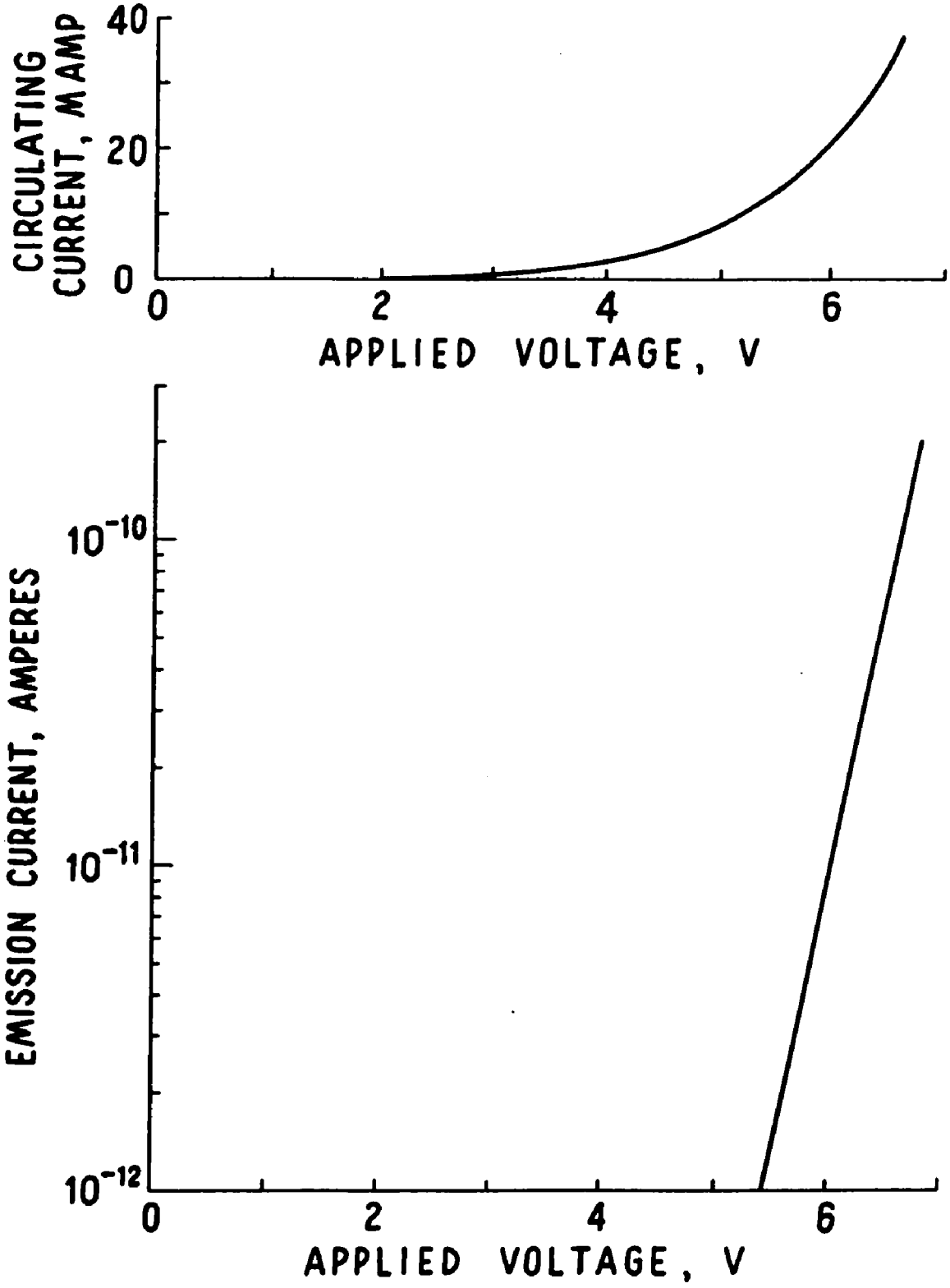

Fig. 2: Draftsman's copy of two simultaneous recorder tracings--circulating and emission currents versus applied voltage for a cold cathode at 4.2K. (Note the differences in the current scales.)

pretty easy to see that the basic practical problem as far as using this emission current of electrons in an actual experiment is this unsteadiness of the current (coupled with a very steep I-V characteristic), even when the voltage across the device is held constant. The cathode may also switch from a state of low impedance back to its initial high impedance state (reversing the forming process, that is) and back again (with consequent drastic changes in the emission current) in what often seemed an incomprehensible fashion. The cold cathode could finally burn out from Joule heating, especially if operated in a DC mode. The only thing very different that we tried in these experiments that had not been done before (to our knowledge) was to manufacture and operate cold cathodes of about 1 cm^2 active area (as compared to perhaps 1 mm^2 active area used by other workers). In addition to the usual components of a cold cathode, we also evaporated some fairly thick (750Å) gold stripes on top of the other layers, in order to equalize the electrical potential across the whole expanse of the gold surface, the "valleys" between them being the sites for emission. (Calculations for the very thin original gold layer indicated a resistance great enough so that the magnitudes of circulating currents we were seeing could have made this a real problem.) After the cold cathode had ceased to operate, it was found that some of the gold had been removed somehow, and not the thin "valleys" where emission presumably took place, but the much thicker stripes, so that one could see through where they had been. Many of these problems which we encountered are discussed in references 12-18; in particular, reference 13 gives a very lucid discussion of the phenomena taking place. For the above reasons, we finally decided to use a radioactive source. We now know that proper "breaking-in" or

ageing of a new cathode is the apparent key to successful operation. The applied voltage on the cold cathode should be increased only very slowly, allowing the cold cathode to come to equilibrium at each new voltage. It is necessary to go slower and slower as the voltage is increased, the whole process taking an hour or more. Then the cold cathode is ready for operation.[19] Also, this process and the other effects mentioned above are all temperature dependent. In particular, breakdowns occur at lower applied voltages the higher the operating temperature. Thus, if it is desired to operate them at low temperatures it seems that one should not test them at room temperature beforehand.

2.1.2 Radioactive Source

The electron source actually used in this experiment was tritium (a beta$^-$ producer) embedded in titanium, forming titanium hydride. Approximately 2,500Å of gold was deposited on this source. Details of the electron energy spectra before and after the gold plating are discussed in Appendix I. The result of calculations presented there is that the number density required to stop all the emitted electrons before the first grid of the experimental cell is $.450 \times 10^{20}$ cm^{-3} for helium and $.375 \times 10^{20}$ cm^{-3} for hydrogen. In general the data I present in the next chapter meet this criterion, but occasionally not. The low density end of the data curves are generally the most unreliable anyway (see subsection 3.1.2 for a discussion of errors).

Another benefit of the gold plating of the source is that any question of hydrogen (when that gas was in the cell) replacing some of the tritium in the titanium hydride can be ruled out as an explanation for any of the experimentally observed effects. (These effects

are discussed section 3.2.)

2.2 Experimental Apparatus

Figure 3 is a scale drawing of the cylindrically symmetric experimental cell. The insulating spacers are made of nylon; the metal part are of brass, except the grids themselves, which are of copper (82±2% transmission, 100 lines/inch, made by the Buckbee Mears Co.). The grids were soldered onto the grid holders, and then all metal parts were gold plated in an Atomex solution. The system is held together by long nylon pegs and brass bolts (omitted in Figure 3). The only noteworthy feature of the system is the collector and its guard ring, due to Ihas and Ryan.[20] The collector is a brass piece soldered onto the center pin of a Microdot connector, which in turn is soldered onto the guard ring. This whole assembly was then gold plated as were the other metal parts, but the gold did not plate onto the teflon insulation of the Microdot connector. A Microdot cable screwed onto the threaded end of the Microdot connector, which projects through a hole in the bottom of the guard ring.

Upon cooling from room temperatures to very low temperatures, nylon shrinks about 1.4% and brass shrinks about .375%.[21] It is the inner brass sleeves and nylon spacers that are of importance in this connection; the thick outer nylon sleeves are actually made a slight bit shorter than the inner sleeves (this difference is not shown in Figure 3). Thus, length changes due to temperature changes are probably not more than 0.5%. However, this is probably negligible compared with other uncertainties in the length measurements: buckling of the grids during soldering and the fact that electrons can move through the apparatus at some shallow angle with respect to the central

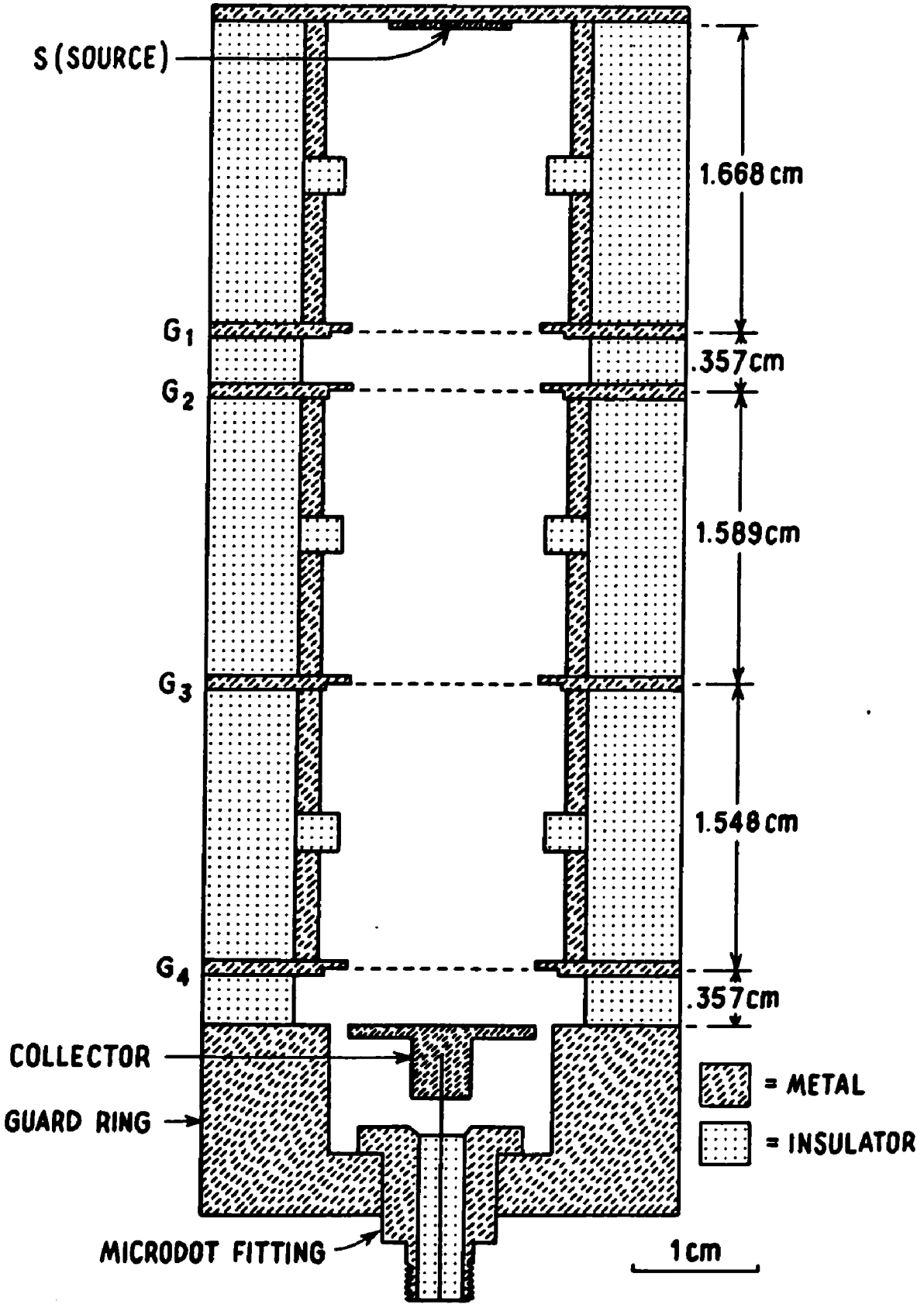

Fig. 3: Scale drawing of the experimental cell.

axis and still be collected.

The experimental cell is suspended from the lid of a sealed can by a nylon holder (see Figure 4). A germanium resistance thermometer is mounted in this nylon holder. The Microdot cable from the collector is attached (inside the sealed can) to a stiff Uniform Tubes coaxial cable of stainless steel (solid inner conductor and solid tubing outer conductor) which runs from the can up to the dewar head. A drop of Stycast epoxy was put on the end of the coaxial cable to prevent vacuum leaks between the inner and outer conductors and the insulator in between. A metal sleeve over the joint between the Microdot and stainless coaxial cables serves as an electrical shield. Manganin wires (for small heat leaks) carry the various grid biasing voltages from the dewar head to the can, and are fed into the can by means of home-made feed-throughs. (The wires come into the dewar head through hermetically sealed Amphenol connectors, just as the collector cable is fed out of the dewar head through a hermetically sealed BNC connector.) These feed-throughs consist of stainless steel tubing, about 1/8" in diameter and 1" or more long, which is sandblasted so that the epoxy to be applied will stick better. They are then tinned with a solder of low melting temperature (like Cerrolow, which melts at either 117°C or 136°C depending on which solder you have). Perhaps 8 to 12 short enameled copper wires are twisted together and epoxied (Stycast again) into the tube. After the epoxy has hardened, the tube is soldered (again with low melting solder) into the can lid.

2.3 Method of Temperature Measurement and Control

2.3.1 Temperature Measurement

Temperature was measured with a Cryocal germanium resistance

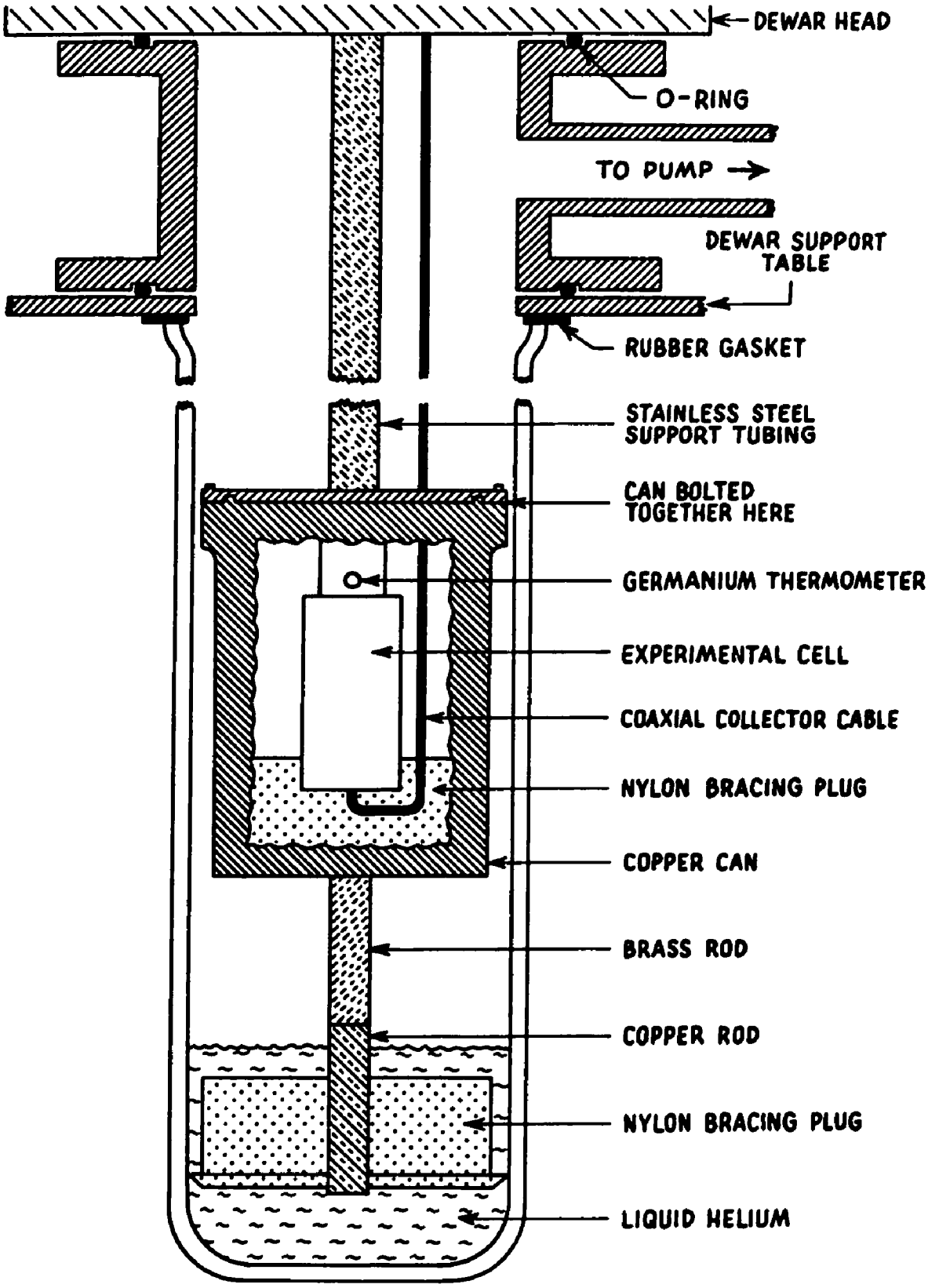

Fig. 4: Schematic representation of the apparatus (not to scale). Not shown: outer liquid nitrogen dewar, bolts, and electrical leads.

thermometer. The resistance was determined by a 4-terminal measurement. A Doric DS-100 K5 four and a half figure digital microvoltmeter read the voltage across the thermometer. The current through the thermometer was supplied by a 1½ volt battery, current limited by precision resistors ranging from 15 Kohms to 4 Megohms in six steps. The current was determined from a knowledge of the current limiting series resistor and a measurement of the voltage across it (measured by a Non-Linear Systems Series X-3 (Model A) digital multimeter). In spite of these precautions to incure an accurate measurement, thermo-electric emf's were seen, usually not more than 10 microvolts and often less. This would correspond to an error in temperature of something like 1% in the worst cases. The details of our calibration of this thermometer are given in Appendix II.

2.3.2 Temperature Control

Temperature control was achieved in perhaps the simplest possible fashion. The basic idea is that of heat balance. The can is held at a certain temperature, above that of the liquid helium (say 20K) but much less than room temperature. (The fact that the can is suspended from the dewar head--which is at room temperature--by stainless steel tubing, an alloy of very low thermal conductivity, makes this possible.) The sealed can (sealed with an indium wire O-ring and bolted shut) containing the experimental apparatus was constructed of copper to insure that there would be no temperature gradients along it (or at least very small ones) even though there might be such temperature gradients outside the can. A rod extended from the bottom of the can into a pool of liquid helium at the bottom of the dewar. The upper part of the rod (entirely out of the liquid helium) was of brass; the lower

part of the rod (partially immersed in liquid helium) was of copper. The copper part of the rod is essentially at the temperature of the liquid helium, no matter how much liquid helium is left. Virtually the entire temperature drop between the liquid helium and the can is along the brass part of the rod (see Figure 4). This type of system is described in reference 22. A quantitative calculation for the design of such a system is presented in Appendix III.

A length of manganin wire was wrapped around the outside of the can to serve as a heating element. The heater current was supplied by a hand-controlled variac. Surprisingly, very good temperature stability could be maintained in this fashion. (See the next chapter for values of temperature variation.) The characteristic time for a temperature change of the size specified in Table I seemed to be several seconds at worst, which made this technique possible.

The same experimental arrangement was used for measurements on a fixed mass of gas in the can and associated tubing (nearly constant density). A very small amount of liquid helium was transferred into the dewar, and a typical run (discussed in the next chapter) would take several hours in going from roughly 4.2-40K, allowing time for many mobility measurements, each at essentially constant temperature.

2.4 Pressure Measurement and Calculation of Number Densities

Pressures above one atmosphere were measured with an old Ashcroft Test Gauge, with subdivisions every 2 p.s.i. This gauge was calibrated against a good Wallace & Tiernan gauge, Model No. FA 233, 0-500 p.s.i. absolute, with subdivisions every .5 p.s.i. (and independently calibrated), and the Ashcroft gauge was found to be accurate to about 1 p.s.i. over its whole range. Below one atmosphere, pressure

was measured with a Marsh Instrument Co. Test Gauge, Type 28, with subdivisions every .10" of Hg.

Pressures measured ranged from essentially vacuum to almost 20 atmospheres. Naturally the accuracy of the measurement was highest at the highest pressures since the precision or absolute uncertainty was the same for all measurements (for either gauge). The apparatus was not originally designed to work above one atmosphere, and not surprisingly some problems developed. The sealed can leaks at these high pressures where it is bolted together by 2-56 stainless steel screws, but apparently this caused no great harm--gas could simply be allowed to flow through at a slow rate. I found that ordinary toggle valves are pushed open at about 20 atmospheres, so all such valves had to be replaced by needle valves.

Number densities were calculated for helium-4 gas from

$$P = \rho kT (1 + B_1 \rho) \qquad (2\text{-}1)$$

where ρ=number density and B_1=second virial coefficient. Values of the virial coefficient were taken from reference 23 to 60K and I extrapolated to 77K, and reference 24 for a room temperature value. Number densities for hydrogen were calculated using empirical equations and constants from reference 25. Virial coefficients for hydrogen, if desired, can be derived from constants found in reference 26. (This reference also has a nice phase diagram for hydrogen.)

2.5 Gases Used

Ordinary tank gas (99.99% pure for hydrogen, 99.998% pure for helium), run through a liquid nitrogen cooled molecular sieve was found to be adequate. (In one instance, to be noted later, ultra-pure hydrogen was used to check that what was being observed was not due

to impurities.) In fact, it is not even certain that the molecular sieve was necessary, but it was an item of "insurance" that was easy to hook up. In addition to prolonged pumping, the can and associated piping lines were usually flushed twice with the gas that was going to be studied next. The fact that no special precautions were necessary to ensure great purity is in contrast to the work of Levine and Sanders,[1,2] but their problem was with poisoning of a delicate photocathode surface, an item not present in my experiment.

I might note that when the system was first put together, the piping lines were not adequately sealed against leaks, and so had impurities in them. When the can was opened to these lines, in order to let in more gas, the signal could immediately be reduced to zero, so presumably impurities of any appreciable concentration would be detected by this effect.

2.6 Control of Mechanical Vibrations

Perhaps the greatest technical problem with my experiment was the level of signal strength, of the order of 10^{-14}-10^{-12} amperes, and the consequent need to reduce noise (whether electrical or mechanical in origin) to an absolute minimum. Ordinary electrical shielding precautions were taken, but noise still remained a major problem, so steps were taken to reduce noise which has its origin in various mechanical vibrations (and which by some transducer action was converted into electrical noise).

The operational amplifier (see the next section about the measurement set-up) sits on a steel plate, which sits on a piece of foam rubber, which in turn sits on a brick pillar, right next to the dewar system, and of about equal height so that the low-noise coaxial

cable connecting the amplifier to the dewar head could be as short as possible. The operational amplifier circuit was constructed so that internal vibration of components and leads was kept to a minumum. The coaxial collector running from the dewar head to the apparatus can was braced against the center stainless steel tubing at several points. The apparatus can, at the end of the long stainless steel tube, is a cantilevered structure; the experimental cell itself inside the sealed apparatus can is also mounted in a cantilevered position, as shown in Figure 4. Both of these structures were braced, reducing most of the vibrations. The experimental cell was braced inside the apparatus can by a large nylon plug which filled the bottom of the can and which gripped the guard ring on the experimental cell as well. (A cut was made to allow the Microdot collector cable to pass through.) The whole system was braced by a nylon plug, almost as large as the dewar diameter, which was attached to the rod hanging down from the can. A circular piece of nylon sheet, with cuts along the edge to allow liquid helium to flow through unimpeded, was beveled at the edge and attached to the heavy nylon plug. The edge of this sheet pressed against the dewar wall.

Finally, it was found that the liquid nitrogen boiling in the outer dewar of a standard double dewar pair was sufficient to cause a large amount of noise over at least some of the ranges of experimental conditions at which data were taken. Following Schofield,[27] a flange was made to seal off the outer dewar and yet allow the inner liquid helium dewar to pass through it. The liquid nitrogen was then pumped down to a temperature near its triple point (63.15K), nitrogen gas was let in above the liquid to a pressure of one atmosphere, and a vent to

the atmosphere was left open. The nitrogen would remain undisturbed by boiling for about 1½ to 2 hours, at which time the data taking could be stopped for a few minutes and the above process repeated. Figure 5 shows two curves of signal strength versus frequency, taken under identical conditions except that the upper one was taken while the liquid nitrogen in the outer dewar was boiling, and the lower one while it was still.

2.7 Electronics and Basic Techniques for the Mobility Measurements

We are interested in measuring electon mobilities in this experiment, where mobility is defined as $\mu = \lim_{\mathcal{E}\to 0} v_d/\mathcal{E}$, where v_d is a terminal drift velocity and $\mathcal{E}$ is the applied electric field. The technique we used for all measurements was the single-gate technique. Double-gate switching and time-of-flight measurements are other possible techniques which can be used, but carefully applied, the single-gate technique gives almost as accurate results, since the limiting accuracy is mainly determined by the geometry of the experimental cell in each of the three mentioned cases. As will be seen in the next chapter, the actual measured values of mobility span a range of 10^5, with corresponding ranges for the cut-off frequency f_c and τ_d, the time to cross the drift region. As might be expected, no one method is best over this whole range. The time-of-flight method is best for low mobilities and long transit times, whereas gating methods (single or double) are best for the high mobilities and short transit times.

The basic equation for the mobility measurements is easily derived.[28] (Northby[28] uses Gunsolo[29] as his source.) The result is

$$I(f) = \frac{I_0}{2}\left(1 - f/f_c\right) \qquad (2\text{-}2)$$

where

$$f_c = \frac{\mu V_i}{2L^2}, \quad \text{or} \quad \mu = \frac{2L^2}{V_d} f_c \qquad (2\text{-}3)$$

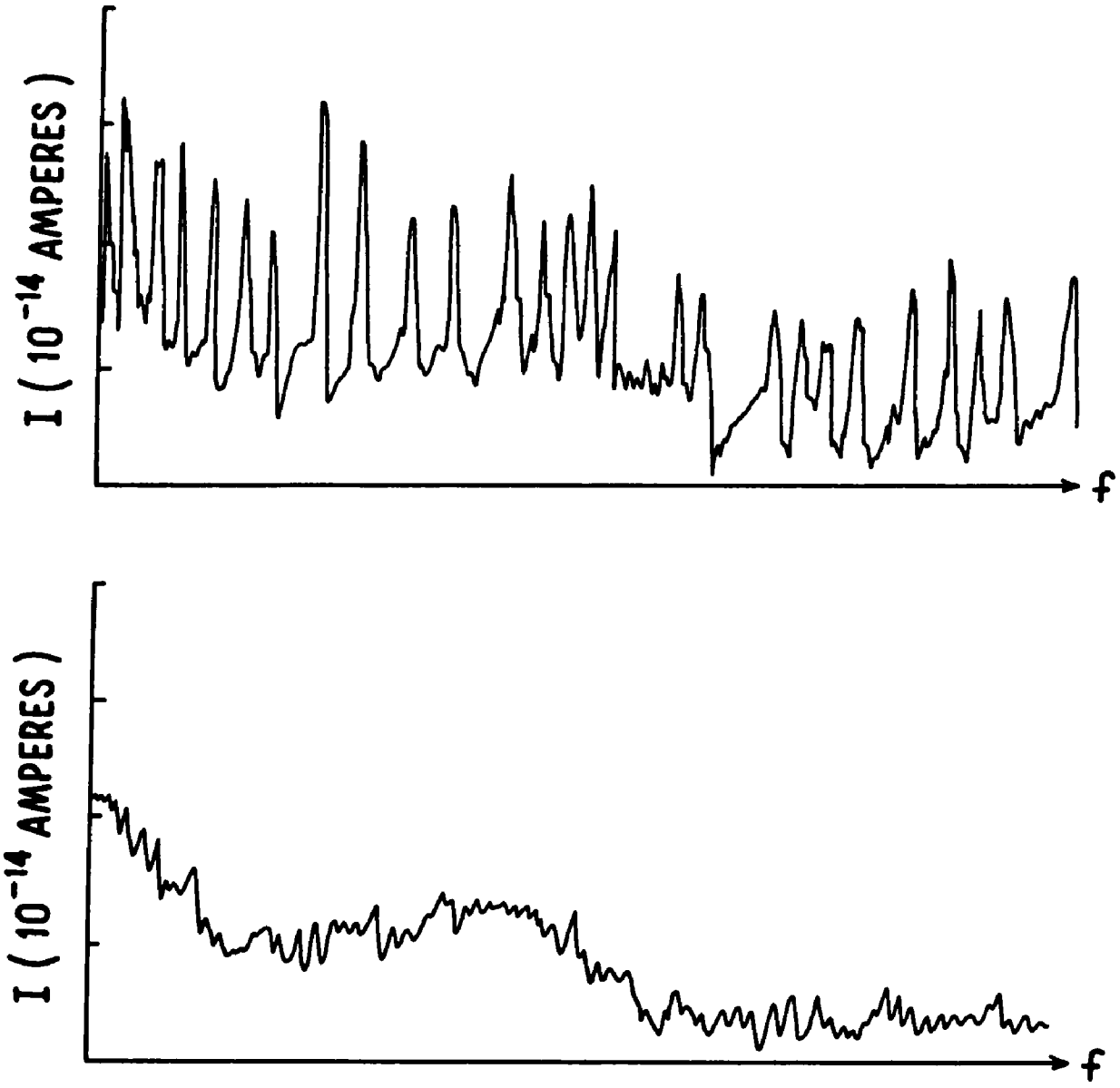

Fig. 5: Draftsman's copy of two recorder traces, the second made immediately after the first. Conditions for the two are identical, except that liquid nitrogen is boiling in the outer dewar for the first but not for the second. The frequency range is approximately .50-7.00 KHz (linear scale). The curves were taken in helium-4 at 77K. Note that the zero of I(f) is shifted for clarity.

and μ = electron mobility
V_d = voltage across the drift region
L = length of the drift region

The physical process behind the derivation is illustrated in Figure 6 and needs little comment.

Figure 8 is a block diagram of the whole experimental set-up. The dewar is liquid nitrogen-liquid helium double dewar system of standard design, with a slit in the silvering to look inside, and of nominal two-inch inner diameter. The ramp voltage generator and the grid biasing circuit are home-made; all the other electronic apparatus is commercially-made, as indicated. There are two items to note concerning the experimental set-up:

(i) The frequency of the square waves from the function generator is linear with the applied controlling voltage from the ramp voltage generator. Thus, if this same voltage is fed to the x-axis of an x-y chart recorder, the x-axis will effectively be a linear frequency axis. (This is true whether or not the ramp voltage generator's output voltage increases perfectly linearly with time or not.) The frequency counter is then used for calibration of this axis. The oscilloscope is to measure the amplitude of the square waves, and to check on any distortions. (It was found that up to about 10 KHz there was very little distortion, but that it had become quite serious by 100 KHz, thus contributing to the error at the high mobility end of each experimental curve.)

(ii) The null voltmeter that follows the operational amplifier (shown in Figure 7--the 27 ohm-33 microfarad system serves to filter out any pickup coming in along the $\pm$15 volt lines) serves principally as a low noise filter and impedance match. It also serves as a variable, low-gain "post" amplifier.

In operation, the square waves are applied (on top of a DC bias voltage) to both S and G_1 (see Figure 3). Thus, the voltage between S and G_1 remains constant; only the voltage between G_1 and G_2 was stepped up and down, and G_1-G_2 becomes the drift region. (The DC bias level of G_1 was higher than that of G_2 in order to achieve a clean cut-off of the current.) (Occasionally other grid pairs were used as the drift region,

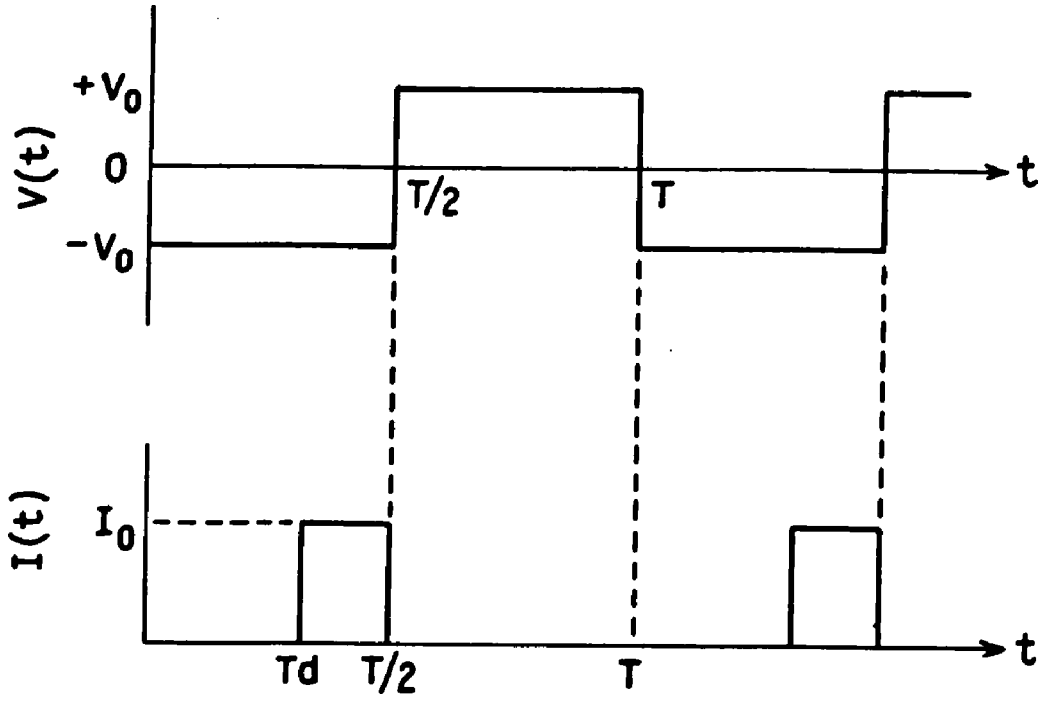

Fig. 6: Current coming from the drift region, driven by a square-wave voltage. τ_d=drift time across the drift region.

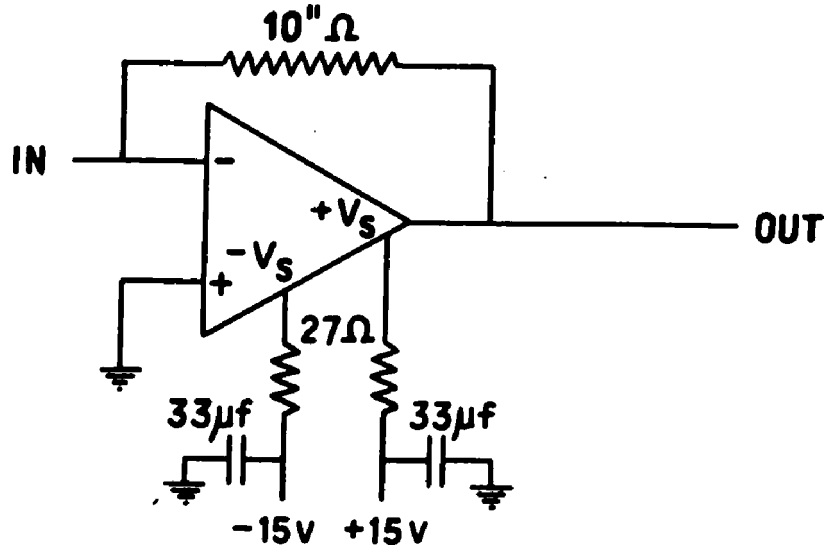

Fig. 7: Operational amplifier (Analog Devices 310J) circuit.

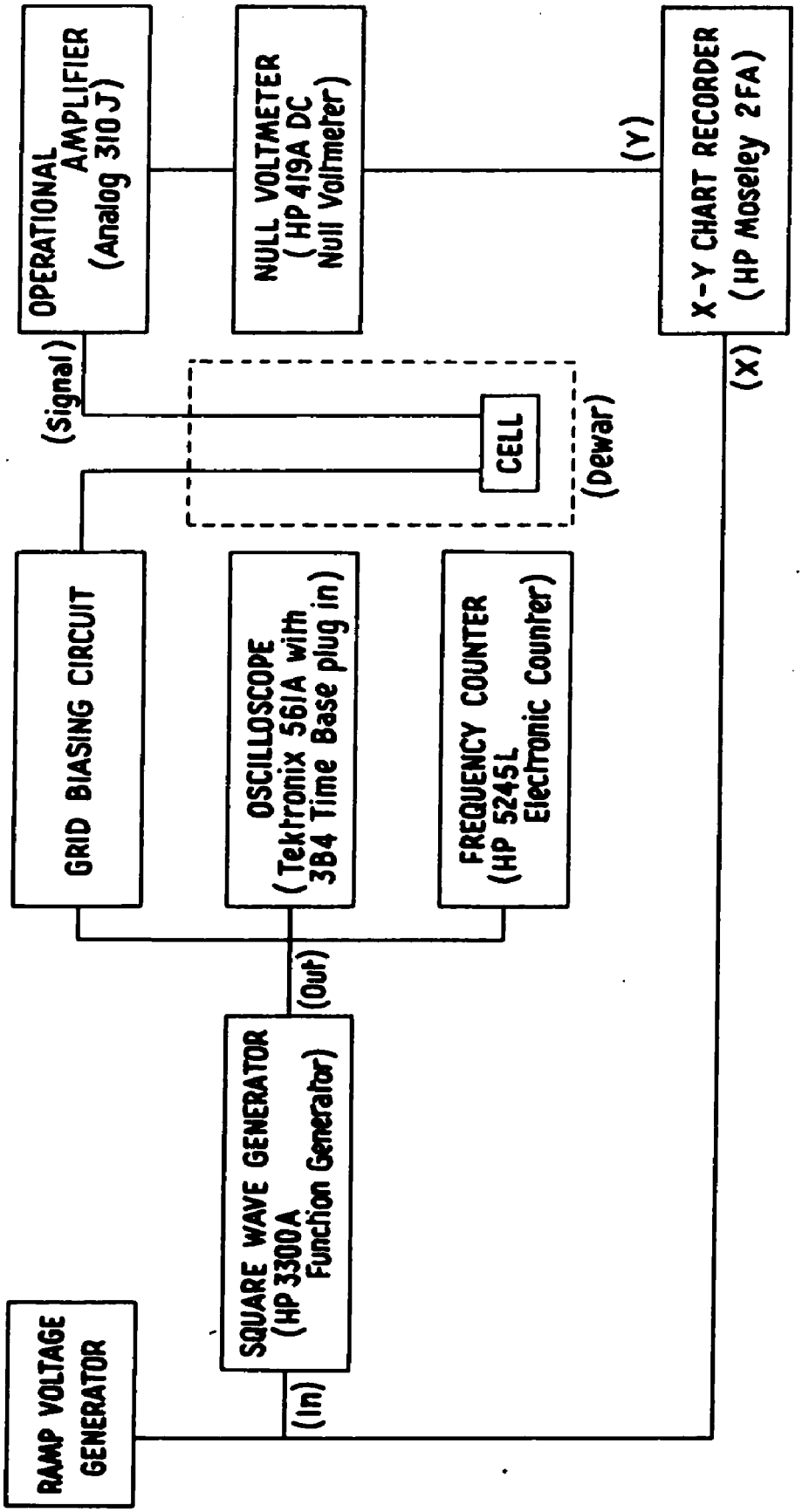

Fig. 8: Block diagram of the experimental electronics.

especially if it were feared the density of the gas in the cell was low enough that the range of the beta particles from the radioactive source was greater than the distance to G_1.) The grid biasing circuit itself is just a series of independent voltage dividers, one for each grid. A capacitor was attached from G_4 (the grid nearest the collector, a grid serving as a shield actually) to ground to cut down on square-wave pick-up, which might have been picked up by the collector as well. The voltages were arranged so that the collector was at ground (no applied voltage), as that is the easiest mode for operation of operational amplifiers.

Notice that the I versus f traces were done in a continuous sweep, the ramp voltage generator driving the system. Each sweep took roughly a minute.

We expect I to decrease linearly with f up to f_c, and be zero after that. (I was checked to be zero by reversing one of the grid biases.) An idealized curve of I versus f is shown in Figure 9. Notice that there is some rounding near the bottom. Northby[28] has derived an approximate expression for this rounding effect:

$$\begin{aligned} I(f) &= \frac{I_0}{2}\left(1 - f/f_c\right), && f < f_{min} \equiv \frac{1}{2\tau_{min}} \\ &= \text{unspecified}, && f_{min} < f < f_{max} \\ &= 0, && f > f_{max} \equiv \frac{1}{2\tau_{max}} \end{aligned} \qquad (2\text{-}4)$$

and

$$f_{max} \leq f_{min}\left(\frac{L_{max}}{L_{min}}\right)^2 \qquad (2\text{-}5)$$

L_{max} and L_{min} represent the extremes of length across the drift region--they represent the fact that the grids are not infinitesimally small, but of finite extension, and so particles may go through at an angle--especially if the electric field lines do not run exactly parallel to the axis of the cell. In addition to this, the grids are not soldered

perfectly to the grid holders, and there is some buckling of the grids to be expected. Figure 10 shows one of my good experimental curves, with the rounding near f_c.

In practice, f_c was determined by drawing straight lines (shown dotted in Figure 10) through the two "halves" of the curve. This was done for the part of the curve that is supposed to be zero because in point of fact this zero (and the first "half" of the curve too, for that matter) may be slowly drifting, the system not having perfectly returned to equilibrium since the last curve had been drawn, and the operating conditions abruptly changed (for example, by letting out some gas). This is shown exaggerated in Figure 10.

Figure 11 shows an experimental curve with a peculiar bump in it, a not uncommon occurence, but not a typical one either. It is not a poor curve in the sense that if another curve were traced out immediately afterward, the second would be different. The curve is quite reproducible for a given set of experimental conditions. Northby[28] had curves that were not linear all the way to zero frequency, but none of them looked like this. What the explanation of this bump is we do not know, although it may be a recombination or space charge problem in the region between the source and the first grid. The bump occured at various temperatures, densities, and grid voltage settings, and not at other values of these parameters, but not in any easily recognizable pattern. If this bump began to appear in our recorder traces during a run, we would try to vary the grid voltage settings to get rid of it; if this were not possible, we just had to live with it. Notice that aside from not understanding fully what is happening, it is a little unclear what to take for f_c in such a trace.

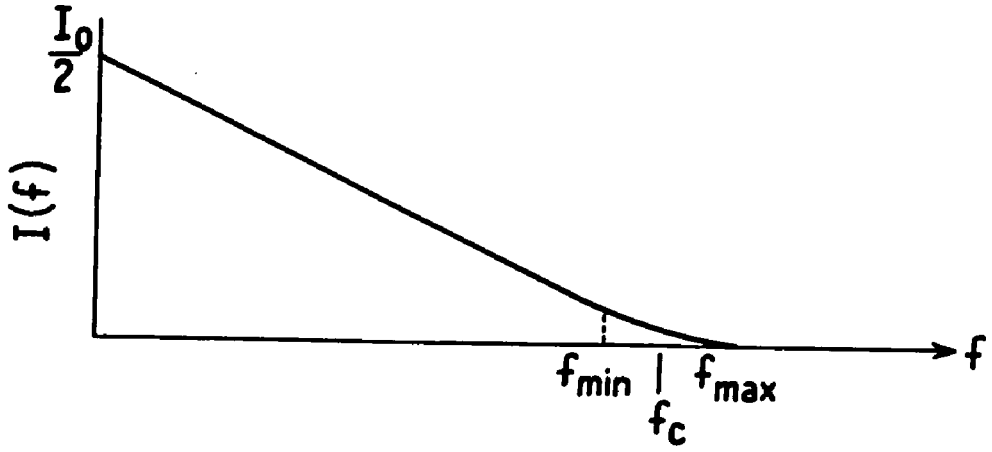

Fig. 9: I(f) versus f in the nearly ideal case.

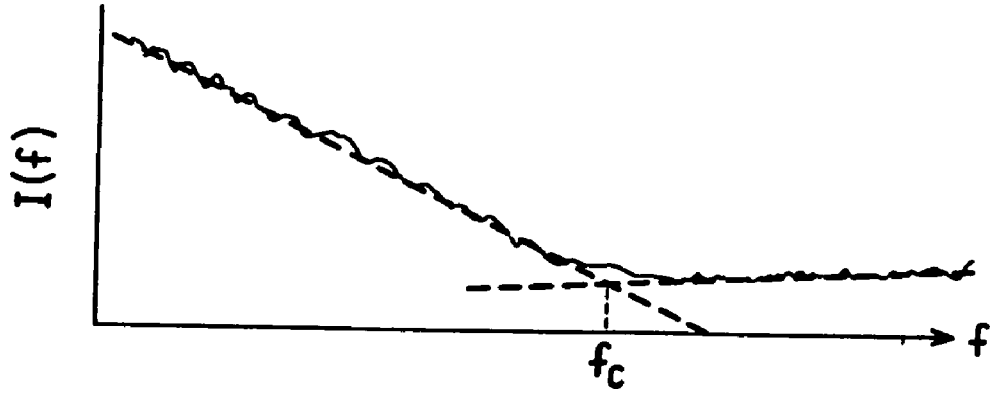

Fig. 10: I(f) versus f for a good experimental trace. Note that the zero of I(f) is shifted for clarity. Frequency range (linear scale) is about one decade (anywhere from 1-10 Hz to 1-10 KHz).

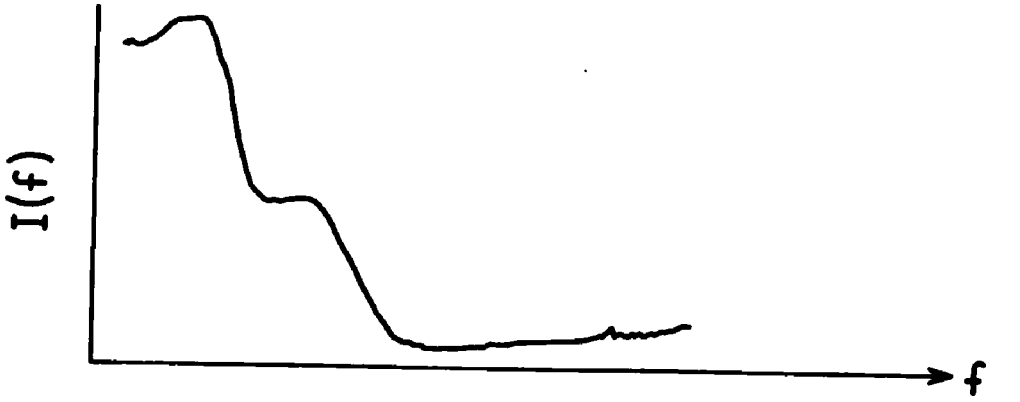

Fig. 11: I(f) versus f for a poor experimental curve. (Draftsman's copy of an actual curve.) Other conditions as for Fig. 10.

Only one measurement was made at each temperature and pressure, at more or less the lowest possible electric field. This is in contrast to the work of Levine and Sanders[1,2] who measured drift velocity versus electric field for several values of the applied field at each point, then took the limit for zero applied field. They were able to take only a comparatively few points for each isotherm, whereas I kept the electric field as low as possible and made measurements at many more points on each isotherm. The two methods yield essentially the same results at 4.18K (the only temperature where the two experiments overlap), although some effects which depended on the electric field were observed (see next chapter). We found that changing the field in the region S-G_1 had an effect on f_c if it was too disparate from that in the rest of the cell. This was presumably due to space charge effects or to heating up the electrons. The dominant mechanism would depend on the density. Finally, the questions raised in this paragraph are discussed a little further in subsection 3.1.2 on errors.

In addition to the limitation at high frequencies mentioned above (distortion of square waves starts at about 10 KHz, and gets bad by 100 KHz), there will obviously be a limitation at low frequencies. Surprisingly perhaps, measurements can be made down to about 2 or 3 Hz; below that level, the null voltmeter and chart recorder are no longer time-averaging the signal, but showing it directly as a function of time. Fortunately 2-3 Hz is low enough for all the measurements I wanted to make.

Finally, in addition to the above problems, there was a problem with signal strength. Signal strengths down to approximately

10^{-14} ampere could be detected, with the signal still larger than the noise. However, at high gas densities the signal strength sometimes would become too small to be seen. This effect seemed more pronounced for higher temperatures at the same density; however, no systematic study was made of it, but very likely it was a recombination effect in the S-G_1 region.

III. EXPERIMENTAL RESULTS

3.1 Electron Mobility in Helium-4

3.1.1 Electron Mobility Data in Helium-4

Smoothed values of measured electron mobility in helium-4 as a function of temperature and number density are presented in Figures 12-14. (The significance of the arrows will be explained in the next chapter.) Figures 13 and 14 are different plots of the same data; Figure 12 represents a different set of data. As the graphs imply, the data of Figure 12 were taken at constant temperature (see Table I for variation in temperature), whereas the data of Figures 13 and 14 were taken at nearly constant density. The dashed parts of the curves in Figure 13 are taken from the data of Figure 12--simply to show the bending over of the curves. (Figure 15 gives smoothed curves showing just how constant the density in fact was during the "constant density" sweeps.)

In Figure 12, the curves for 11.6, 13.8, and 18.1K do not extend to densities high enough that they "roll over" to some fairly constant low mobility value as is the case for the curves for 4.2 and 7.3K. The latter curves were done last, when my technique had improved somewhat over that used in gathering the data for the former curves; presumably now I could go back and extend the curves for 11.6, 13.8, and 18.1K with little trouble, but it was not thought to be worth the effort.

The data curves of Figure 12 are in good agreement with already published values for data at 4.2K[1] and 293K.[30] Measurements have been made at other temperatures (77K, for example) by other workers, but none of these to our knowledge extend to anywhere near as

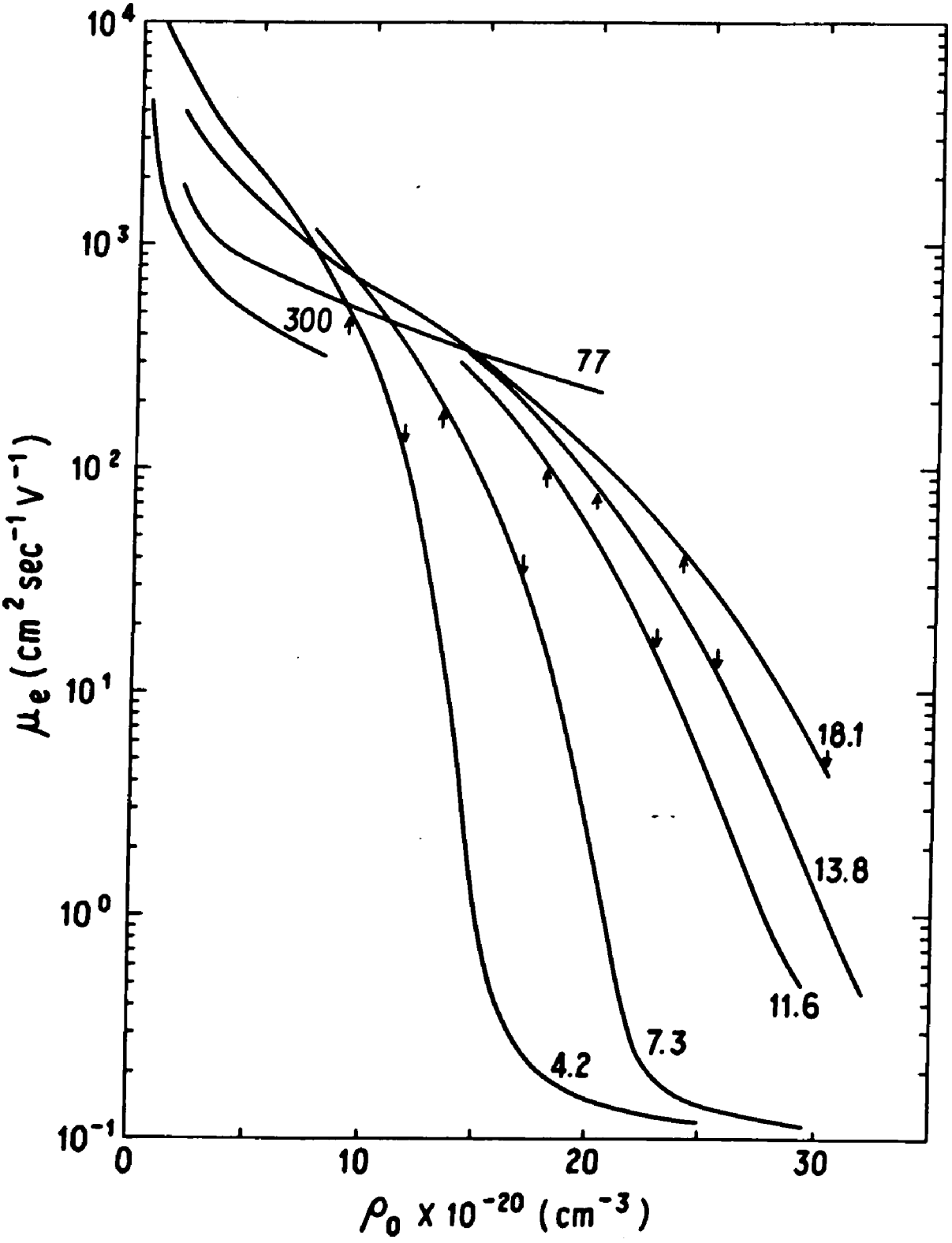

Fig. 12: Electron mobility versus number density at fixed temperatures (marked on curves in degrees kelvin) in helium-4.

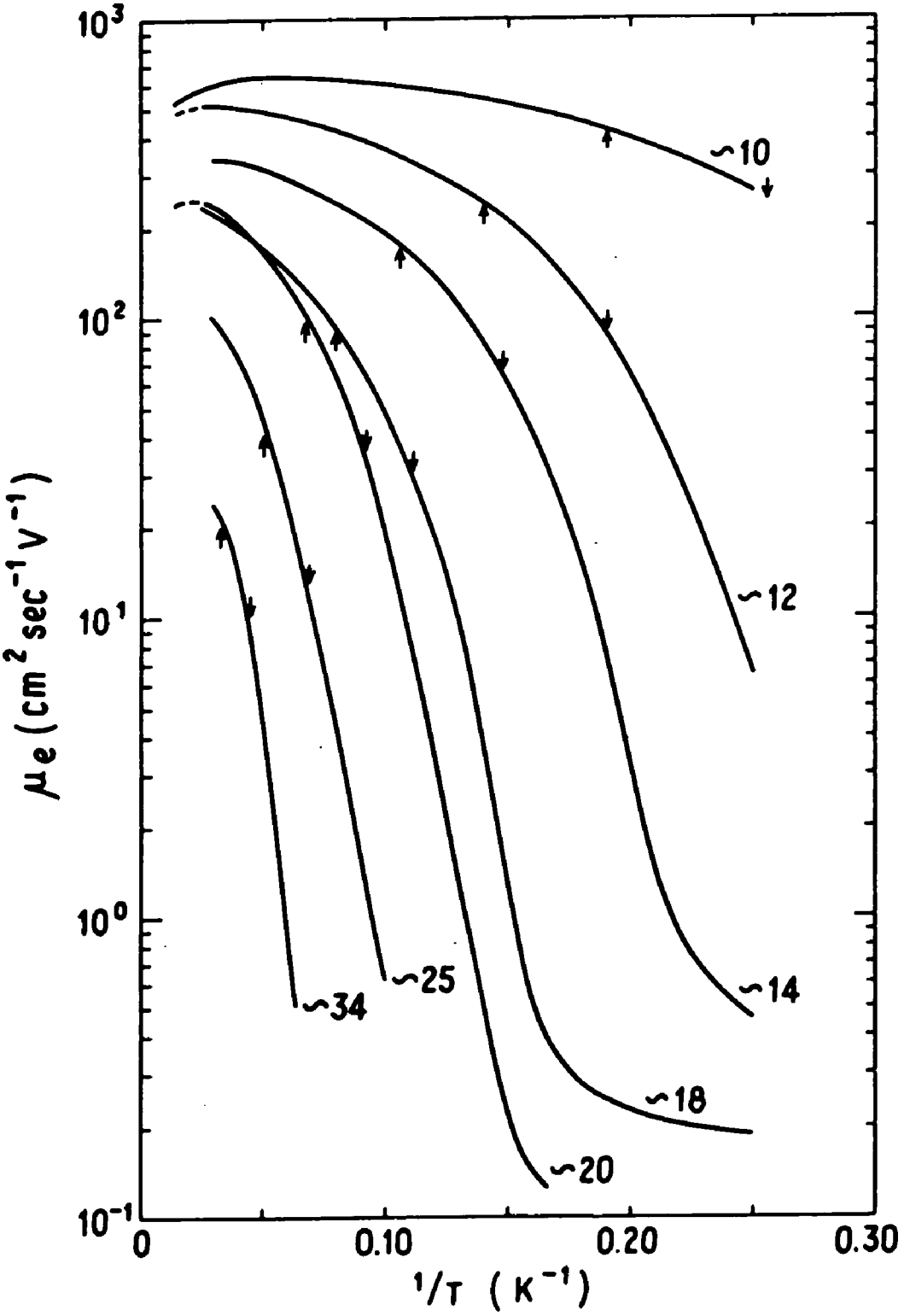

Fig. 13: Electron mobility versus inverse temperature at nearly constant density in helium-4. This density is marked on the curves in units of 10^{20} cm^{-3}.

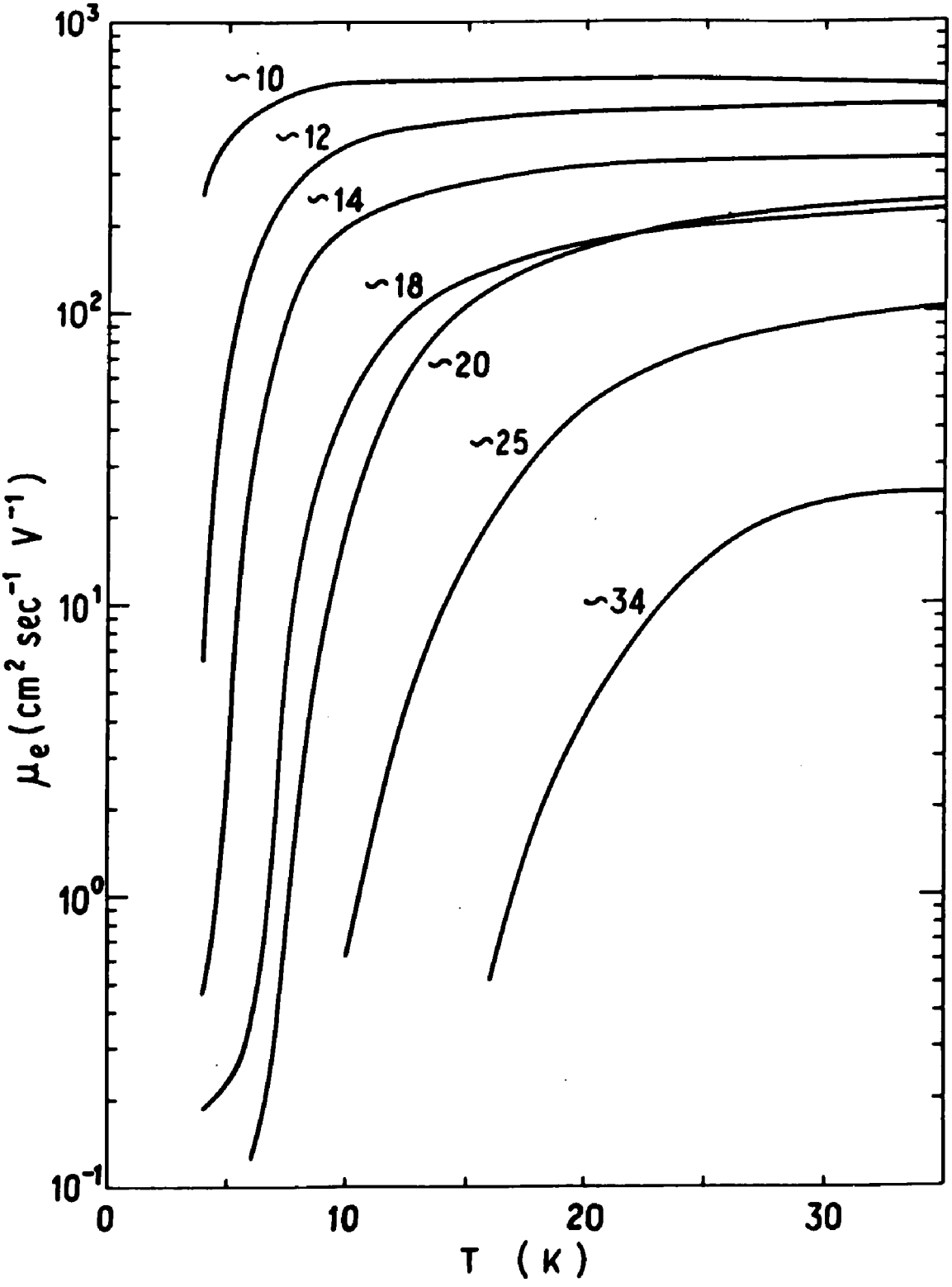

Fig. 14: Electron mobility versus temperature at nearly constant density in helium-4. This density is marked on the curves in units of 10^{20} cm^{-3}.

TABLE I

VARIATION OF TEMPERATURE DURING CONSTANT TEMPERATURE SWEEPS

	T(K)
Helium-4:	4.18 (variation not monitored)
	$7.28 \pm .012$
	$11.6 \pm .04$
	$13.8 \pm .02$
	$16.1 \pm .03$
	77.2 (variation not monitored)
	300 (room temperature)
Hydrogen:	$26.0 \pm .17$
	$28.0 \pm .17$
	$30.0 \pm .22$
	$31.7 \pm .063$
	293 (data of Grünberg[30])

Note that the variation in each temperature is quoted to a higher precision than the temperature itself. This is because the variation in each case is derived from the slope of the R versus T characteristic of the thermometer given in Figure 33 and is thus arrived at essentially independently from the value of the temperature itself.

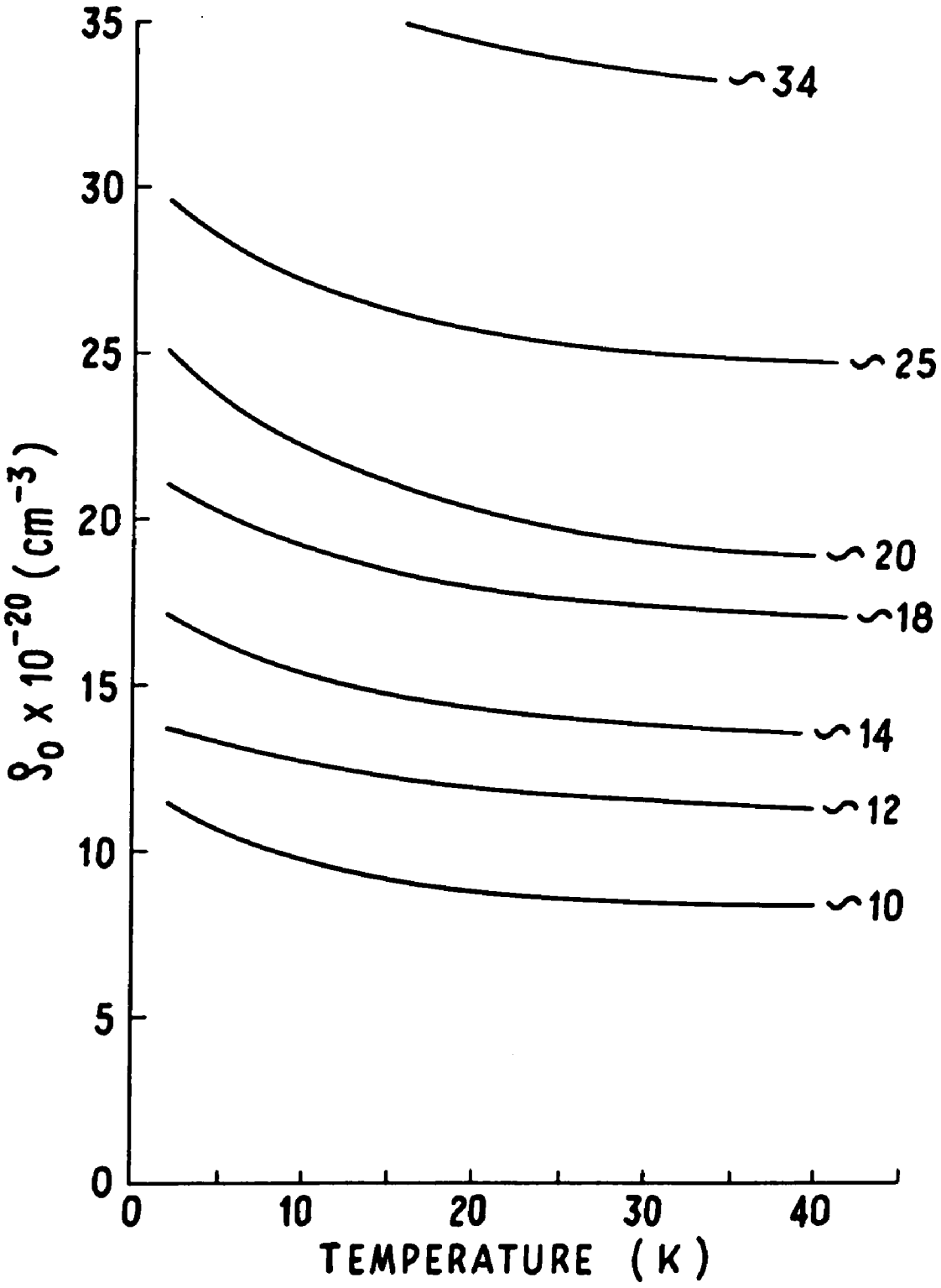

Fig. 15: Variation of number density versus temperature for nearly constant sweeps. Approximate densities used on other figures marked on curves.

high densities as our work, or the work at 4.2 and 293K just cited. Note also that we are using a different measuring technique (single-gate switching) from that used by Levine and Sanders[1] and Grunberg[30] (time-of-flight) to obtain their data at 4.2 and 293K, respectively. Measurements were made at lower temperatures,[1] but the limitation imposed by the saturated vapor pressure severely limits the maximum density that can be achieved. The curve for 4.2K, for example, extends to the density corresponding to the saturated vapor pressure for that temperature.

Figure 16 shows the loci of constant mobility in the ρ-T plane, a smoothed replot of the basic data presented in Figures 12-14--necessarily smoothed because the data at constant temperature and at constant density do no necessarily match up due to measurement errors, as discussed in the next subsection. Notice for the curves of larger constant mobility that each curve exhibits a maximum number density, and this point occurs at lower temperatures the higher the mobility. (Presumably the curves for lower mobility would show a similar shape if they could be extended to higher temperatures.) Notice that this says that a given mobility will not be observed above a certain number density, no matter what the temperature. As we move to higher number density, the range of possible mobilities becomes more restricted.

Figures 17-19 are the mobility data shown in Figures 12-14 divided by the semi-classical prediction for mobility given by Levine:[2]

$$\mu = \frac{4e}{3\rho\sigma(2\pi m k T)^{1/2}}\left[1 + 2B_1(T)\rho\right] \qquad (3\text{-}1)$$

where e=electronic charge
m=electronic mass
ρ=gas number density
σ=total interaction cross-section
B_1=second virial coefficient

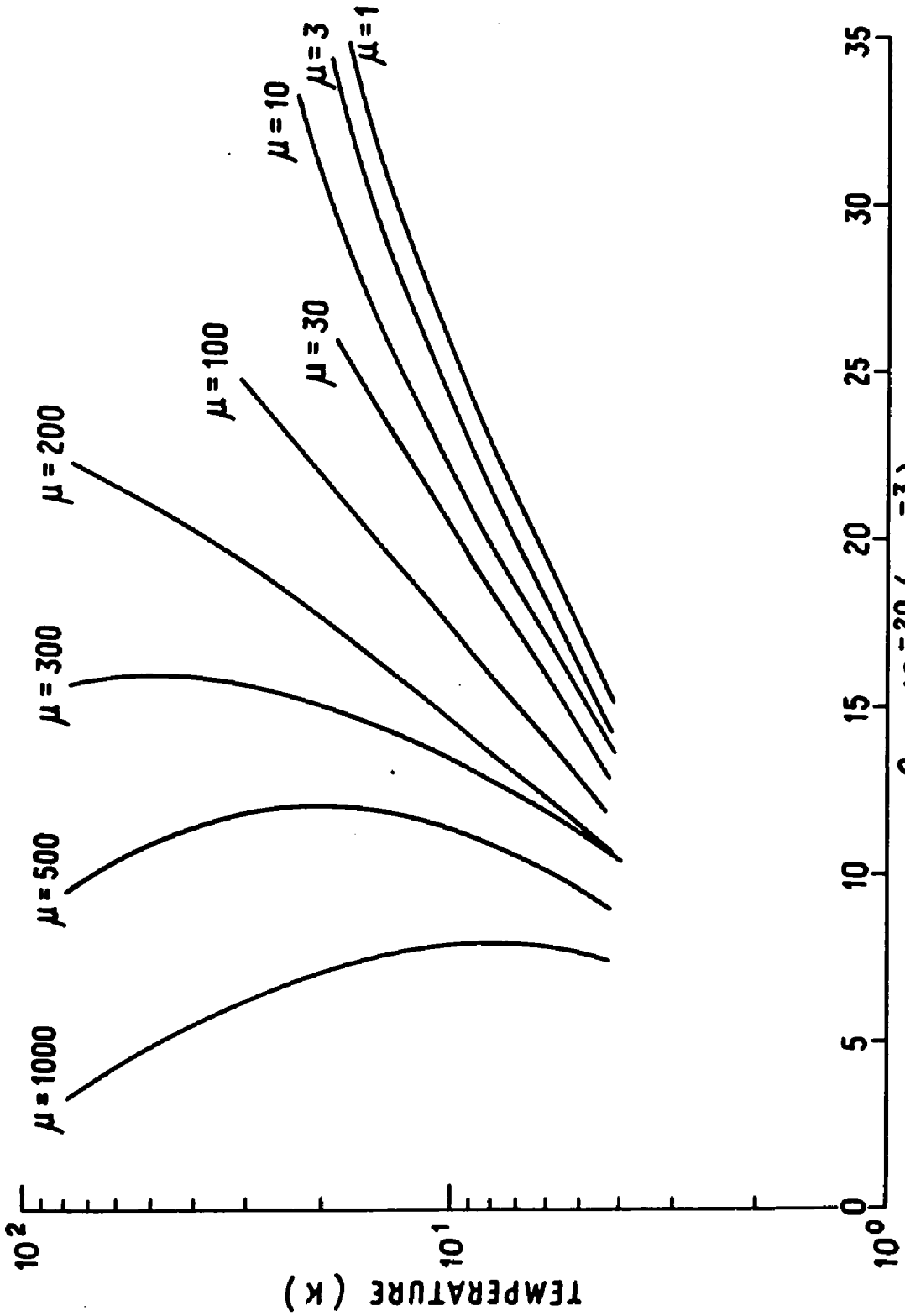

Fig. 16: Curves of constant mobility (in units of $cm^2/V^{-1}sec^{-1}$) in helium-4.

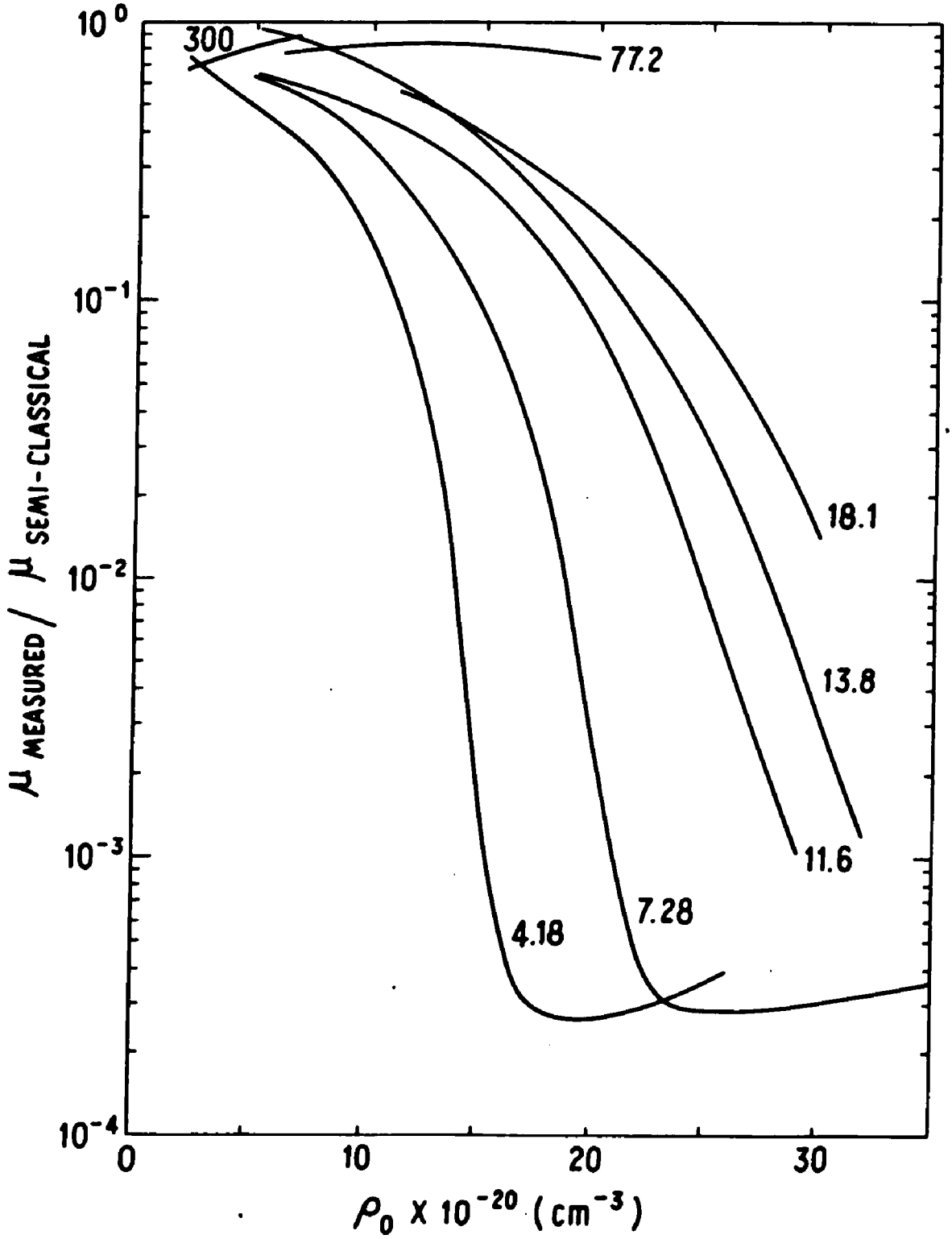

Fig. 17: Electron mobility divided by the semi-classical prediction versus number density at fixed temperatures (marked on curves in degrees kelvin) in helium-4.

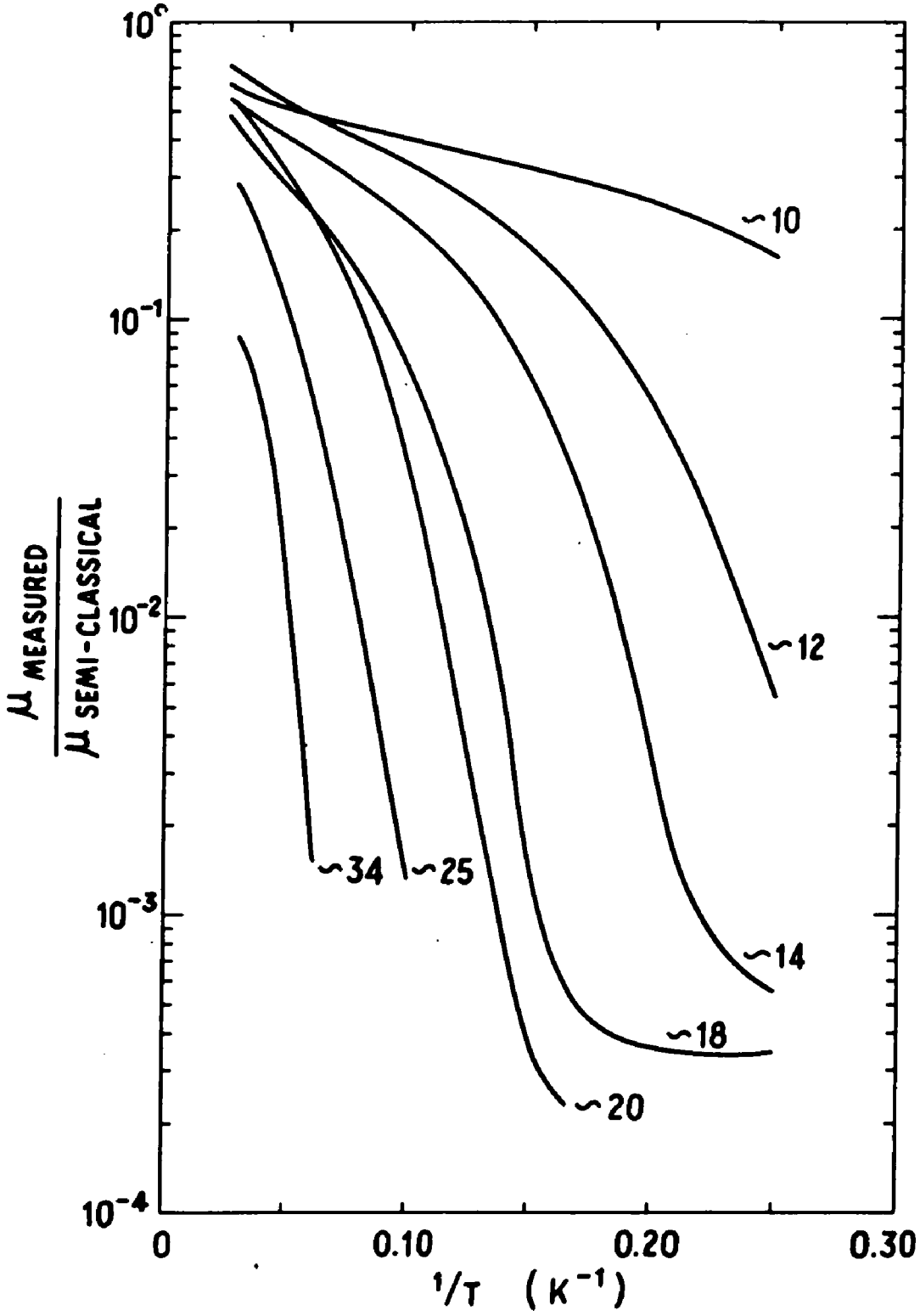

Fig. 18: Electron mobility divided by the semi-classical prediction versus inverse temperature at nearly constant number density (marked on curves in units of 10^{20} cm^{-3}) in helium-4.

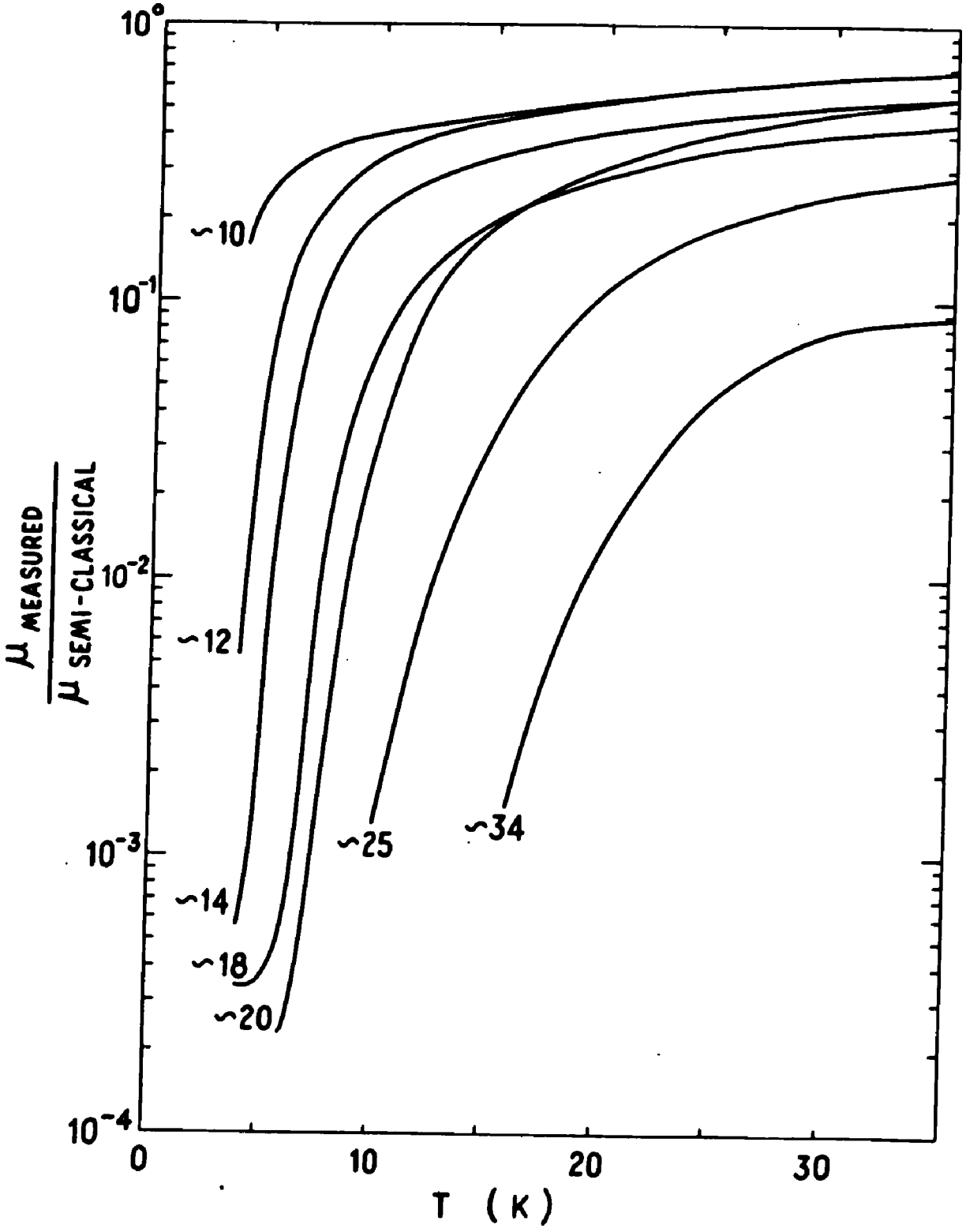

Fig. 19: Electron mobility divided by the semi-classical prediction versus temperature at nearly constant number density (marked on curves in units of 10^{20} cm^{-3}) in helium-4.

Levine calculated the correction factor $[1+2\beta B_1(T)]$ to the classical kinetic theory prediction. This correction factor is really the first order term resulting from a perturbation theory. It is easy to see that this is only an approximation, because below 20K the second virial coefficient for helium-4 is negative,[23] and so this formula predicts that as the number density is increased at a fixed temperature (always possible above the critical point), the mobility will eventually become negative, which is nonsense. Note that a much more general derivation has been published by Lekner and Cohen.[31,32] The result is, for $\mathcal{E} \to 0$. (This is equivalent to equation (7) of Levine and Sanders.[1])

$$\mathcal{M} = \frac{2}{3} \frac{1}{(\pi m kT)^{1/2}} \frac{e}{\rho 4\pi a^2 S(0)} \qquad (3\text{-}2)$$

where a=electron-atom scattering length
($\sigma = 4\pi a^2$)
S(0)=long-wavelength limit of the structure factor
$=nkT\kappa_T$
κ_T=isothermal compressibility

Using the equation of state (2-1), (3-2) reduces to (3-1) exactly. The variations in density shown in Figure 15 were taken into account in calculating this semi-classical mobility for the data taken at nearly constant density. For σ, we took O'Malley's recommended value of 4.9×10^{-16} cm^2.[33]

3.1.2 Errors

Figure 20 shows the actual data points for the 4.18K isotherm. There are in fact more data points for this isotherm than for most of the others, but this set of data was chosen because it illustrates some other things besides just the degree of scatter. The first thing to note is the effect of different electric fields, especially at low density. Remember that the beta particles from the radioactive source

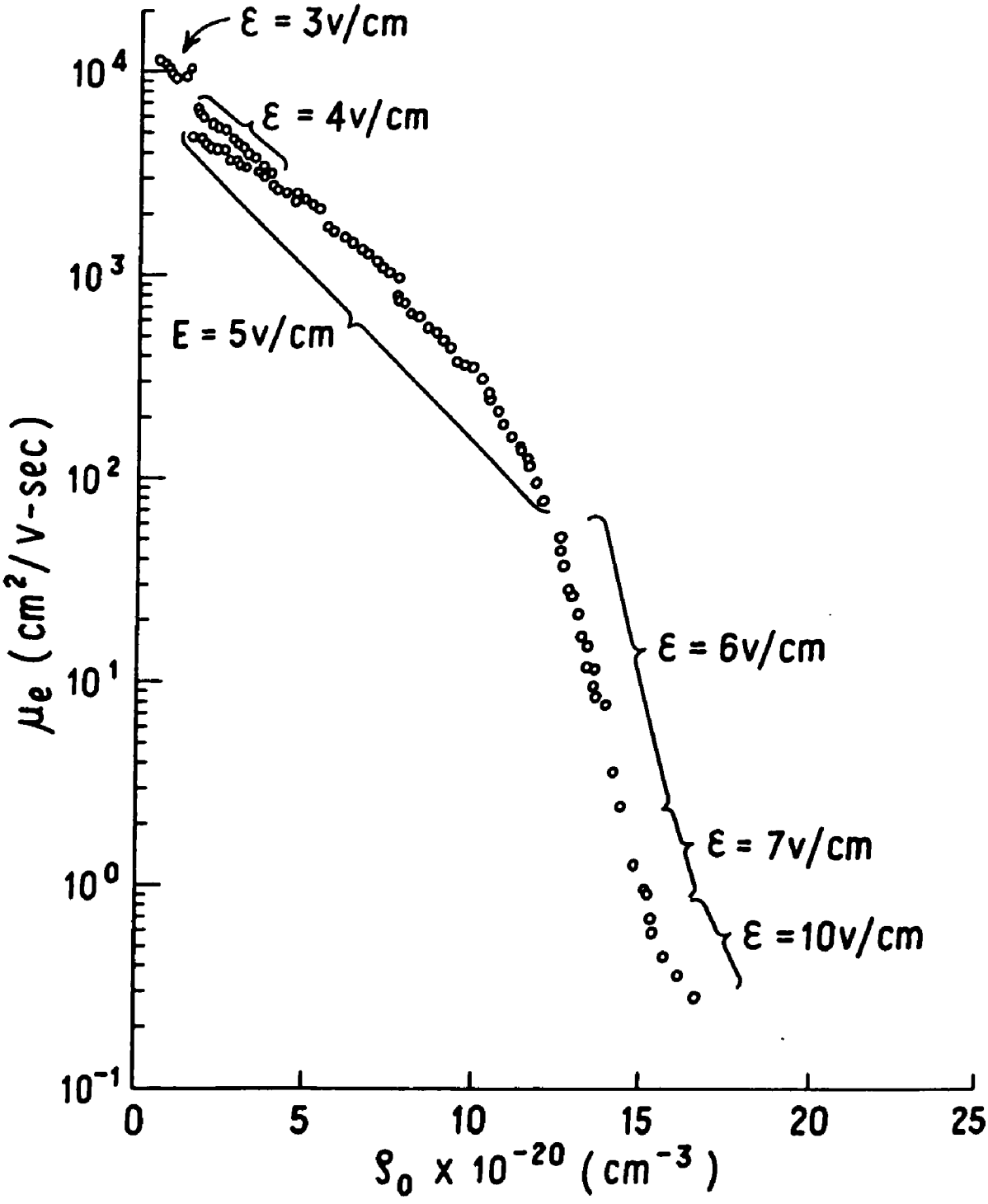

Fig. 20: Electron mobility versus number density in helium-4 at 4.18K, showing scatter of data points and effect of using different electric fields.

are stopped before the first grid for all densities above $.450 \times 10^{20}$ cm^{-3}, according the calculations presented in the last chapter. This density value is where the data begin in Figure 20. Notice that at about 1.5×10^{20} cm^{-3}, the data for $\mathcal{E}$=4 V/cm and $\mathcal{E}$=5 V/cm are obviously different, but that the data points move together as the density increases, becoming indistinguishable at about $4\text{-}5 \times 10^{20}$ cm^{-3}. The smoothed curve of this data was drawn ("eyeball" fashion) so as to "skim across the top" of the data points. Even so, it is clear that the low density ends of my data curves are the least reliable. This $\mathcal{E}$ field effect was noticed in other sets of data also. At higher densities, the changing of the electric field does not seem to produce this effect. Levine and Sanders[1,2] display some curves of drift velocity versus electric field, the curves showing different sorts of curvature. They also have a universal curve plot of $\sqrt{T/T_o}\, v_d$ versus $\xi = \frac{e\mathcal{E}\lambda}{kT}$, and our data agree with that at least roughly. Interestingly, electron mobility data published on eight liquid saturated hydrocarbons and liquid tetramethylsilane do not show any non-linearity between drift velocity and applied electric field up to the highest fields studied (140 KV/cm, at 23°C).[34] The criterion for when to expect non-linearities is[35]

$$\sqrt{\frac{M}{m}}\, e\mathcal{E}\lambda \geq kT \quad \text{or} \quad \mathcal{E} \geq \frac{kT}{e\lambda}\sqrt{\frac{m}{M}} = \frac{kT\rho\sigma}{e}\sqrt{\frac{m}{M}} \quad \text{or} \quad \lambda \geq \frac{kT}{c\mathcal{E}}\sqrt{\frac{m}{M}} \qquad (3\text{-}3)$$

This is because the electric field can "heat up" the electrons, drastically changing their distribution function. For the hydrocarbon data, the above equation says non-linearities would set in if $\lambda \geq .05$ Å, which presumably is not the case. For my data in helium-4 at 4.18K, $\mathcal{E}$=3 V/Cm and $\rho = 10^{20}$ cm^{-3}, equation (3-3) says there will be non-linearities if $\lambda \geq 10^2$ Å. In point of fact, $\lambda = 1/\rho\sigma \sim 2 \times 10^{3}$ Å, so it is not

at all surprising to see the beginning of a non-linear region setting in.

Secondly, notice that the data at $\mathcal{E}$=5 V/cm seem to fall into well defined groups, an effect also observed in other data. Why this should be is not known. Finally, as would be expected the density of data points along the curve is least where the curve is rising the fastest--simply because a small change in the gas density there produces a correspondingly larger change in mobility than elsewhere.

In addition to the above items, there are the sources of error mentioned in the last chapter (in detail there): (i) how well we know the temperature, (ii) how well we can calculate the number density, given the uncertainties in our knowledge of temperature and pressure, (iii) how accurately we know the actual length that the electrons traverse in the drift region, (iv) how accurately we can determine the amplitude of the square waves running the gate (and the distortion of the square waves at high frequency), and finally (v) how accurately we can determine the cut-off frequency f_c from the signal strength versus frequency curves (especially for curves of odd shape). Space charge effects may also be important, but we always tried to work at a low signal strength level to avoid this problem.

Finally, in attempting to arrive at an error estimate by comparison with measurements made by other workers, which means by making comparisons in the low density limit where kinetic theory should apply, there seems to be an uncertainty as to what value to take for the cross-section. To quote Levine and Sanders, "For electrons in the energy range of importance in this work ($\mathcal{E} \sim 10^{-3}$ eV) only s-wave elastic scattering is of any importance, and the interaction can be adequately

characterized by a single parameter, the zero-energy s-wave scattering length a. We adopt for this parameter the value recommended by O'Malley,[33] $a=1.18a_o=0.62\mathring{A}$, so that $\sigma=4\pi a^2=4.9\times10^{-16}$ cm^2."[1] However, Grünberg[30] made measurements of electron drift velocity as a function of $\mathcal{E}/P$ up to about 42 atmospheres at room temperature (293K) (that is, to a density of 10.3×10^{20} cm^{-3}), with a claimed accuracy of 1-1.5%. From his data, and assuming the kinetic theory formula is correct, it is easy to deduce a cross-section of roughly 6.9×10^{-16} cm^2, yielding $a=1.40a_o=.740\mathring{A}$, a considerably different value from the above. Goldan, Goldstein, and Cahn,[36,37] on the basis of microwave measurements in low temperature helium plasmas, find a cross-section between $10\text{-}19\times10^{-16}$ cm^2, for densities below 2.3×10^{18} cm^{-3}, a value very different from either of the above. They postulate that, "For electron temperatures in the vicinity of 10K, the number of neutral atoms in a sphere whose diameter is equal to the electron deBroglie wavelength, λ_e, may be as high as 50 for neutral gas pressures as low as 1 Torr at 4.2K. Under such conditions, the concept of electron <u>binary</u> collisions [the basis of classical concepts and derivations] might be expected to have little validity."[36] Any very precise fitting of the data to theory would require clarification of this point. However, as will be seen in the next chapter, no theory as yet comes very close to agreement with experimental results over the whole range of data.

Considering all this, it would seem that a reasonable guess as to the error limits would $\pm$20% absolute accuracy and perhaps $\pm$5% relative accuracy (about what Levine and Sanders[1] quote).

3.2 Mobility in Normal Hydrogen

3.2.1 Limitations Imposed by Coexistence Curves

Figure 21 shows the coexistence curves of helium-4 and normal hydrogen, as well as the ranges over which data were taken in the two gases. By a coexistence curve, I mean both halves of a saturated vapor pressure curve--that is, displaying both the liquid and gas densities at saturation at each temperature. The region between these two densities is inaccessible. The curve for helium-4 was calculated from the equation

$$P = kT(\rho + B_1\rho^2) \qquad (3\text{-}4)$$

and values of P and T at saturation were obtained from Donnelly[38] (based on the 1958 temperature scale) for the gas phase; data on the liquid phase were obtained from Wilks.[39] The data for the curve for hydrogen were obtained from an empirical equation fitted to measured data from Woolley, Scott, and Brickwedde.[25] Figure 21 shows very clearly that the region where most of the data were taken in helium-4, and presumably where similarly interesting phenomena would appear in hydrogen, is simply forbidden. We were forced to skirt around the edge of the coexistence curve of hydrogen in the search for electron mobilities which depart markedly from values predicted by kinetic theory.

3.2.2 Normal versus Equilibrium Hydrogen

Unlike monatomic molecules like helium, diatomic molecules of like atoms such as hydrogen have rotational energy levels, which are divided into two groups (because of the different nuclear spin alignments) which are known as the ortho and para series. At high temperatures (such as room temperature), 75% of the molecules are in the ortho state and 25% are in the para state (this is called normal

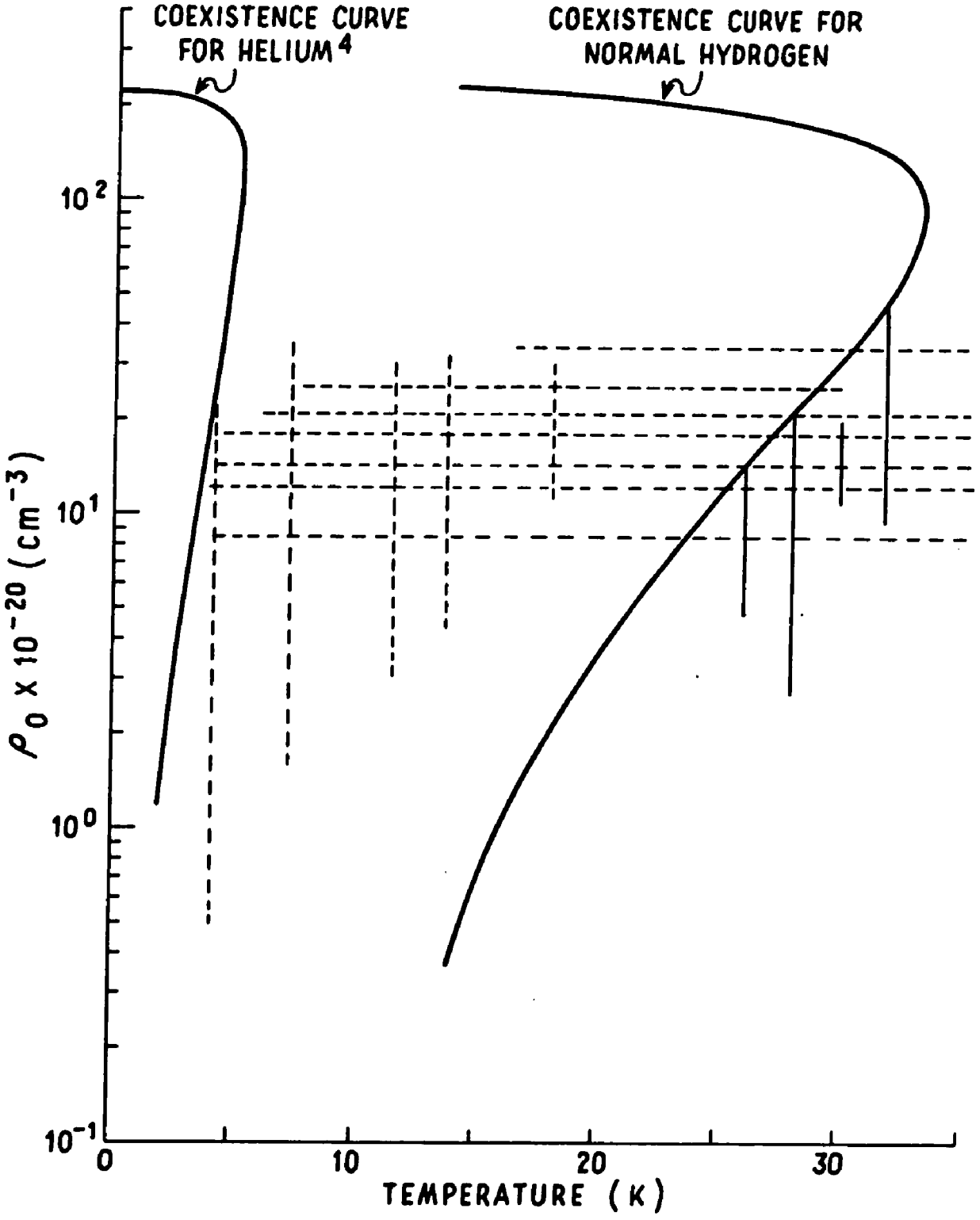

Fig. 21: Coexistence curves for helium-4 and normal hydrogen together with ranges over which data were taken (dotted lines for helium-4; solid vertical lines for hydrogen).

hydrogen), whereas at low temperatures (such as where I was working) almost 100% of the molecules are in the para state--if equilibrium has been achieved. In fact, however, unless a catalyst is present, transitions from one form to the other proceed at a very slow rate, so that normal hydrogen may be cooled down to very low temperatures, and even after several hours it will still be very close to normal hydrogen.

However, even if I had equilibrium rather than normal hydrogen in my experimental cell, I do not think it would have made any perceptible difference. This is because most of the physical properties of the two forms are almost identical (for example, the equation of state, or equivalently, the second virial coefficient is imperceptibly different[25]), as most physical properties are due to the electronic energy levels. There are some physical properties that will be different for the different forms (those for which the rotational energy levels--which are much smaller than the electronic energy levels--are important), such as the specific heat at low temperatures.

3.2.3 Electron Mobility Data in Normal Hydrogen

Figure 22 shows smoothed values of the data taken in normal hydrogen. (For variation in the temperatures quoted, refer back to Table I.) Note that the general features are even qualitatively very different from the data in helium-4--in particular, the data for the 30.0 and 31.7K isotherms show two branches. (Experimentally this means that the signal versus frequency traces show two definite downward slopes--at frequencies different from each other by a factor of 10^3--followed by a prolonged flat "zero level".) The data were taken by starting at the saturated vapor pressure and moving toward lower

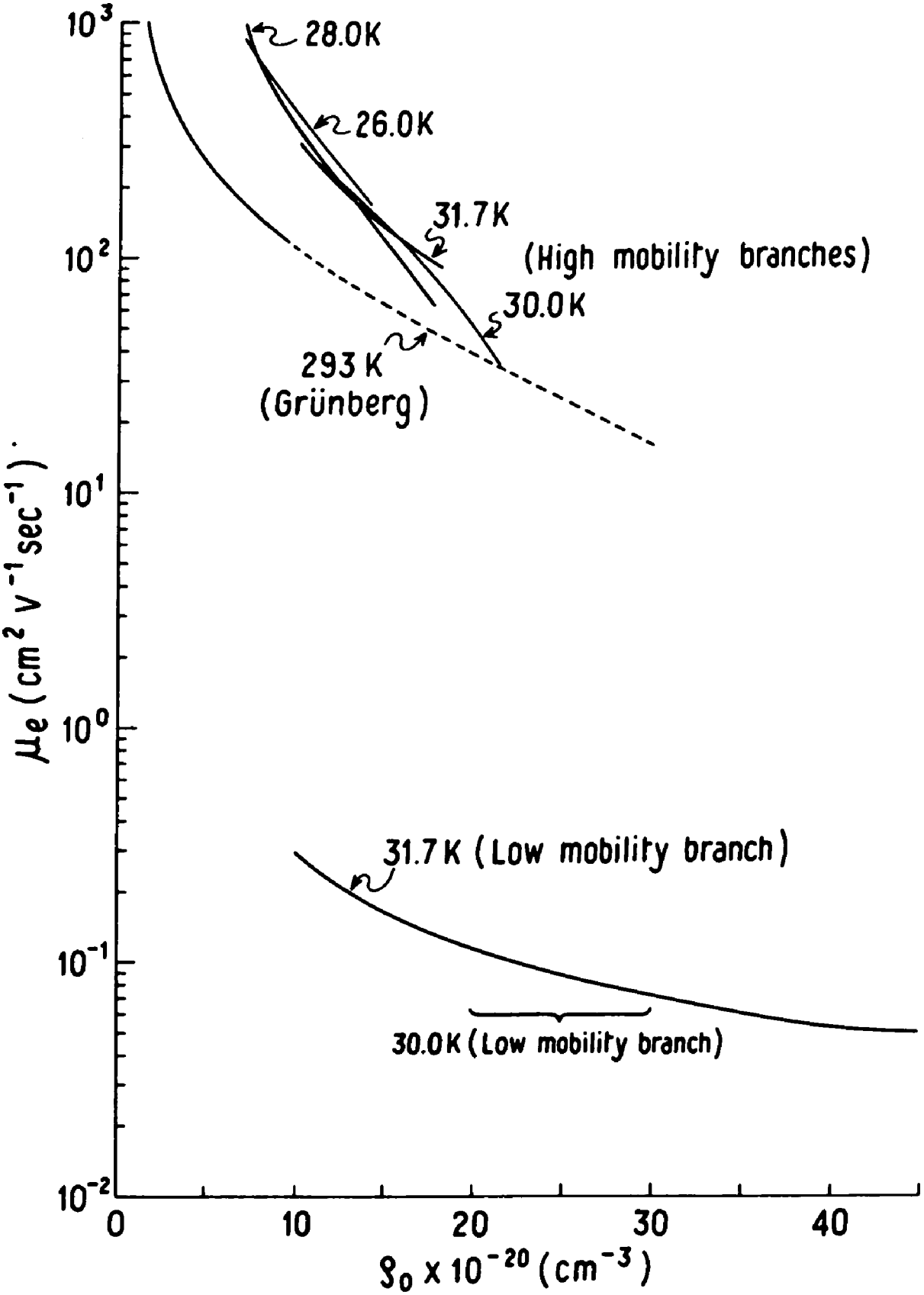

Fig. 22: Mobility of negative particles versus number density at fixed temperatures (marked on curves in degrees kelvin) in normal hydrogen.

densities. For the high mobility part of each isotherm, measurements were extended to as high a density as possible; for the 26.0 and 28.0K isotherms, the high mobility branches stopped at the densities corresponding to their saturated vapor pressures, but for the 30.0 and 31.7K isotherms the signal strength simply became too small to be seen before the saturated vapor pressure was reached. The signals for the low mobility branches of these latter isotherms (which are so close together that one virtually coincides with the other, as shown in Figure 22) could be seen all the way out to the densities at their respective saturated vapor pressures. Figure 23 shows the relative strengths of the signals of the high and low mobility branches for the 31.7K isotherm. (The strength at any point is the value of I_o, obtained by extrapolating the x-y recorder trace back to zero frequency.) (The low mobility branch of the 30.0K isotherm was not followed back to lower densities because its significance was not realized at the time.)

Also shown in Figure 22 are the data of Grünberg[30] at 295K. In contrast to his data on helium-4, his hydrogen data (v_d versus E/P, which extend up to a number density of 9.92×10^{20} cm^{-3}) can be fitted assuming a cross-section which increases approximately linearly with number density. (Appendix VII presents an alternative explanation for his data.) The dashed part of the curve is an extrapolation based on that assumption, but there is no really firm evidence for believing this is the correct picture. This changing cross-section can not be accounted for by the virial coefficient dependence represented by equation (3-1), from which we can write (comparing with the classical theory equation)

$$\sigma_{effective} = \frac{\sigma_{low\ density}}{1 + 2 B_1 \rho} \qquad (3\text{-}5)$$

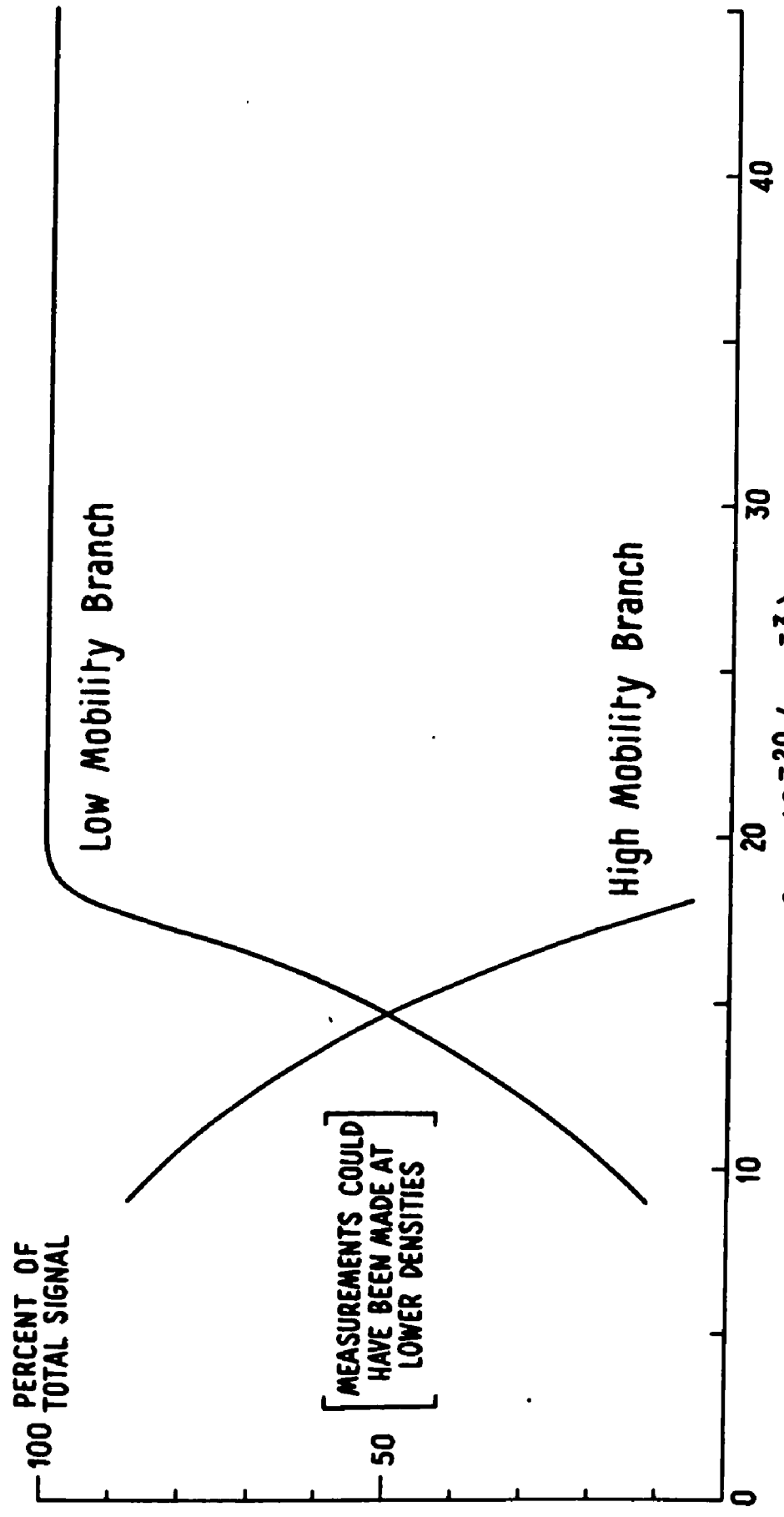

Fig. 23: Relative signal strengths of received signals of negative particles for electrons injected into normal hydrogen at 31.7K. The maximum density corresponds to the saturated vapor pressure.

Extracting the actual cross-sections from Grünberg's data indicates σ increases from 10.4×10^{-16} cm^2 at $\rho=.250\times10^{20}$ cm^{-3} to 13.6×10^{-16} cm^2 at $\rho=9.92\times10^{20}$ cm^{-3}, a 30% change. However, equation (3-5) predicts (using B_1 from reference 25) that σ_{calc} will decrease about 10% from $\sigma_{low\ density}$ at a number density of 10×10^{20} cm^{-3}. Because of this uncertainty in the cross-section even at 293K, no semi-classical calculations have been done for hydrogen as were done for helium-4. Legler,[40] using Grünberg's data, states that the scattering length is .85Å, or the cross-section is 9.10×10^{-16} cm^2. It is shown in Appendix VII that Legler's theory gives a good fit to Grünberg's hydrogen data, but unfortunately does not fit the other data discussed there so well. As a point of interest, I checked that the semi-classical correction factor $(1+2B_1)$ had dropped to .90 at $\rho=8.43\times10^{20}$ cm^{-3} for the 31.7K isotherm in hydrogen. (The virial coefficient came from reference 26.) For comparison, for helium-4 at 3.96K, the same point was reached at $\rho=3.64\times10^{20}$ cm^{-3}.

Notice that the high mobility branch of the 30.0K isotherm is starting to bend downward as though it were about to cross the 293K isotherm and drop precipitously. However, there are too few data points, which are scattered sufficiently so that it can not be said for certain whether this is happening or not. A direct comparison with helium-4 is made in Appendix VII. Errors are about the same as for the data of helium-4, discussed in the last section.

It was suspected after taking the data at 30.0K that perhaps the low mobility branch was due to some impurity. So for the run at 31.7K the highest purity tank gas hydrogen was used (mass spectroscopy and gas chromatography tests by Airco showing no impurities on the parts

per million scale). Impurities could not have slowly entered the system during the course of the measurements because I started at the maximum density and just let gas out between measurements. Outgassing of the system can be ruled out because in the course of the run the signal strength of the low mobility object eventually declined, both in absolute magnitude and in percentage of the total signal strength. Impurities could not have entered the system right at the beginning through the piping system when the pressure was less than the outside pressure, because I had to retransfer some more liquid helium in the middle of the run (which dropped the pressure in the can and the piping system to essentially vacuum) and there was no change or break in the data before and after this event. Thus, it seems we can rule out impurities as the cause of this peculiar data in hydrogen. (Peculiar compared to the data in helium-4 anyway.) What the low mobility object might be will be considered in the next chapter.

3.3 Summary of Experimental Results

Before summarizing the data presented in this chapter, I think it is useful to briefly summarize current data on electron and positronium (both objects much lighter than any positive ions) behavior in other systems, to put this particular data in perspective.

Electron[3] and positronium[41,42] behavior in liquid helium may be explained in terms of the bubble model. Positronium bubbles form in solid helium;[43] they have also recently been observed in liquid argon, krypton, and xenon, but not in the solid phases of these rare gases.[44] Electrons, however, do not form bubbles in argon, krypton, or xenon in the liquid and solid phases[45,46] but have mobilities indicating they are free, or nearly so, which is expected, as electrons

have a negative scattering length (attraction) in all these species, but a positive scattering length (repulsion) in helium. (If electronic bubbles do not form in the liquid, it is not expected that they will in the gas phase either.)

In addition to the rare gases, electron mobilities have been studied in several other liquids as well. For one class at least, good qualitative understanding has been achieved: "Most of the earlier studies were concerned with the binding of excess electrons in polar solvents (i.e., metal-ammonia solutions,[47] solvated electrons in water[48]) and in metal-molten salt systems.[49] In the case of polar solvents there is compelling evidence for the formation of localized states of the excess electrons at low electron densities, while at high concentrations a transition to a metallic state is observed.[47] The electronic properties of dilute metal solutions are primarily those of a collection of localized electrons, each moving in a cavity in the liquid. In sum, our qualitative understanding of the negatively charged species in a polar liquid in which no chemically bound state exists for the excess electron is quite satisfactory."[5] Recent measurements of electron mobility in dielectric liquids (eight saturated hydrocarbons and tetramethylsilane) yield mobility values ranging from 0.09 $cm^2V^{-1}sec^{-1}$ in n-hexane to 90 in tetramethylsilane (at 23°C)--a span of three orders of magnitude in what are otherwise hydrocarbons of very similar physical properties. ("Probably the major difference between hydrocarbons and monatomic liquids, with respect to electronic behavior, is the permanent dipole moment of the C-H bond. In saturated hydrocarbons these moments cancel geometrically, so the molecules as a whole have no moment, yet in the immediate neighborhood of each C-H

bond a dipole field exists. Then: (a) each bond acts as a strong scattering center for free electrons; (b) in the random thermal motions of the molecules, configurations are continually forming and dissolving in which the local dipole fields reinforce each other to form potential wells.") The data do not seem to be explicable in simple terms by considering the electrons as "quasifree" or by considering the electrons to be localized in traps.[34] Finally, very recent measurements of electron mobilities in mixtures of n-hexane and neopentane can be fitted by the equation

$$\mu = \mu_n \exp(-X_h E/kT) \qquad (3\text{-}6)$$

where μ_n=mobility in pure neopentane
X_h=mole fraction of n-hexane
E=a constant (activation energy)

(Notice this functional form is just like that for mobility in an insulator with traps.) The authors think the explanation lies in a collective trap involving several fluid molecules.[50]

With the above in mind, let us now return to the mobility data presented in this chapter. Notice that these data (helium-4 in particular) are different from almost all of the above in that they show the systematics of a transition of electron mobility from one regime (free, or extended state) to another (bubble, or localized state, characterized by a nearly constant low mobility). It is possible to view the curves of μ versus 1/T (Figure 13), for instance, in terms of an expression like (3-6). We see then that the activation energy entering the exponential is density (or pressure) dependent. When I come to discuss the theoretical aspects of this problem the origin of this fact will become apparent. Furthermore, it will be seen that the electron must play an essential role in the trapping process,

and this is probably true in the case of the hydrocarbons mentioned above also. Of course, these measurements in helium-4 gas represent an extension of the work of Levine and Sanders,[1,2] but an extension over a wide enough range of temperatures so that the systematics of the sudden drop of electron mobility in helium-4 gas are now much better known. (Figure 21 is a concise summary of the ρ,T range of my data in helium-4.) The maxima in the $\rho(T)$ curves (Figure 16) mark the departure from anything approaching classical behavior, which is more clearly highlighted by the reduced mobility curves of Figures 18 and 19.

Measurements in hydrogen gas at low temperatures and high densities have been made for the first time, resulting in a qualitatively different picture from that which applies to any other substance yet studied, namely that there exist two mobility branches, and these branches coexist in the span of densities covered. (There exists one previous measurement made indirectly by field emission of electrons into liquid hydrogen, yielding a mobility of 0.02 $cm^2V^{-1}sec^{-1}$.[51]) From the data presented, it is not clear whether the high mobility curves in hydrogen will drop precipitously upon going to higher densities, as is the case with helium-4; it is also not clear just what object is involved in the low mobility curves. I will make suggestions for what experiments might be attempted next in the last chapter.

IV. THEORETICAL CALCULATIONS OF ELECTRON MOBILITY

4.1 Localized State Models for Electron Mobility

4.1.1 General

As mentioned in the introduction, it is now generally accepted (due to Levine's[2] work) that cluster ions and impurity ions can be ruled out as possible explanations of the data (at least for the helium-4 gas data). That leaves two general types of theories to be considered: (i) localized state, or bubble, models, and (ii) various extended state, or scattering, models. By an extended state, I mean one in which the electron propagates through the fluid as a plane wave, scattering off the molecules of the fluid, but still describable by a wavefunction that extends over a very large number of atomic spacings. By a localized state, I mean one in which the electron's wavefunction is effectively restricted to a space of only a few atomic spacings, for some reason or other (such as being trapped in some sort of potential well of about that size). In this section I will discuss bubble models; in section 4.2 I will briefly review scattering models; and finally in section 4.3 I will try to combine both types of theories in a qualitative way in an attempt to fit a data curve for helium-4. Most of the remainder of the chapter will be devoted to a discussion of the data in normal hydrogen.

4.1.2 Spherical Square Well

I will now briefly review the theory of the spherical square well potential as presented by Springett, Jortner, and Cohen,[5] and then apply the calculation to the problem of predicting a mobility curve (at constant temperature, with the density varying, say) for an electron

in helium-4 gas. The theory presented in reference 5 will be simplified in that polarization corrections will be ignored, and an experimental rather than a theoretical value of the scattering length will be used. The experimental scattering length represents a combination of the Pauli principal scattering length and polarization effects due to the $1/r^4$ electron-atom interaction.

The Wigner-Seitz model, which was developed originally for crystalline solids rather than fluids, states that each atom in the fluid is replaced by an equivalent sphere of radius

$$r_s = \left(\frac{3}{4\pi\rho_o}\right)^{1/3} \tag{4-1}$$

We presume that in any undisturbed portion of the fluid that the potential V obeys the following conditions:

$$\begin{aligned} &\text{(i)} \quad V=V(r) \qquad \text{(spherical symmetry)} \\ &\text{(ii)} \quad V(|\underline{r}+2\underline{r}_a|)=V(|\underline{r}|) \qquad \text{(translational symmetry)} \end{aligned} \tag{4-2}$$

Now the one-electron ground state wavefunction ψ_o is symmetric about the center of any equivalent sphere (that is, about any nucleus) so

$$\left(\partial\psi_o/\partial r\right)\Big|_{r=r_s} = 0 \tag{4-3}$$

The wavefunction obeys the equation

$$\left[-\frac{\hbar^2}{2m}\nabla^2 + V(r)\right]\psi_o(r) = V_o\psi_o(r) \tag{4-4}$$

where V_o is the ground state energy of an excess electron <u>in the unperturbed fluid</u>. For V(r) we choose a square well pseudopotential to obtain a model potential V_M given by

$$\begin{aligned} V_M &= \infty, \quad r<r_s \\ &= 0, \quad r>r_s \end{aligned} \tag{4-5}$$

The s-wave ground state solution to this problem is

$$\psi_o = \frac{\sin k_o(r-a)}{r} \tag{4-6}$$

$$\text{where} \quad k_o = \left(\frac{2m}{\hbar^2}V_o\right)^{1/2} \tag{4-7}$$

and is determined by the above boundary conditions, leading to

$$\tan k_0(r_s - a) = k_0 r_s \qquad (4\text{-}8)$$

Thus, r_s is obtained first, then k_0 (if a value of the scattering length a is known), and then V_0.

Now for the real problem we take a spherical step in the density distribution

$$\begin{aligned} \rho &= 0, \quad r < R \ (\neq r_s) \\ \rho &= \rho_0, \quad r > R \end{aligned} \qquad (4\text{-}9)$$

The electron is then taken to be localized in this well. The eigenvalue equation to be satisfied is

$$\begin{aligned} \left(-\tfrac{\hbar^2}{2m}\nabla^2 - E_e\right) f(r) &= 0 \quad , \quad r < R \\ \left(-\tfrac{\hbar^2}{2m}\nabla^2 + V_0 - E_e\right) f(r) &= 0 \quad , \quad r > R \end{aligned} \qquad (4\text{-}10)$$

The solution is

$$\begin{aligned} f(r) &= \tfrac{1}{r}\sin kr \quad , \quad r < R \\ f(r) &= A_r \exp(-Kr) \quad , \quad r > R \end{aligned} \qquad (4\text{-}11)$$

where $$k = \left(\tfrac{2m}{\hbar^2} E_e\right)^{1/2} \qquad (4\text{-}12)$$

$$K = \left[\tfrac{2m}{\hbar^2}(V_0 - E)\right]^{1/2} \qquad (4\text{-}13)$$

Defining $k = Xk_0$, we obtain $K = (1-X^2)^{\frac{1}{2}} k_0$ (4-14), (4-15)

The boundary conditions at r=R lead to

$$\cot Xk_0 R = -\frac{(1-X^2)^{1/2}}{X} \qquad (4\text{-}16)$$

and $$E_e = X^2 V_0 \qquad (4\text{-}17)$$

Now the total energy of the bubble is the sum of the electronic energy and the mechanical energy needed to form a bubble:

$$E_t = X^2 V_0 + \tfrac{4\pi}{3} R^3 P \qquad (4\text{-}18)$$

(We neglect surface tension because we are in a gas, not a liquid--any surface term would be very small at most pressures to be considered, but not so for the 4.18K isotherm.) This may be rewritten as

$$E_t = V_0\left[X^2 + \tfrac{4\pi}{3}\beta^{3/2}\left(P/V_0\right)^{5/2}(k_0 R)^3\right] \qquad (4\text{-}19)$$

where $\beta = \hbar^2/2m$

The equilibrium radius is found from the condition $\partial E_t/\partial R = 0$, which gives

$$2X\left(\frac{\partial X}{\partial R}\right) + 4\pi\beta^{3/2}\left(P/V_o^{5/2}\right) k_o^3 R^2 = 0 \qquad (4\text{-}20)$$

Equation (4-16) gives

$$\frac{\partial X}{\partial R} = -\left[\frac{X k_o (1-X^2)^{1/2}}{k_o R (1-X^2)^{1/2}+1}\right] \qquad (4\text{-}21)$$

Together we have

$$f(X) \equiv 2\pi\beta^{3/2} P/V_o^{5/2} \qquad (4\text{-}22)$$

$$= \frac{2\pi}{\beta} P/k_o^{5/2}, \quad \text{as } V_c = \beta k_o^2 \qquad (4\text{-}23)$$

$$= \frac{X^2 (1-X^2)^{1/2}}{k_o R\left[k_o R (1-X^2)^{1/2}+1\right]} \qquad (4\text{-}24)$$

At this point we leave the above mentioned reference and strike out on our own. The quantity we are interested in is

ΔF = change in Helmholtz free energy between the free and bubble states

$$= V_o - E_t \qquad (4\text{-}25)$$

$$= V_o\left[(1-X^2) - \frac{4\pi}{5}\beta^{3/2}\left(P/V_o^{5/2}\right)(k_o R)^3\right] \qquad (4\text{-}26)$$

$$= V_c\left[(1-X^2) - \frac{2}{3} f(X)(k_o R)^3\right] \qquad (4\text{-}27)$$

Using the expression (4-24) in (4-27), we obtain after some algebra

$$\Delta F = V_o\left\{1 - X^2\left[\frac{5/3 (k_o R)(1-X^2)^{1/2}+1}{(k_o R)(1-X^2)^{1/2}+1}\right]\right\} \qquad (4\text{-}28)$$

The process of evaluating ΔF proceeds as follows:

(i) r_s is obtained from (4-1)
(ii) k_o is obtained from (4-8)
(iii) V_o is obtained from (4-7)
(iv) $f(x)$ is determined by (4-24)
(v) (4-16) provides a relation between X and $(k_o R)$
(vi) X and $(k_o R)$ are then determined by (4-22); since k_o is known already, R is now known
(vii) ΔF is finally determined by (4-28)

In order to calculate the mobility itself, we use the result of Young's phenomenological theory[52] (an equation also given by Levine[2])

$$\mu = \left[\frac{1+(\mu_0/\mu_i)\exp(\Delta F/kT)}{1+\exp(\Delta F/kT)}\right]\mu_i \qquad (4\text{-}29)$$

where μ_f=mobility of a free electron (which for the moment we take to be given by the semi-classical mobility, equation (3-1))
μ_b=mobility of an electronic bubble (see below)

This equation is derived from Young's two assumptions, that (i) there exist two unique electronic states, characterized by the mobilities μ_b and μ_f, and (ii) these states can be characterized by thermodynamic relaxation times τ_{fb} and τ_{bf}, where $\tau_{fb}(\tau_{bf})$ is the characteristic free to bubble (bubble to free) decay time, related by $\tau_{bf}/\tau_{fb} = \exp\left(\frac{\Delta F}{kT}\right) = n_b/n_f$, where n_b and n_f are the populations of the bubble and free states. (This ignores any effective mass or density of states effects.)

The bubble mobility is calculated from Levine's[1,2] interpolation formula

$$\mu_b = \frac{e}{6\pi\eta R}\left[1 + \frac{9\pi\eta}{4\rho R(2\pi MkT)^{1/2}}\right] \qquad (4\text{-}30)$$

where η=viscosity of the gas
R=radius of the bubble
M=atomic mass of helium-4

Values of the viscosity are obtained from reference 53. Note that Levine and Sanders[1,2] used the classical turning point radius for R rather than the bubble radius.

Figure 24 shows the measured mobility curve at 3.96K, as well as the predicted curve from this theory, marked square well. (The other curves will be explained later in this chapter.) (Note that the "measured" curve is actually a rough interpolation between the data of Levine and Sanders[1] at 3.902 and 4.18K--which was quite close to my data at 4.18K; for some reason, the theory of Neustadter and Coopersmith[54] was done for 3.96K, and we wished to compare our calculations at the same temperature.) The density at the saturated vapor pressure at 3.96K is 19.85×10^{20} cm^{-3}, so the curves shown could not be extended

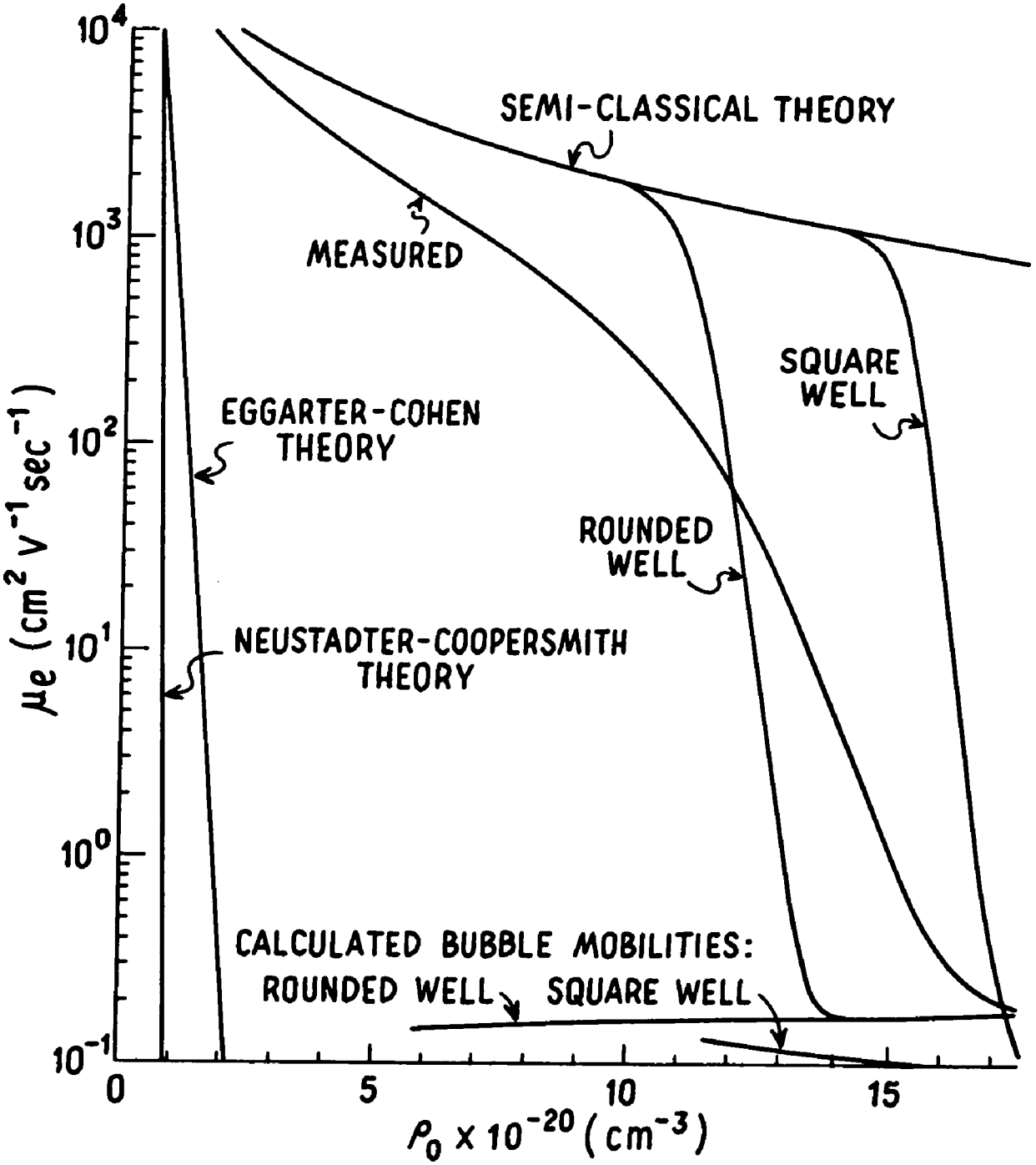

Fig. 24: Electron mobility versus number density in helium-4 at 3.96K--measured values and various theories. The Eggarter-Cohen and Neustadter-Coopersmith theories are scattering theories; the square and rounded wells are bubble model theories.

much further in any case. The calculated curve seems to be dropping well below the measured curve at the end, but of course it only goes down to μ_m which is a roughly flat curve at about 0.1 $cm^2V^{-1}sec^{-1}$.

Actually we have left out a term in the free energy

$$\Delta F_{Translation} = +\frac{3}{2}kT \ln \frac{m_b}{m} \qquad (4\text{-}31)$$

from equation (4-28), which should have been included. This term arises from the free energy associated with the translational states of the electron,

$$\Delta F_{Translation} = -kT \ln \frac{V}{h^3}(2\pi m kT)^{3/2} + kT \ln \frac{V}{h^3}(2\pi m_b kT)^{3/2} \qquad (4\text{-}32)$$

("We assumed that the electron wave function was centered around some point in the gas. In reality, all parts of the system are equivalent except for the region very close to the walls, and this fact must be allowed for."[2]) Now m is the electronic mass (free electron), while m_b is the effective bubble mass, taken to be equal to m plus one-half the mass of the displaced gas, according to the usual hydrodynamic prescription. However, since we are not in a purely hydrodynamic regime, it is a bit uncertain just what to take for this mass. (Notice that Levine and Young have opposite sign conventions for ΔF, and we are following Young's usage.) If this term were included, the calculated curve would simply "drop off" more steeply than it already does.

Before leaving the square well, I would like to make one final remark. The f(X) function of (4-24) exhibits a maximum value of 4.4998×10^{-2} at X=.965. This means that there are many points in the ρ-T plane where binding simply does not occur, and the mobility is just the free mobility. Where the calculated curve in Figure 24 departs from the semi-classical curve shows where binding just begins in

helium-4 at 3.96K. The locus of points satisfying

$$\frac{2\pi}{\beta} P/k_o^5 = \frac{4\pi a}{h^2} P/k_o^5 = 4.4998 \times 10^{-2} \qquad (4\text{-}33)$$

is plotted in Figure 25. (A similar limit on binding to the potential well in the rounded well case occurs also, as shown in the figure, and as will be discussed in the next subsection.) Also shown are the coexistence curves for helium-4 and hydrogen, as in Figure 21, showing once again that perhaps the most interesting region to study is forbidden in the case of hydrogen. A curve showing where binding begins for the square well for hydrogen could have been calculated, but what value to take for the scattering length a was not certain (see subsection 3.2.3 for uncertainties in the cross-section, and hence the scattering length, of electrons in hydrogen). Notice that binding always occurs at a lower density for the rounded well than for the square well, at any given temperature. Finally, referring back to Figures 12 and 13, the downward pointing arrows indicate where binding just begins for the square well and the upward pointing arrows indicate the same thing for the rounded well. There does seem to be a good correspondence between this point for the rounded well and the onset of a sharp drop.

4.1.3 Spherical Rounded Well

The square well potential has already been treated, as indicated in the last subsection. In this subsection I will treat a new potential, which I call the rounded well potential. The basic physical ideas are quite similar to the square well case; it is the mathematics that is different, and therefore will be confined to the appendices. Appendix IV covers the derivation of the general formal expression for ΔF for any potential (as noted there, this was not required for the simple square well case). Appendix V covers the

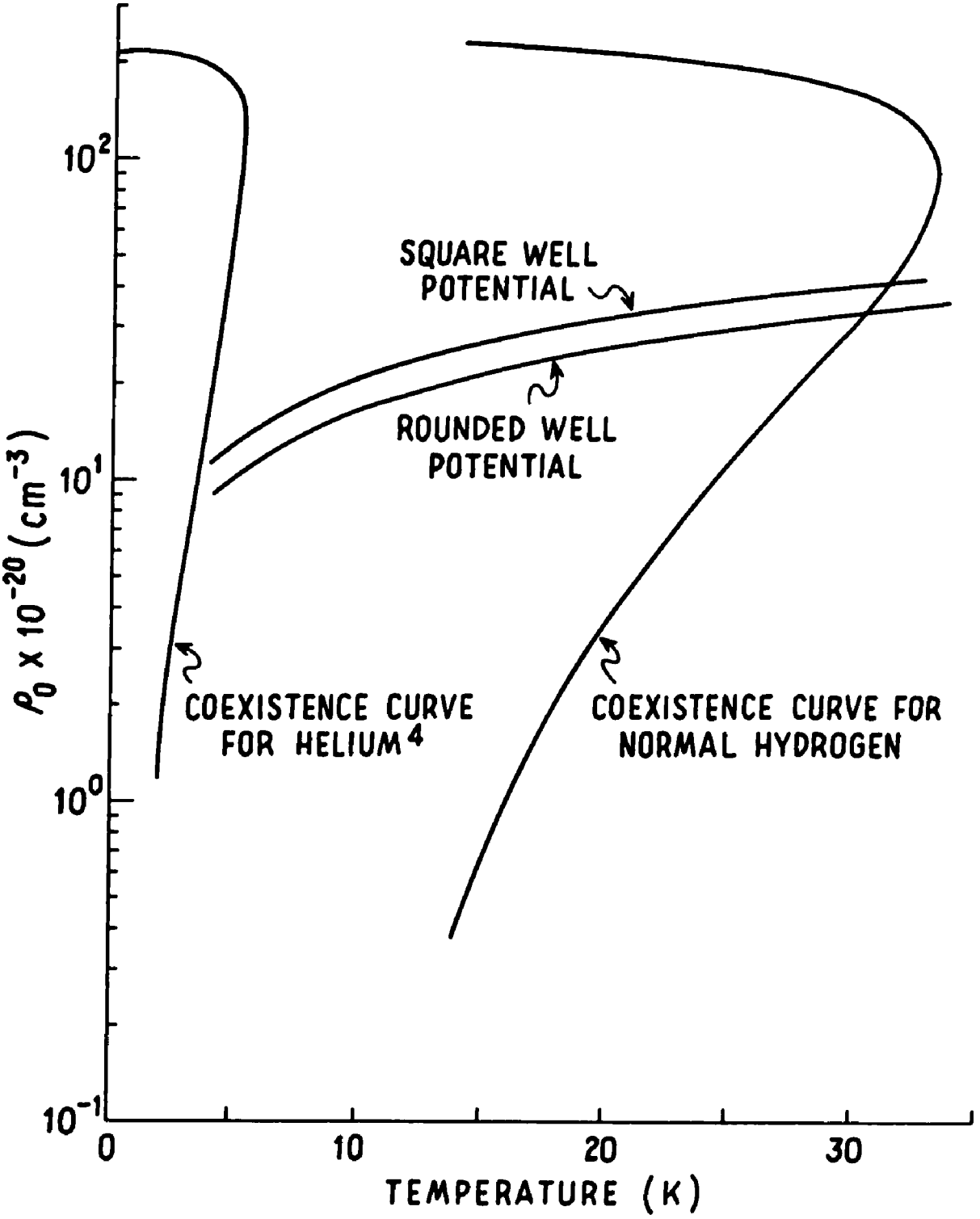

Fig. 25: Coexistence curves for helium-4 and normal hydrogen together with curves showing where binding just begins for two potentials for electrons in helium-4.

evaluation of ΔF for the rounded well potential

$$V = -V_0 / \cosh^2(r/r_0) \qquad (4\text{-}34)$$

Notice that only terms up to first order in the second virial coefficient are included in Appendix V. If the term to second order in B_1 (given in general form in Appendix IV) were included (which is easy), it would cause the theoretical curve of Figure 24, marked rounded well, to drop off even more sharply than it already does, so it was not included. In reference to Figure 24, the same general method was used to calculate the rounded well curve as was used for the square well curve, namely, the use of equations (4-29) and (4-30) and the semi-classical mobility for μ_ξ. (Note that r_0 was used for R in (4-30) for the bubble mobility, which means that the curve does not necessarily represent the actual mobility; only the range over which the drop occurs is really meaningful.)

It is evident from Figure 24 that the rounded well curve has a shape or width very close to that of the square well curve; the measured curve rises much more slowly than either of these theoretical curves. Thus it appears that the rounded well model is no great improvement on the square well model; I shall return to this point shortly.

A better fit can be achieved if some value other than the semi-classical prediction is used for μ_ξ. In particular, Young[52] uses

$$\mu_\xi = 2\mu_0 / \{2 + [4 + (\mathcal{E}/\mathcal{E}_1)^2]\}^{1/2} \qquad (4\text{-}35)$$

where μ_0 is the low field free electron mobility and $\mathcal{E}_1$ is determined by

$$\mu_0 \mathcal{E}_1 (3m/kT)^{1/2} = 1 \qquad (4\text{-}36)$$

where m is the mass of the electron. ("The parameterization of μ_ξ is chosen on the basis that it is capable of fitting the first principles calculation of Hargenau[55] to an accuracy of 1%.") "We assume that the

functional dependence of μ_f with respect to $\mathcal{E}$ is independent of the density of the helium gas while μ_o has a density dependence which we obtain by fitting the experimental data of v_d versus $\mathcal{E}$ in the high $\mathcal{E}$ region, i.e. where $v_d \sim \mathcal{E}^{\frac{1}{2}}$. Thus, in essence, an experimental rather than a theoretical value is being used for μ_f. The results of using this μ_f are shown in Figure 26, with all conditions the same as for Figure 24. Also shown for comparison are $\mu_{\text{semi-classical}}$ and $\mu_{\text{Legler theory}}$; the latter is discussed in Appendix VII. The improvement of the fit at the high mobility end is significant, which perhaps is not so apparent on a semi-log plot. It may be possible to derive this μ_o curve on the basis of a scattering theory like Legler's.[40] This point will be raised again in section 4.2 on scattering models, and in Appendix VII.

Finally, just as in the square well case, the function f(z), specified by equations (V-43) and (V-44) has a maximum value of 3.331×10^{-3}, which occurs at z=12.67. So the locus of points satisfying

$$\left(\frac{2m}{\hbar^2}\right)\left(\frac{\pi^3}{16}\right)\left[.1647 + .26138\, B_1 \rho_\infty\right] kT \frac{\rho_\infty}{k_o^5} = 3.331 \times 10^{-3} \qquad (4\text{-}37)$$

is the curve shown in Figure 25 for the rounded well.

4.1.4 Self-Consistency Calculation

Levine and Sanders[1,2] derived a self-consistent set of equations for the electron wavefunction ψ and the gas density $\rho(r)$. We present here an alternative derivation. To begin,

$$-\frac{\hbar^2}{2m}\nabla^2\psi + V\psi = E\psi \; ; \quad V = \left(\frac{\hbar^2}{2m}\right) 4\pi a\, \rho(r) \qquad (4\text{-}38)$$

Note that this potential V is not the same as that given by (4-7), the latter being derived from the Wigner-Seitz model. This V in (4-38) is from the optical model; in Appendix VI it is shown that they are the same to first order. Now if a helium atom is placed at R_1, the energy

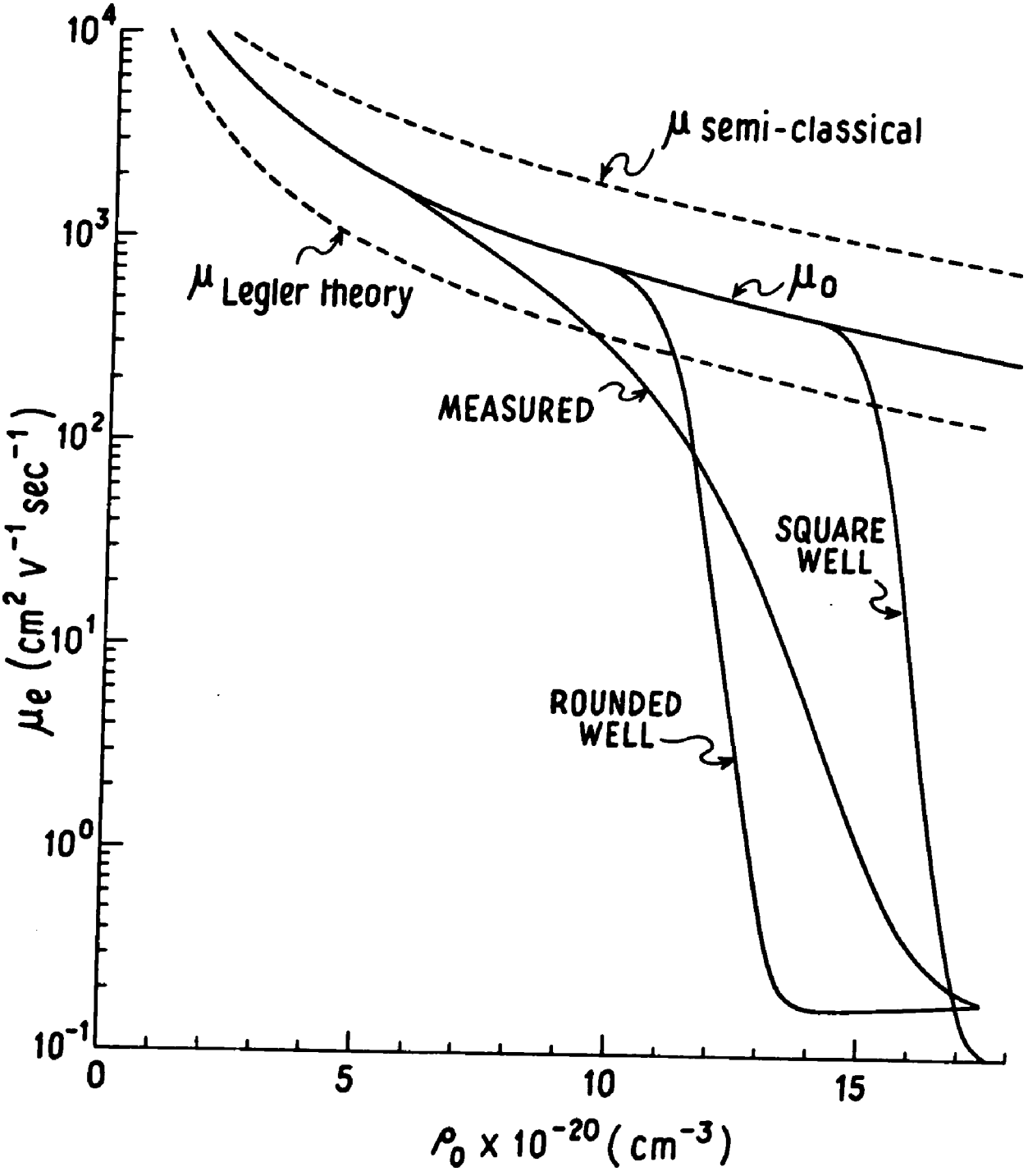

Fig. 26: Electron mobility versus number density in helium-4 at 3.96K--measured values and square and rounded well bubble model predictions using Youngs's μ_o.

of the system will be raised by

$$\Delta V_i = \left(\frac{\hbar^2}{2m}\right) 4\pi a |\psi(r_i)|^2 = \frac{V_{optical}}{\rho} |\psi|^2 \qquad (4\text{-}39)$$

We have the general expression for the chemical potential μ_c[56]

$$\mu_c = kT \ln P(r) + B_1(T) P(r) + \chi(T) + \mu(r) \qquad (4\text{-}40)$$

In our case,

$$\mu(r) = \frac{V_{optical}}{\rho} |\psi|^2 = \frac{2\pi\hbar^2}{m} |\psi(r)|^2 \qquad (4\text{-}41)$$

and, since μ_c is constant throughout the system

$$\mu_c = \mu(r) + \mu(r) = \mu_0 \qquad (4\text{-}42)$$

Combining these,

$$kT \ln P(r) + B_1(T) P(r) + \chi(T) + \frac{V_{optical}}{\rho} |\psi|^2 = kT \ln P_0 + B_1(T) P_0 + \chi(T) \qquad (4\text{-}43)$$

Using the equation of state

$$P = \rho kT (1 + B_1 \rho) \qquad (4\text{-}44)$$

this can be reduced to

$$kT \ln \frac{\rho(r)}{\rho(0)} + 2kTB_1[\rho(r) - \rho(0)] = -\frac{2\pi\hbar^2 a}{m} |\psi(r)|^2 \qquad (4\text{-}45)$$

Dropping the term with the virial coefficient as it is usually small compared to the other, we find

$$\rho(r) = \rho(0) \exp\left\{-\frac{2\pi\hbar^2 a}{m} |\psi(r)|^2\right\} \qquad (4\text{-}46)$$

This set of non-linear equations is too difficult to tackle directly. However, it can be approached with an iterative procedure. A given $\rho(r)$ is taken, and $\psi(r)$ is calculated for it. Then (4-46) is used to compute a new $\rho(r)$, and so on. This has been done in Appendix VI. The results are shown in Figures 27 and 28. Notice in Figure 28 of $\rho(r)/\rho(0)$ versus r that the new $\rho(r)$ does not go to zero at the origin--it can not unless the argument of the exponential in (4-46) goes to minus infinity. Further comments about the shape of these density distributions will be made in the next subsection.

Clark[57,58] has already set up simultaneous equations for the

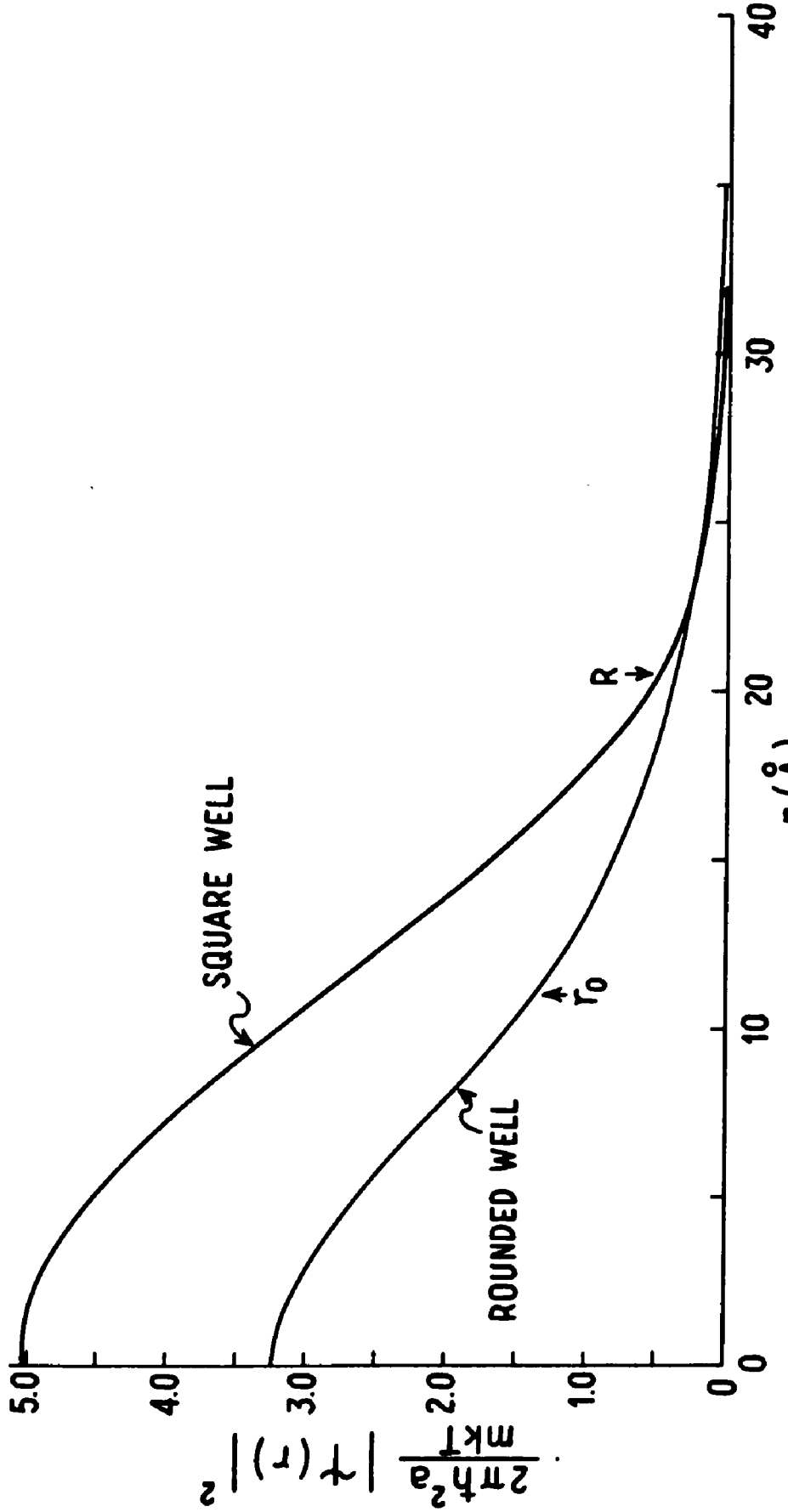

Fig. 27: The electron wave function squared versus radius for helium-4 at 4.18K and the saturated vapor pressure, for both the square and rounded well models (both are normalized). R and r_o are the characteristic sizes for the two potential models.

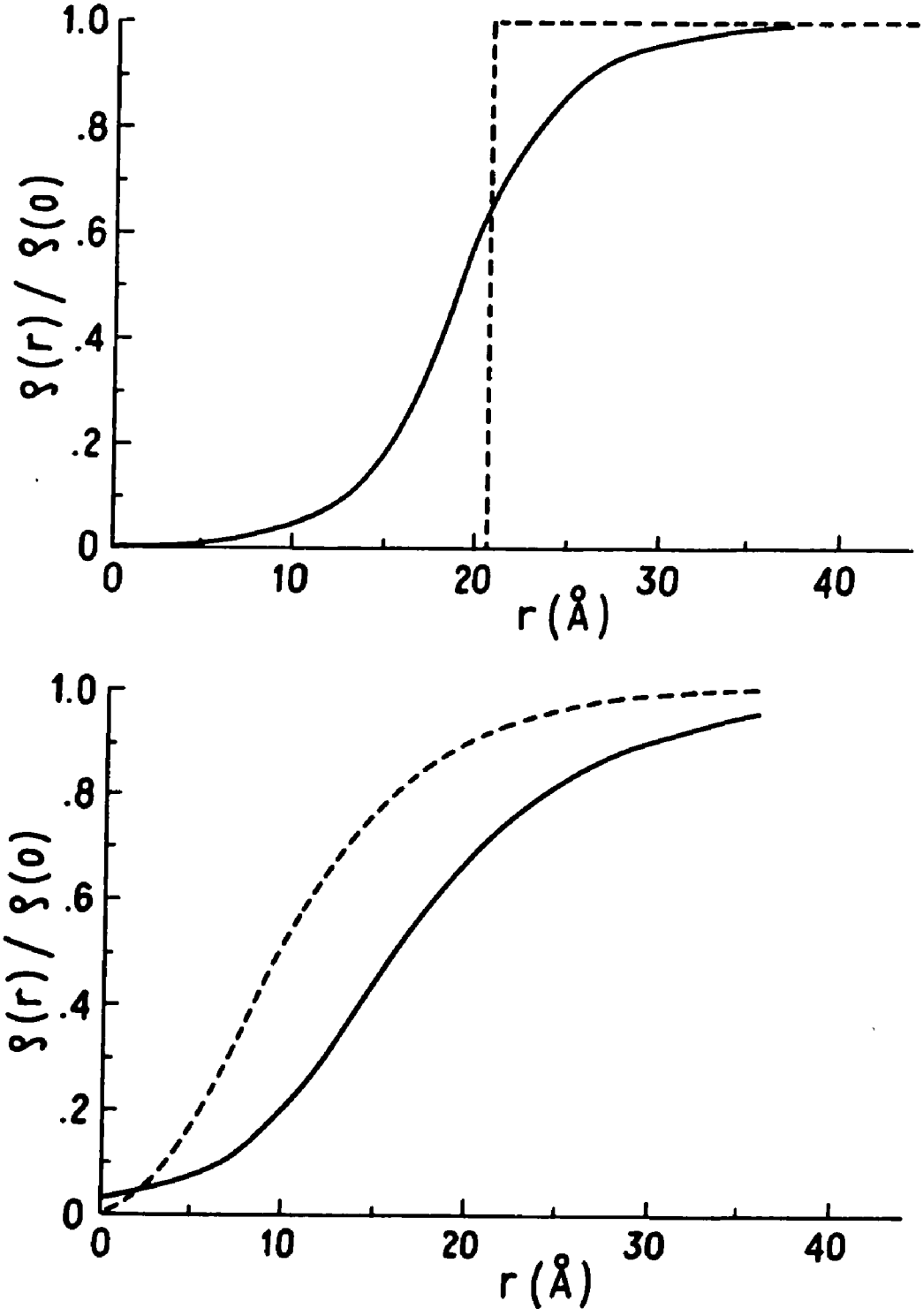

Fig. 28: Initial density distribution (dashed) and recalculated density distribution (solid) in helium-4 at 4.18K at the saturated vapor pressure. Upper graph--square well; lower graph--rounded well.

bubble model in helium and solved them on an analogue computer. He finds (for liquid helium) that the quantity equivalent to my $\rho(r)/\rho(0)$ is more "squared-off" than my $\rho(r)/\rho(0)$, being essentially zero for r less than 10Å and essentially unity for r greater than 15Å.

We can discuss the problem more analytically in certain limiting cases. If $|\psi(r)|^2$ in (4-46) is about

$$|\psi(r)|^2 \longrightarrow \infty, \quad r<R$$
$$|\psi(r)|^2 \longrightarrow 0, \quad r>R \tag{4-47}$$

then a square well results. If

$$\frac{2\pi\hbar^2 a}{mkT}|\psi(r)|^2 \ll 1, \quad \text{all } r \tag{4-48}$$

then we may expand the exponential to

$$\rho(r) \simeq \rho(0)\left(1 - \frac{2\pi\hbar^2 a}{mkT}|\psi(r)|^2\right) \tag{4-49}$$

Note that ρ_0 is the starting density (a function of r) and $\rho(r)$ is the density after one iteration. This equation means there is a characteristic length, or range, of the electron's influence on the gas given by

$$l \sim \left(\frac{2\pi\hbar^2 a}{mkT}\right)^{1/3} = \left(\frac{V_0}{\rho kT}\right)^{1/3} = \left(\frac{4\pi}{3}\frac{V_0}{kT}\right)^{1/3} r_s \tag{4-50}$$

If there is going to be an appreciable bubble, the characteristic length of the potential, r_0, must be comparable to this length. Inserting (4-49) into (4-38) yields

$$E'\psi(r) + \frac{\hbar^2}{2m}\nabla^2\psi(r) + \left(\frac{2\pi\hbar^2 a}{m}\right)^2 \frac{\rho_0}{kT}|\psi(r)|^2\psi(r) = 0 \tag{4-51}$$
$$\text{where} \quad E' = E - \frac{2\pi\hbar^2 a}{m}\rho_0$$

Interestingly, this is of the same form as the Gross-Pitaevskii[59,60] equation which is for a microscopic model for superfluid helium:

$$\left(i\hbar\frac{\partial}{\partial t} + \frac{\hbar^2}{2m}\nabla^2\right)\psi(r,t) - V_0|\psi(r,t)|^2\psi(r,t) = 0 \tag{4-52}$$

Note that this is the equation used by Clark.[57] We now have a time-dependence, but $i\hbar\frac{\partial}{\partial t}\psi(r,t)$ is equivalent to our $E'\psi(r)$. Perhaps more

seriously for a direct usage of known solutions to the Gross-Pitaevskii equation is the difference in sign between the V_o term in (4-52) and the equivalent term in (4-51).

Finally we might note that at least we are considering stationary states. If we had to consider wavefunctions like

$$\psi(r) = \psi_o(r)\, e^{i k \cdot r} \qquad (4\text{-}53)$$

and use perturbation theory, we might have an even worse problem than the coupled equations described above. Also (4-53) must certainly be used in order to arrive at the density of states or the electron effective mass.

4.1.5 Comments on Other Bubble Models

Looking at Figure 26, it appears that the rounded well gives a fair approximation to the measured mobility at high mobilities, and the square well gives a fair approximation at low mobilities. This is as we would expect physically, namely, that when the bubble first forms it will be smeared out and diffuse, but that it becomes more and more "squared-off" as the density is increased. Thus, some sort of transition from the rounded well to the square well should represent the physical situation in the intermediate region, and looking at Figure 26, that seems to be the case. A true square well can never be self-consistent, of course, but the actual self-consistent result presumably will start to look more and more "squared-off" for increasing densities. It would seem best to try to treat a density distribution that has two parameters to characterize the well--one for the approximate width of the flat part of the well, and one to characterize the shape or width or the well. In other words, a density distribution of the shape of an inverted Fermi-Dirac density of states distribution function. A look at Figure

28 indicates further that this is called for. Also notice that in Figure 28 the well is not "swept clean" at the center--the density is non-zero there after one iteration of the equations given in the last subsection. So a third parameter is called for. A potential of this sort, the Saxon-Woods potential used by nuclear physicists, is a good candidate. However, no attempts have been made to use it as the calculations would all have to be done a on a digital computer (the electronic energy and wave function, the energy to form a bubble, and all the iterations). Conceivably an imaginatively programmed analogue computer could be used, as was done by Clark.[57,58]

As a note, the density distribution

$$\rho(r) = 0, \quad r < R_0$$
$$\rho(r) = \rho_0\{1 - [1 + \alpha(r-R_0)]\exp[-\alpha(r-R_0)]\}, \quad r > R_0 \tag{4-54}$$

has been treated.[61,62] (Notice that this reduces to the square well for $\alpha \to \infty$.) The energy to form a bubble is easily evaluated, and is found to be

$$E_b = \frac{4\pi}{3} P r_0^3 \left[1 + \frac{6}{\alpha R_0} + \frac{18}{(\alpha R_0)^2} + \frac{24}{(\alpha R_0)^3}\right] \tag{4-55}$$

The electronic energy appears to have been evaluated on a computer. The resulting fit is some improvement over the square well case. Note that this is the first attempted two-parameter bubble model that has been treated, as far as I know.

4.2 Scattering Models

Scattering theories represent a totally different way of looking at the problem. The classical theory for the mobility is of course a simple scattering theory. The semi-classical theory by Levine, equation (3-1), and the more general theoretical equation (3-2) by Lekner are also scattering theories. But the first scattering theory

(known to us) for a system of randomly located scatterers, leading to a large drop in mobility at a characteristic density is that of Neustadter and Coopersmith.[54] The mobility is calculated to all orders in the density of scatterers. Their calculated curve is shown in Figure 24. There are several things to notice about this curve: (i) at very low densities it agrees with the classical prediction, (ii) it departs from the classical prediction at a much lower density than does the actual measured curve, and (iii) it falls at a nearly exponential rate, with no lower limit, in contrast to the case of the measured curve and various bubble models. "The poor quantitative agreement is thought to arise from the lack of excluded volume between the scatterers (omission of the hard-core helium-helium interaction) which permits configurations contributing very strongly to the scattering."[54] In addition to this, another possible reason for the disagreement is that the scattering centers are static; they do not change in time as they do in a real gas. This perhaps explains why the predicted mobility has no "floor"--once an electron is trapped by some spatial configuration of scatterers, it can not escape.[63] Also, the electrons can not affect the static scattering centers (either by their wave functions directly, or by polarization effects), which is also very unrealistic physically. (The same comments apply to the Eggarter-Cohen theory immediately below.)

Eggarter and Cohen[64] have developed a model which is more easily understood than that of Neustadter and Coopersmith. Their abstract is the best summary of their theory: "A semiquantitative model for the density of states and transport properties of an electron in a system of randomly located hard core scatterers is given. Our main results are: (a) The density of states has the usual square root

behavior for high energies and a tail of localized states at the low energy end; the energy at which the transition from localized to extended states occurs is computed from percolation theory. (b) For a fixed temperature the fraction of electrons in localized states is extremely small below a certain critical density of scatterers and increases drastically above this critical density. Thus, our model provides a physical explanation for the mobility transition found by Neustadter and Coopersmith.* Their calculated curve is shown in Figure 24, and the descriptive remarks about the Neustadter-Coopersmith theory in the preceeding paragraph apply here as well. Eggarter and Cohen predict that the transition from high to low mobility should occur at roughly

$$\rho^{5/4} T^{-1} \backsim \left(\frac{2m}{\hbar^2}\right) \frac{3^{3/4}}{(4\pi a)^{7/4}} \qquad (4\text{-}56)$$

Figure 29 shows a universal curve of the mobility (divided by the classical prediction) for the theory versus $\rho^{5/4}T^{-1}$; also shown are some of my data points. It will be seen that the theory predicts a curve of the correct general shape, but is a couple of orders of magnitude off quantitatively. Also notice in Figure 16 that a plot of (4-56) would be a line running almost straight upward and close to the temperature axis.

A different characteristic parameter for the onset of the transition can be found by combining our characteristic length from (4-50) with the Eggarter-Cohen theory. Their parameter for the onset of the transition is

$$\frac{V_o}{\langle N\rangle^{4/3} kT} \backsim 1 \qquad (4\text{-}57)$$

where $\langle N\rangle$ is the average number of particles in one of their elementary cells, that is

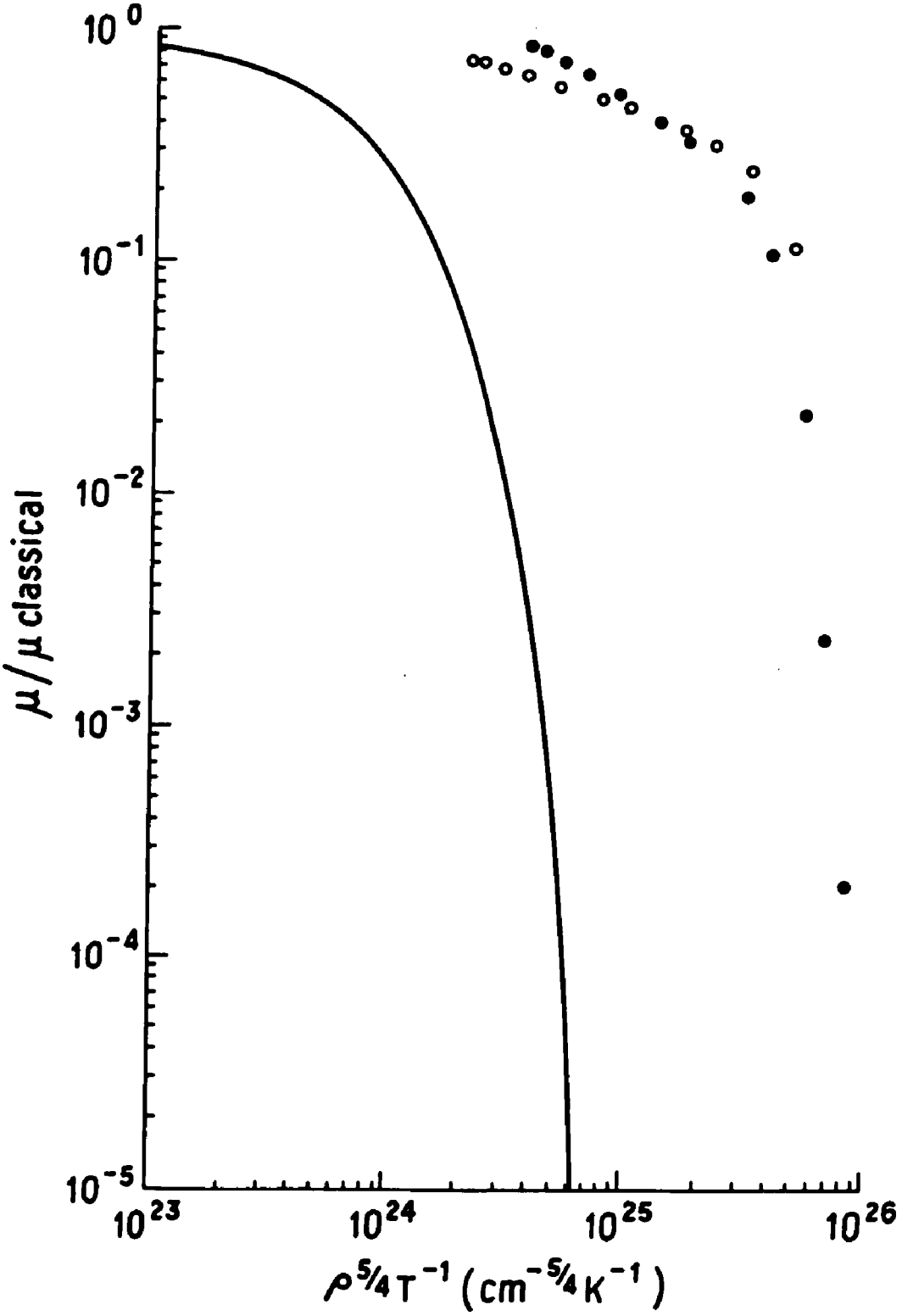

Fig. 29: Electron mobility in helium-4 divided by the classical value. Solid line, universal curve prediction of the Eggarter-Cohen theory; open and solid circles, data points from temperature sweeps at $\rho = 10 \times 10^{20}$ cm^{-3} and 14×10^{20} cm^{-3}, respectively.

$$\langle N \rangle = \rho_0 \ell^3 \tag{4-58}$$

Combining (4-50), (4-57), and (4-58) yields

$$\frac{V_0}{\rho_0^{1/2}\left(\frac{V_0}{\rho_0 kT}\right)^{1/2} kT} = \left(\frac{V_0}{kT}\right)^{1/2} \leq 1 \quad \text{or} \quad V_0 \leq kT \tag{4-59}$$

This is just the criterion found by Neustadter and Coopersmith,[54] and also by Legler[40] (as seen after a little rearrangement)--and they disagree with experimental results, of course.

Before these scattering theories are simply dismissed as being a much worse fit than the bubble models, it is well to remember that they are well thought out theories, and that if they are in disagreement with measurements, there may be some serious underlying physical problem. It has been suggested that correlated scattering is the cause of the departure of the measured mobility from the semi-classical prediction which occurs even before the sharp downward transition, an effect mentioned in subsection 4.1.3. Then as the density becomes greater, where the various bubble models begin to become important, there could be a sort of hydrodynamic flow pattern moving around the electron, "sweeping" scattering centers out of the way and making them ineffective.[65] (In a solid, for which these theories were originally designed, this of course would not happen. The theory also seems to work better for a solid.) However, at the moment this is inconclusive.

It is well to point out what is contained implicitly in the above, namely that we probably have <u>two</u> phenomena at work in the problem, scattering at low densities and bubble formation at higher densities. If a very good model could be developed for one of these phenomena (say bubble formation), its effect could be "subtracted out" from measured values leaving mobility effects due solely to the other

phenomenon (scattering). This would mean being left with Young's[52] curve (an experimental curve really), shown in Figure 26, to calculate, at the least. An attempt to calculate this μ_e curve on the basis of Legler's[40] theory is presented in Appendix VII.

4.3 Electric-Field Dependent Mobility Measurements

A possible test of various mobility theories is how well they can explain the various v_d versus $\mathcal{E}$ curves observed by Levine and Sanders,[1,2] which bend in various ways. All apparently have a region where $v_d \propto \mathcal{E}$ near the origin and a high field region where $v_d \propto \mathcal{E}^{1/2}$. In particular we discussed in subsection 3.1.2 the equation

$$\sqrt{M/m}\; e\mathcal{E}\lambda \backsimeq kT \tag{4-60}$$

For the Eggarter-Cohen theory, we can postulate that the break in the v_d versus $\mathcal{E}$ curve occurs when the energy gained in one mean free path is roughly equal to the smearing of the band edge where localized states appear:

$$e\mathcal{E}\lambda \backsimeq \frac{V_o}{\langle N\rangle^{1/2}} \tag{4-61}$$

V_o is given by the optical potential,

$$V_o = \left(\frac{\hbar^2}{2m}\right) 4\pi a \rho \tag{4-62}$$

and $\langle N\rangle$ is the mean number of atoms in one of the elementary cells:

$$\langle N\rangle \backsimeq \left[\left(\frac{3}{4\pi a}\right)^{1/3} \frac{1}{\rho}\right]^{1/2} \tag{4-63}$$

Combining the last three equations yields

$$\mathcal{E} \backsimeq \left(\frac{\hbar^2}{2m}\right)\left(\frac{4\pi a}{3}\right)^{3/4} \frac{16\pi^2 a^3}{e} \rho^{9/4} \tag{4-64}$$

The three curves presented by Levine and Sanders[1,2] do seem to roughly obey the form $\mathcal{E} \propto \rho^{9/4}$ even if the constant is not correct; however, there are not enough data to come to any conclusions. Also, we are near the percolation region and the temperature must play a role. Since field measurements are relatively easy to make, some theoretical predictions

in this area could be subjected to test.

4.4 Discussion of Mobility Data in Hydrogen

The high mobility branches of the data in Figure 22 for hydrogen are due to electrons, without question, as they match up with kinetic theory prediction at low densities. (A direct comparison with helium-4 is made in Appendix VII.) Similarly all the data in helium-4 are due to electrons, because all the data curves progress in a continuous fashion from a regime known to be due to electrons. However, what the low mobility branches of the hydrogen data are due to is not known. The three possibilities are electrons, heavy ions, or impurities. As discussed earlier in subsection 3.2.3, impurities can be ruled out, leaving only electrons and heavy ions as possibilities.

Figure 30 shows the radious of the low mobility object versus number density using the interpolation formula of Levine and Sanders and the measured values of mobility:

$$\mu = \frac{e}{6\pi\eta R}\left[1 + \frac{9\pi\eta}{4\rho R(2\pi MkT)^{1/2}}\right] \qquad (4\text{-}65)$$

where η=viscosity
M=reduced mass (taken as one molecular mass)
R=radius

Both the viscosity value and the Enskog theory dependence of viscosity mentioned in Figure 30 are from reference 25. Plots using just the viscous term or just the kinetic theory term for a heavy object were very far away from the other curves in the picture and were not included. (They did not predict an R greater than 10Å at any point on the graph. The purely kinetic theory curve rose less steeply than the curve including both terms; the purely viscous curve, more steeply. For the purely viscous or hydrodynamic case to be valid, we require $\lambda_m \ll R$, where λ_m is the molecule-molecule mean free path. Following

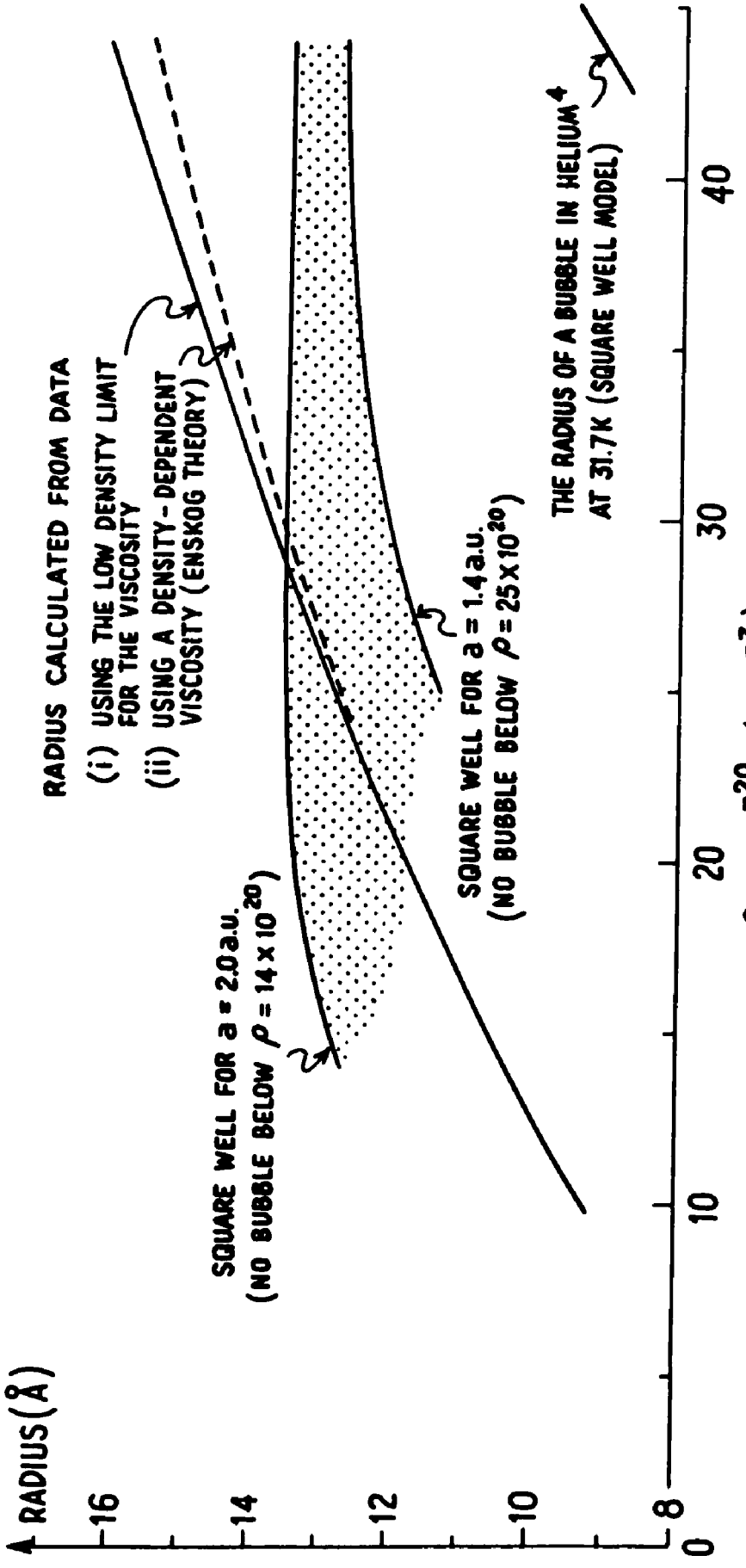

Fig. 30: Radius of the low mobility negative object in normal hydrogen at 31.7K versus number density, derived from

$$\mu = \frac{e}{6\pi\eta R}\left[1 + \frac{9\pi}{4\sqrt{5}R\,(2\pi MkT)^{1/2}}\right],$$

and various model predictions.

Dushman[66] we find λ_m=19.2Å at ρ=10x10^{20} cm^{-3}--of the same order as R, indicating we are in between the pure kinetic theory and pure viscous regions.) Also shown in Figure 30 are predictions for a square well bubble model (for electrons) for a=1.4a.u.=.740Å (experimental scattering length) and a=2.0a.u.=1.06Å (theoretical scattering length without polarization effects) for hydrogen. (The prediction for a square well bubble model for helium-4 is shown for comparison.) Notice that no bubbles form at densities lower than shown on the figure, whereas the experimental curve goes down to a lower density. In fact (see Figure 23) measurements could have been extended to even lower densities, but the importance of doing this was not realized at the time. Note that for a rounded well calculation, the calculated curves would extend to lower densities.

Another difficulty with electrons being the low mobility object is why two distinct electronic states should be seen simultaneously. One would expect to see some sort of average, unless the transition time between the states were very long indeed (of the order of a second). Figure 31 is a schematic illustration of a density profile for the rounded well bubble model, together with a plot of the free energy difference between extended state and localized state electrons, as a function of the characteristic length r_o of the rounded well. This is not like the usual problem of an electron tunneling through a potential barrier in real space, because this is a configuration energy diagram. The problem of calculating the transition time from one configuration to the other (stochastic process) is discussed by Donnelly[67] (the original treatment is by Chandrasekhar[68]). If the number of particles in a potential well is given by

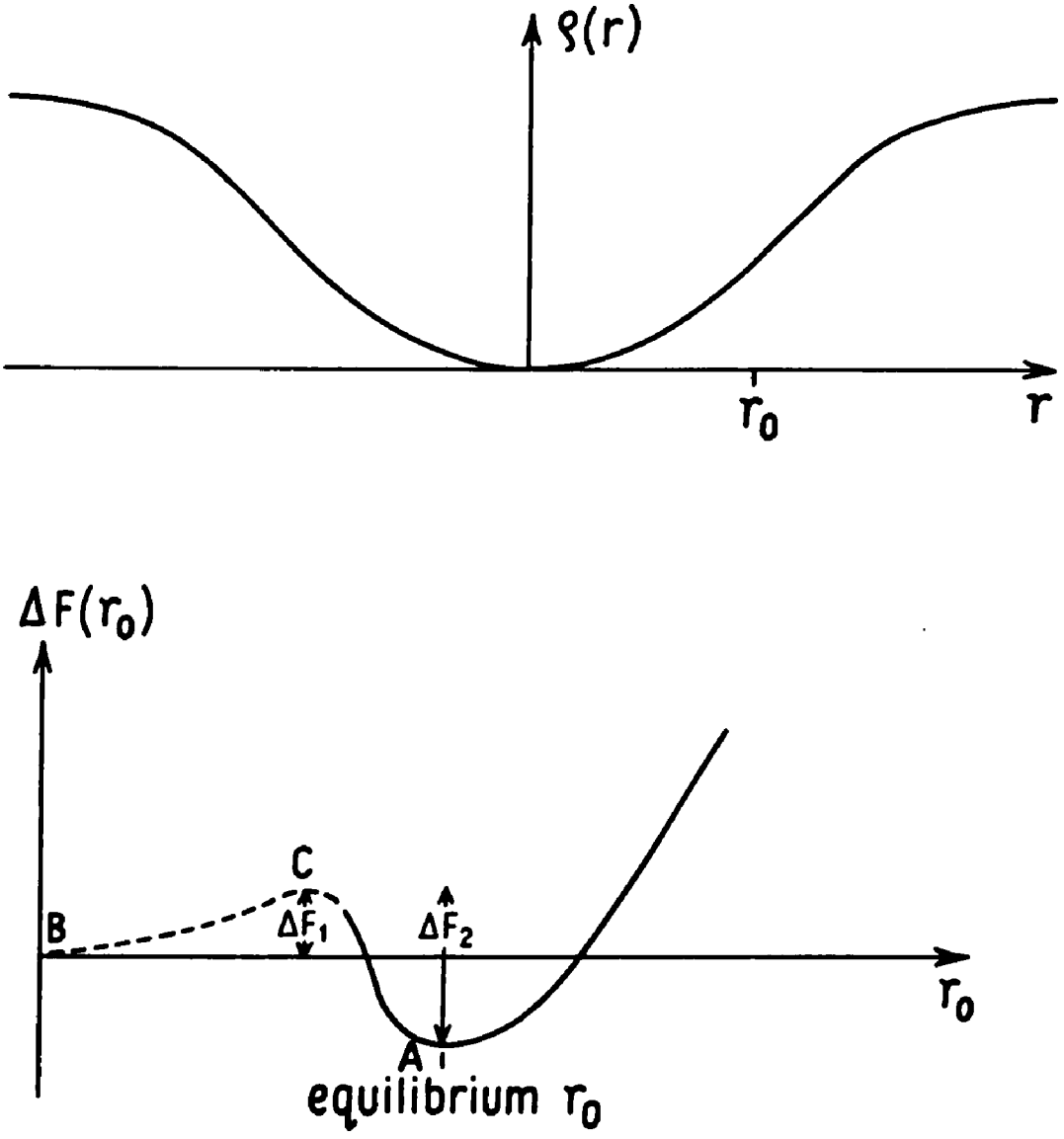

Fig. 31: Schematic illustration of a density profile $\rho(r)/\rho(\infty)=1-\cosh^{-2}(r/r_0)$ and of the free energy difference between free and localized electrons, the latter as a function of the r_0 of the former.

$$N(t) = N_0 e^{-Pt} \tag{4-66}$$

then the ratio of transition times is given by

$$\frac{P_{BC}}{P_{AC}} = \Lambda\, e^{(\Delta F_2 - \Delta F_1)/kT} \tag{4-67}$$

where Λ=geometrical factor depending on the shape of the potential curve

We have not attempted to calculate Λ because (i) we do not know the details of the $\Delta F(r_0)$ curve, which comes from the actual potential curves, and (ii) the electron is not interacting with a static potential, but is actively changing the shape of a proto-bubble to a full-sized bubble--that is, digging itself a hole in the fluid (and in fact may fail, and be ejected back to the free state immediately), meaning that the potential the electron sees is continuously changing.

There are also difficulties with the idea that the low mobility objects are ionic "snowballs" (cluster ions). H_2^- is a metastable ion and H^- is a stable ion. H_2^- has an electron affinity of about -2.5 eV (energy above H_2); H^-has an electron affinity of +.747 eV (energy below H).[69] If such an ion were involved, and if there were time for equilibrium to be established among the different species, we would expect a mass action law equation to be satisfied:

$$e^- + H_2 \rightleftharpoons H_2^- \tag{4-68}$$

$$\frac{[e^-][H_2]}{[H_2^-]} = K(T) = Ae^{-\Delta/kT} \tag{4-69}$$

where [ ] represents concentration, and Δ is some activation energy, which must involve V_0, which in turn is directly proportional to ρ in the optical model, equation (4-62). $[H_2]$ is just given by ρ itself. The concentrations are obtained from the measured signal strengths (intensity) and drift velocities (mobility/electric field):

$$\frac{(I_H/\mu_H \mathcal{E}_H)}{\rho\,(I_L/\mu_L \mathcal{E}_L)} = Ae^{-\Delta/kT}. \tag{4-70}$$

where the subscripts H and L refer to the high and low mobility

branches, respectively. Taking logarithms,

$$\ln \frac{[H_2^-]}{[e^-][H_2]} = \frac{\Delta}{kT} - \ln A \qquad (4\text{-}71)$$

Figure 32 shows $[H_2^-]/[e^-][H_2]$ plotted versus number density in an attempt to fit (4-71)--that is, to find some dependence between Δ and $\rho(V_o)$. There is a knee in the curve, so it does not seem that any simple relation will work. Of course, if the H_2^- ion is at the center of a snowball (and especially if the center is frozen as it is thought to be under some conditions, according to Kuper's theoretical treatment[3]) it is hard to see how equilibrium represented by (4-68) could be reached. It is conceivable that the important species is H^-, since the powerful radiation from the source will create just about every species possible in some concentration. In that case we would have

$$e^- + H \rightleftharpoons H^- \qquad (4\text{-}72)$$

$$\frac{[e^-][H]}{[H^-]} = A e^{-\Delta/kT} \qquad (4\text{-}73)$$

Unfortunately, [H] is not known, so no fit to these equations can be attempted.

Referring back to Figure 30, we see that the object we are talking about is at least 10Å in radius. Thus, if we have an ion, it must be a snowball to be so large, or else the cross-section is this big because of the range of the polarization potential. A snowball, formed by electrostrictive polarization forces according to Kuper, should exhibit only very small changes in radius with changing pressure, unless we are near the saturated vapor pressure curve. Levine and Sanders[70] attempted to explain some of their early data by assuming a small droplet of liquid forms on each electron. From cloud chamber theory we have

$$\ln (P/P_S) = \frac{1}{8kT}\left(\frac{2\gamma}{R} + \frac{\partial\gamma}{\partial R}\right) - \frac{\alpha e^2}{2R^4 kT} \qquad (4\text{-}74)$$

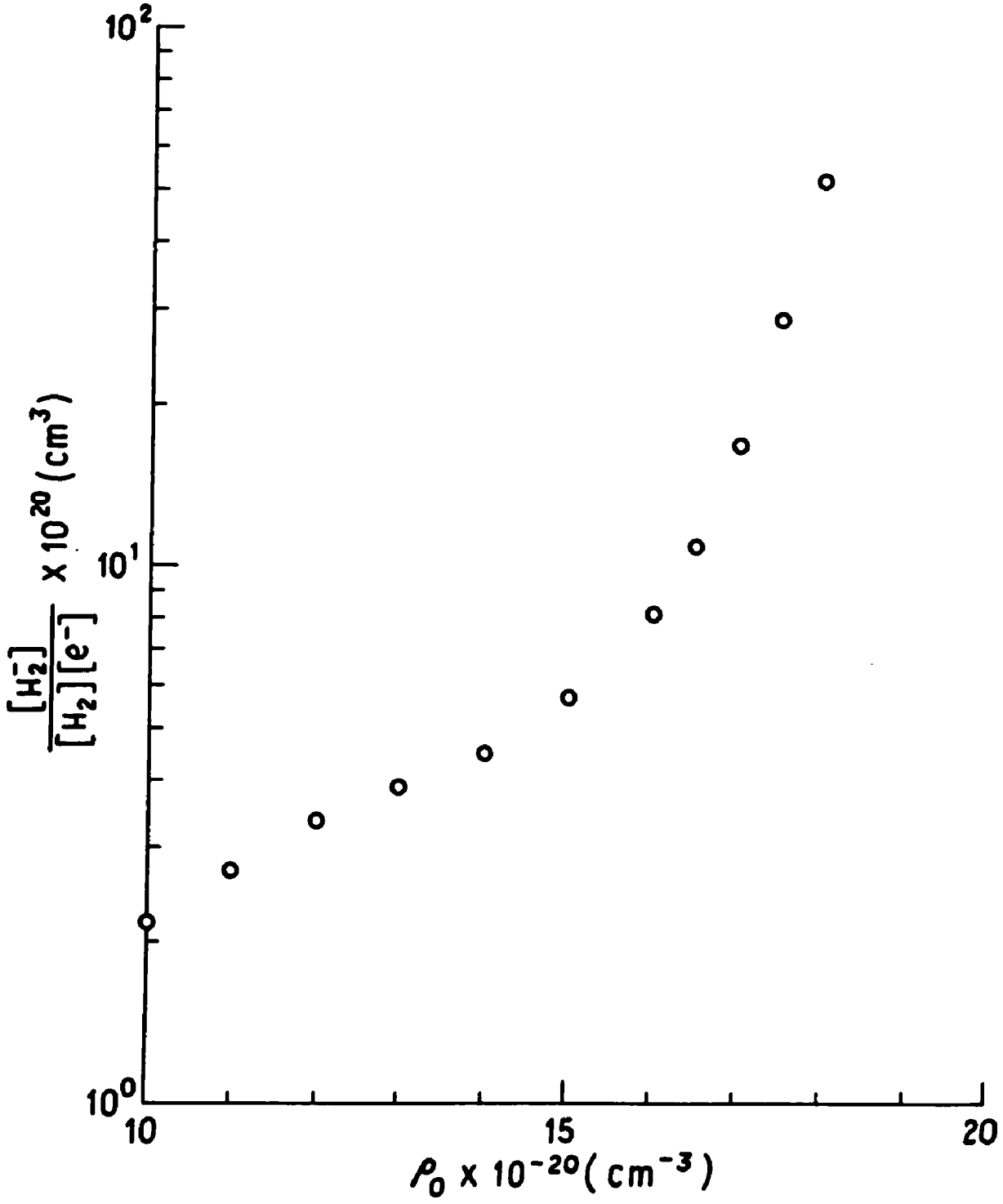

Fig. 32: Mass-action plot of the high and low mobility data in normal hydrogen at 31.7K-- $[H_2^-]/[H_2][e^-]$ versus number density.

where P_s=saturated vapor pressure
ρ=number density of the liquid at a given temperature
γ=surface tension
α=molecular polarizability
R=radius of the droplet

We neglect $\partial\gamma/\partial R$, and use (for hydrogen at 31.7K) γ=.1390 dyne/cm (reference 6) and α=.790Å^3 (reference 5). We find R increases from about 5.6Å at a gas density of 9.80×10^{20} cm^{-3} to 11.5Å at 45.2×10^{20} cm^{-3}. This change in radius is about of the correct magnitude and is increasing as the number density increases, as it should, but it lies below the radius calculated from the data. Note that there is no lower "cut-off" for this model, as is the case with any bubble model.

Thus we have seen that there are difficulties in interpreting the low mobility object as either an electronic bubble or an ionic snowball. To decide this question, the positive ionic mobilities should be measured in hydrogen. There should be very little difference between positive and negative ionic mobilities. Perhaps a very low energy electron source should be used, of such low energy ions would not be produced. (Of course, if a mass action equation held, no matter how low the energy of the injected electrons we would find ions.)

V. CONCLUSIONS

As I mentioned in the introduction, this study was undertaken to further our knowledge of the interaction of electrons with simple, dense materials. This I think I have done, but I have also raised more new questions than I have answered.

To summarize my work, I found in helium-4 that as the number density increased, (i) the mobility deviated gradually from the predicted value, (ii) then underwent a rapid drop, and (iii) finally flattened off to some low value. The first two effects become less pronounced as the temperature increases. An explanation in terms of a modified electron mobility (Young's[52] μ_e, perhaps explicable by an application of Legler's[40] theory) followed by the onset of bubble formation explains the data crudely, but better than any previous explanation. In general, sufficient data were accumulated to serve as a testing ground for various theories. In hydrogen, high and low mobility branches coexist over a fair range of density, in contrast to measurements on other substances. This phenomenon has not yet been adequately explained.

Scattered throughout the text I have made suggestions as to what might be done next in this area, and I would like to bring all these together here. Neon is an obvious candidate for study, the only outstanding simple substance predicted to have electronic bubbles. This would provide a more sensitive test of the theory of Springett, Jortner, and Cohen[5] on what is required to form electronic bubbles than any test carried out so far. There is one piece of evidence indicating neon may support electronic bubbles: "It is possible that the increase in the neon cross-section for momentum transfer found by Dougal[71] at 77K in the

pressure range 10 to 60 mmHg gas pressure is the result of just such multiparticle scattering effects."[72] More data are needed on hydrogen to see if the low mobility object is an electronic bubble or a heavy ion. Perhaps the easiest way would be to conduct mobility measurements on positive ions in hydrogen. Positive ion clusters should have mobilities little different from negative ion clusters. Also, lifetime measurements would be valuable, but how to perform them is not clear. (References 36 and 37, on microwave relaxation measurements, and reference 11 represent the only work done in this area, as far as I know.) Measurements could be made all around the "horn" of the coexistence curve of helium-4 along a continuous path in the ρ, T plane to check that the low mobility object seen in gaseous helium is the same as that seen in liquid helium, thus providing further proof that we are seeing electronic bubbles in the gas (it being already well established that they exist in the liquid).[28,73,74] Recently Schwarz[75] has measured the mobilities of both the positive and negative species in helium-4 in the liquid, up to the critical point, moving along the saturated vapor pressure curve, and found nothing unusual, except very close to the critical point, an effect already observed in helium-3.[76,77] Although no differences are expected, it might be well to check that the data are the same in helium-3 as in helium-4 and the same in para-hydrogen and deuterium as in normal hydrogen. Finally, mixtures could be studied. The only study of this kind so far (mentioned in section 3.3) revealed an interesting and somewhat unexpected equation for the mobility. Helium-neon and helium-hydrogen mixtures are easily accessible and would possibly reveal the correctness of the percolation theory approach of Eggarter and Cohen.[64]

On the theoretical side, I have shown that a rounded well bubble model together with the square well bubble model give a pretty good fit to the data. However, computer calculations with a two-parameter potential, like the Saxon-Woods potential, as well as self-consistency calculations (discussed in subsection 4.1.4) should be performed, to confirm our indication that a sophisticated bubble model together with Young's experimental μ_0^{52} can fit the measured data completely. This would leave the explanation of Young's μ_0 to be accounted for by a scattering theory. Also, the reason why scattering theories have failed so far in their quantitative predictions needs to be uncovered.

For the interested reader, two abstracts for talks on this work were included in the 1971 New York Meeting issue of the Bulletin of the American Physical Society. A paper on our work in helium-4 should be published soon in Physics Letters, and another on our work in hydrogen should be published in Chemical Physics Letters.

APPENDIX I

INTENSITY DISTRIBUTION OF SOURCE ELECTRONS

The electron source was tritium embedded in titanium, forming titanium hydride. Without taking account of attenuation in the titanium hydride, the intensity distribution of emitted beta$^-$ particles (electrons) approximately follows the usual Kurie plot with a maximum of about 18 KeV:[78]

$$I_e = K P^2 (E_m - E_e)^2 \qquad \text{(I-1)}$$

where E_e=electron energy
E_m=maximum electron energy
P=electron momentum
I_e=differential intensity
(counts/time/energy interval)
K=constant for the species and its strength

(The main discrepancy of the actual spectrum for beta$^-$ decay from this formula is that in actuality there is a surplus of low-energy electrons.) Now we have the general relativistic relations

$$W^2 = P^2 + M^2 \qquad \text{and} \qquad W = M + T \qquad \text{(I-2)}$$

where W=total energy
M=rest energy
P=momentum
T=kinetic energy

Substituting these into the above,

$$I_e = K (W^2 - M^2) (T_m - T_e)^2 \qquad \text{(I-3)}$$

$$= K T_e (T_e + 2M) (T_m - T_e)^2 \qquad \text{(I-4)}$$

factor (T_e+2M) is virtually a constant since M=511 Kev and T≤18 KeV.

Now let us consider the effect of the gold layer. The published values for ranges and stopping powers for electrons in different substances[79] can be represented (in the case of gold at least, and over the energy range of interest) by

$$\ln S = \ln C_1 - C_2 \ln E \quad \text{or} \quad S = C_1 E^{-C_2} \tag{I-5}$$

The total stopping power (collision plus radiation) S is defined by the equation

$$-dE = S(E)\, \rho\, dx \tag{I-6}$$

Thus, going through a thick slab of metal,

$$\int_0^L dx = -\int_{E_i}^{E_f} \frac{dE}{S(E)\,\rho} \tag{I-7}$$

which yields

$$E_f = \left[E_i^{C_2+1} - L\rho\, C_1 (C_2+1) \right]^{-(C_2+1)} \tag{I-8}$$

C_1 and C_2 are determined by solving

$$S_1 = C_1 E_1^{-C_2} \quad \text{and} \quad S_2 = C_1 E_2^{-C_2} \tag{I-9}$$

which yield

$$C_2 = \frac{\ln(S_1/S_2)}{\ln(E_2/E_1)} \quad \text{and} \quad C_1 = S_1 E_1^{C_2} \tag{I-10}$$

Now to obtain the energy spectrum after passing through the gold from the initial energy spectrum, an E_f is calculated for each E_i from 0 to 18 KeV. The intensity at the initial E_i is the intensity at the final E_f. These two curves are shown in Figure 33. The maximum electron energy for the secondary spectrum is 14.8 KeV. The unrealistic low energy end of the secondary spectrum (not falling to zero) is not of great importance.

From the published values of range data in materials,[79] the number density of molecules required to stop the electrons emitted at the maximum energy (14.8 KeV) before they reach the first grid in the experimental cell (1.67 cm from source to the first grid) is $.450 \times 10^{20}$ cm^{-3} for helium-4 and $.375 \times 10^{20}$ cm^{-3} for hydrogen.

As to the absolute strength of the source, when it was purchased in 1961, it was rated at 1 curie/in^2=1.55 millicuries/mm^2. Our source is about 6 mm square, so the original activity (1961) was

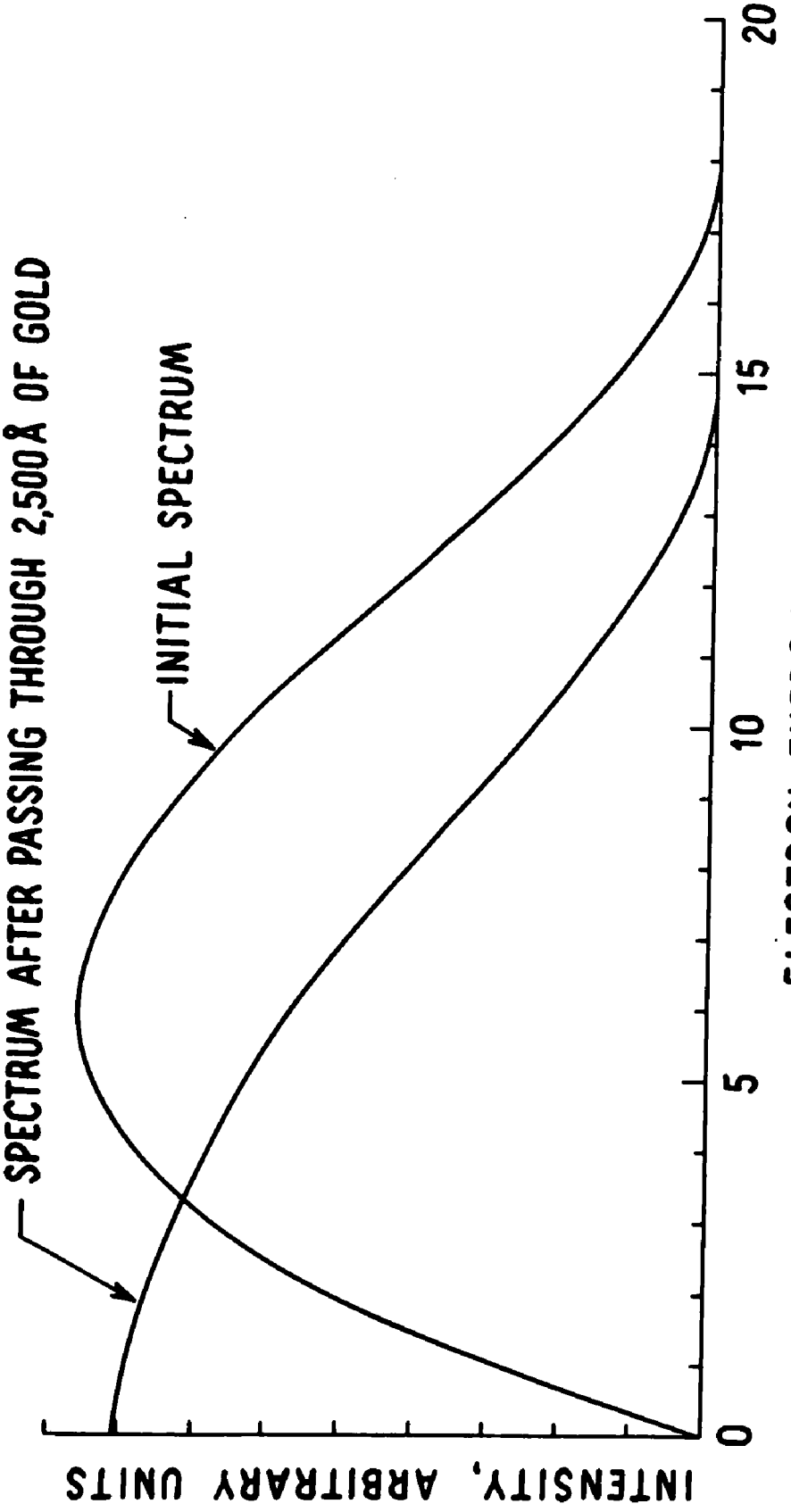

Fig. 33: Spectrum of beta particles emitted from tritium—original spectrum and spectrum after passing through 2,500Å of gold.

about 55.8 millicuries. The half-life of tritium is 12.26 years,[78] so the activity is now roughly 30 millicuries. The curie is defined as exactly 3.7×10^{10} disintegrations/second,[78] so the activity of the source at the present time can be expressed as roughly 10^9 disintegrations/second.

As to the deposition of the gold, it was done by myself in a home-made metals evaporator of standard design which I put back into working order. The gold was evaporated at pressures $\leq 1.5 \times 10^{-5}$ Torr. The thickness of the deposited metal was monitored with a Sloan DTM-3 Deposit Thickness Monitor.

Note that the gold ensures a good electrical connection from the source to the source biasing lead. The source was initially attached to a glass slide with Ablestik conducting copper epoxy.

APPENDIX II

CALIBRATION OF GERMANIUM RESISTANCE THERMOMETER

We decided to use a germanium thermometer rather than a carbon thermometer because: (i) a properly doped germanium thermometer is capable of measuring temperature accurately over a much greater range (up to 100K, say) than is a carbon thermometer, and (ii) a germanium thermometer gives very reproducible readings--it does not drift upon recyclying as does a carbon thermometer. However, a germanium thermometer has the disadvantage that its R versus T (or ln R versus ln T) characteristic is not always as "smooth" as the chacteristic of a carbon thermometer, and can in fact show definite "breaks."[80] Figure 34 is the final calibration curve for our thermometer, and a break in the curve is indeed evident. In spite of this, accurate polynomial fits of the form

$$\ln R = \sum_{i=0}^{n} A_i (\ln T)^i \qquad \text{(II-1)}$$

can be made. "For an optimum representation, it is necessary to make judicious choices both of the polynomial degree and the temperature range. Insistence on a single polynomial over the entire 1-100K range produces a solution with spurious oscillations of rms amplitude some 0.3% of the absolute temperature. Such spurious oscillations can be reduced to an amplitude of a few parts in 10^4 of temperature by using one polynomial for the 1-20K range and a second polynomial for T≥15K (thus affording a small overlap region between the two polynomials)."[80]

By vapor pressure thermometry, I calibrated my thermometer over the ranges 1.35-5.00K (liquid helium)[38], 11.0-15.0K (solid hydrogen)[25], 15.0-20.5K (liquid hydrogen)[25], and 63-77K (liquid

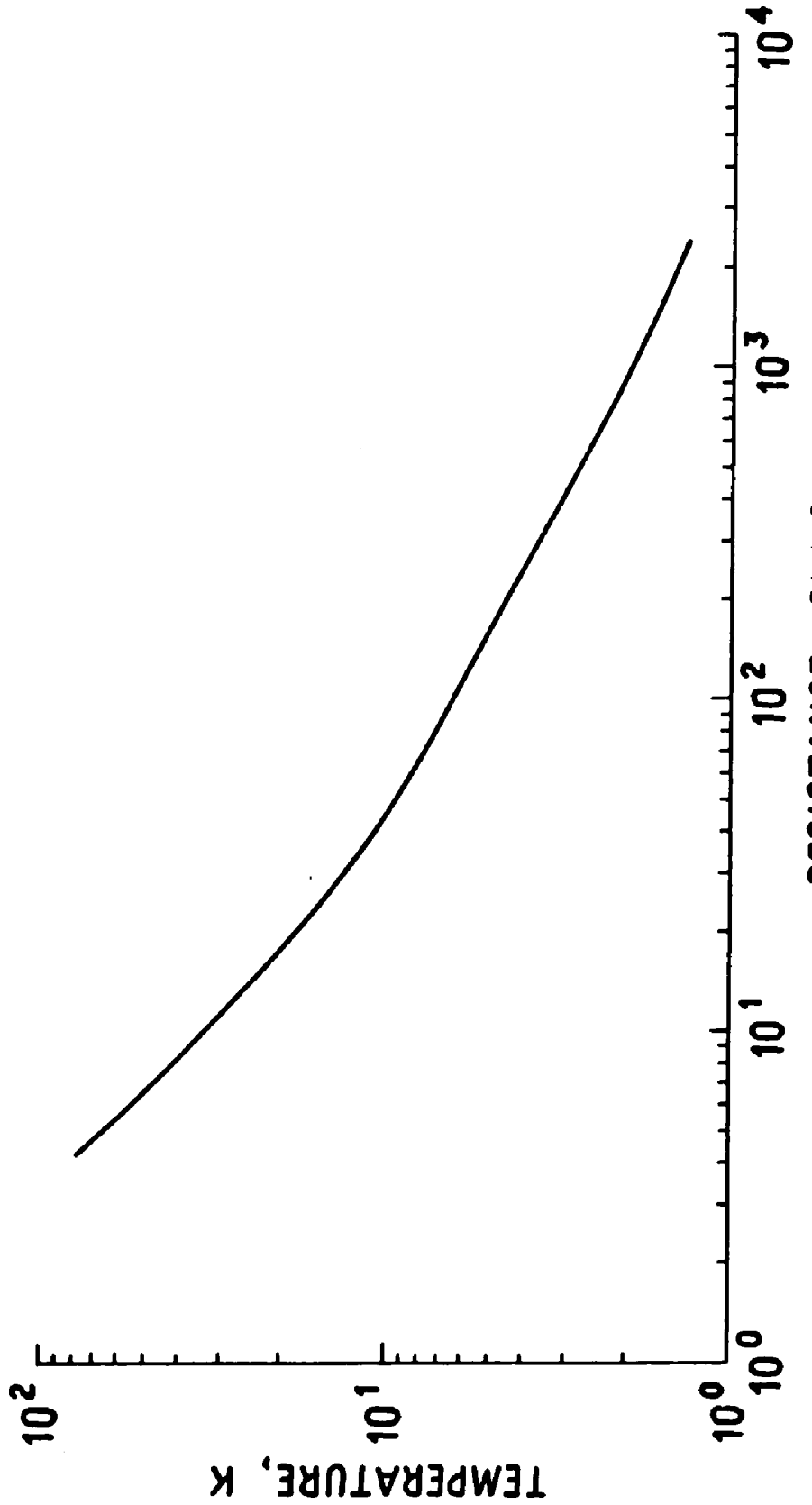

Fig. 34: Resistance-temperature calibration curve for the Cryocal germanium resistance thermometer used in this experiment.

nitrogen).[81] The measurements in liquid helium and liquid nitrogen were performed with the uncovered (except for its own case) thermometer immersed directly in the liquid. For the measurements in hydrogen, a special can was constructed, metal at the top (so it could be bolted together) but glass at the bottom. The thermometer rested near the bottom. The glass lower portion of the can allowed me to look in to see whether or not the hydrogen in the cell was liquid, and if it completely covered the thermometer. In the case of solid hydrogen, which crystallized on the walls something like ordinary ice, I could not be so sure. However, solidification was fairly sudden so that if the liquid level previously had been comparatively high, I felt safe in assuming the whole thermometer was encased in solid hydrogen. The hydrogen was initially liquefied by liquid helium in an arrangement similar to that described in subsection 2.3.2. There was a question as to whether thermal equilibrium was being achieved, so a great mass of fine copper wires (in the form of a "brush") was placed in the can to insure that the liquid hydrogen was all at one temperature.

At this point it was evident that there was a break in the R versus T characteristic between 5.0 and 11.0K. (The characteristic can break at different points and in different ways depending upon the doping of the germanium thermometer. Reference 80 has illustrations of this phenomenon for several thermometers.) So I then placed a carbon thermometer beside the germanium thermometer (now back inside the regular all metal can), cooled them and the can down below 5K, and allowed the system to slowly warm up (about two hours to go from 5 to 11K), measuring the resistance of both at many different temperatures. The measurements extended outside the 5-11K unknown region, on both

sides, so that it was possible to link-up with the previous calibration of the germanium thermometer, and thus to get a good calibration (for this cycle) for the carbon thermometer. The data for the carbon thermometer were fitted with the simple formula

$$[(\ln R)/T]^{1/2} = A \ln R + B \qquad \text{(II-2)}$$

That is, $[(\ln R)/T]^{1/2}$ versus ln R gave a straight line, the data outside the 5-11K range fixing the line. This then gave the R versus T characteristic for the germanium thermometer in the range 5-11K.

A computer fit of the final R versus T data was not attempted, past attempts on part of the data indicating that the fit over ranges where there were wide gaps in the data (here, 20.5-66K) being obviously incorrect just by inspection. Instead of that, a smooth curve was drawn in the gap 20.5-66K with a ship's curve, and this was felt to be accurate enough for our purposes. In the temperature ranges for which data were taken, the density of data points was almost great enough to draw a curve by itself. I think that the curve is accurate to at least 1% in temperature over its whole length, and is certainly more accurate over those ranges where calibration was performed.

In conclusion, while this method will give a reliable calibration, it is now seen to be easier, and in fact cheaper, to simply purchase a calibrated germanium thermometer, with a computer fitting of the data points, and with interpolation between points, rather than to do the calibration oneself.

APPENDIX III

HEAT BALANCE CALCULATIONS FOR TEMPERATURE CONTROL

The problem to be solved is that of heat conduction along a rod of uniform cross-section, but in which the temperature is different at each point along its length. This problem represents what is happening along the brass portion of the rod which is maintaining the temperature balance and control for the experimental can. We are neglecting gas heat exchange in what follows. Since this can be very important, any results obtained will be only approximately accurate--but that is enough to see if a proposed system is feasible or not. From reference 82 we have the usual heat conduction equation

$$\frac{\partial}{\partial t}\left(c\rho AT\right) = \frac{\partial}{\partial x}\left(KA\frac{\partial T}{\partial x}\right) \qquad \text{(III-1)}$$

where T=temperature
A=cross-sectional area
K(T)=thermal conductivity
ρ =mass density
c(T)=specific heat

In our case, we are interested in the steady-state solution, and additionally the cross-sectional area will be constant. Thus,

$$\frac{\partial}{\partial x}\left(K\frac{\partial T}{\partial x}\right)=0 \qquad \text{(III-2)}$$

Integrating,
$$K\frac{dT}{dx}=C \qquad \text{(III-3)}$$

If $K=aT^n$, then
$$T^n\frac{dT}{dx}=C_1 \qquad \text{(III-4)}$$

which if integrated yields

$$T(x)=\left[(n+1)\left(C_1x+C_2\right)\right]^{\frac{1}{n+1}} \qquad \text{(III-5)}$$

In fact, over the temperature range in which we are interested, $K=aT+bT^2$ very nearly.[83] In most cases this can be approximated with fair accuracy to just K=aT. Thus we have n=1 in our equation above, so

$$T(x) = [2(C_1 x + C_2)]^{1/2} \qquad \text{(III-6)}$$

The heat flow across any cross-section of the rod (in the steady-state solution) is

$$Q = KA\frac{dT}{dx} \qquad \text{(III-7)}$$

$$Q = (aT)^n(A)\left(\frac{C_1}{[(n+1)(C_1 x + C_2)]^{n/n+1}}\right) \qquad \text{(III-8)}$$

$$Q = aAC_1 \qquad \text{(III-9)}$$

For a rod of length L, with $T(x=0)=T_1$ and $T(x=L)=T_2$, we solve

$$T = [2(C_1 x + C_2)]^{1/2} \qquad \text{(III-10)}$$

to yield

$$C_1 = \frac{T_2^2 - T_1^2}{2L} \qquad \text{(III-11)}$$

So altogether,

$$Q = \frac{aA}{2L}(T_2^2 - T_1^2) \qquad \text{(III-12)}$$

From a knowledge of the constant a from reference 83 plus reasonable engineering choices for Q, T_1, and T_2, the needed ratio A/L may be calculated in the design of the rod to be used.

APPENDIX IV

DERIVATION OF STARTING EQUATION FOR THE EVALUATION OF ΔF

The ideas behind this Appendix (setting up the general equation for ΔF) are covered in reference 84.

We want to evaluate the Helmholtz free energy

$$\Delta F = F_g + F_e + V_{e-g} \tag{IV-1}$$

where F_g=free energy for the gas alone
F_e=free energy for the electron alone
V_{e-g}=electron-gas interaction energy

We have always

$$F = G - PV \tag{IV-2}$$

where F=Helmholtz free energy
G=Gibbs free energy

or, writing these functions per unit volume (indicated by small letters)

$$f = g - p \tag{IV-3}$$

We can write g as

$$g(r) = \mu \rho(r) \tag{IV-4}$$

where μ=chemical potential
$\rho(r)$=number density

Therefore we can write

$$F_{gas} = \int d^3r \{\mu\rho(r) - p(r)\} \tag{IV-5}$$

In the end, of course, we will want ΔF, so using the subscript ∞ to designate the uncorrelated (free) state (far from our potential well)

$$\Delta F_{gas} = F_{gas} - F_{\infty\,gas} = \int d^3r \{[\mu(r)\rho(r) - \mu_\infty \rho_\infty] - [p(r) - p_\infty]\} \tag{IV-6}$$

$$= \int d^3r \{[\mu(r) - \mu_\infty]\rho(r) - [p(r) - p_\infty]\} \tag{IV-7}$$

since μ_∞ is a constant and both ρ_∞ and $\rho(r)$ integrate to the total number of atoms N. We have the general expression for μ[56]

$$\mu = kT \ln \rho(r) + B_1(T)\rho(r) + \chi(T) + U(r) \tag{IV-8}$$

So $$\mu(r)-\mu_\infty = kT \ln\left[\frac{\rho(r)}{\rho_\infty}\right] + B_1\left[\rho(r)-\rho_\infty\right] \qquad \text{(IV-9)}$$

and the equation of state is

$$P = \rho kT\left(1+B_1\rho\right) \qquad \text{(IV-10)}$$

Combining the last two equations,

$$\mu(r)-\mu_\infty = kT \ln \frac{\rho(r)\left[1+B_1\rho(r)\right]}{\rho_\infty\left[1+B_1\rho_\infty\right]} + B_1 kT\left\{\rho(r)\left[1+B_1\rho(r)\right]-\rho_\infty\left[1+B_1\rho_\infty\right]\right\} \qquad \text{(IV-11)}$$

$$= kT\left\{\ln\left(\frac{\rho}{\rho_\infty}\right)+\ln\left(\frac{1+B_1\rho}{1+B_1\rho_\infty}\right)+B_1(\rho-\rho_\infty)+B_1^2(\rho^2-\rho_\infty^2)\right\} \qquad \text{(IV-12)}$$

where we let $\rho(r)=\rho$ from now on if there is no subscript.

Also we have

$$\rho(r)-\rho_\infty = kT\left\{\rho+B_1\rho^2-\rho_\infty-B_1\rho_\infty^2\right\} \qquad \text{(IV-13)}$$

$$= kT\left\{(\rho-\rho_\infty)+B_1(\rho^2-\rho_\infty^2)\right\} \qquad \text{(IV-14)}$$

Adding these two terms,

$$\rho(r)\left[\mu(r)-\mu_\infty\right]-\left[\rho(r)-\rho_\infty\right] = kT\left[\begin{array}{l}\rho\ln\left(\frac{\rho}{\rho_\infty}\right)+\rho\ln\left(\frac{1+B_1\rho}{1+B_1\rho_\infty}\right)+B_1\rho(\rho-\rho_\infty)\\ +B_1^2\rho(\rho^2-\rho_\infty^2)-(\rho-\rho_\infty)-B_1(\rho^2-\rho_\infty^2)\end{array}\right] \qquad \text{(IV-15)}$$

Combining (IV-7) and (IV-15),

$$\Delta F_{gas} = kT\rho_\infty\int d^3r\left\{\frac{\rho}{\rho_\infty}\ln\left(\frac{\rho}{\rho_\infty}\right)+\frac{\rho}{\rho_\infty}\ln\left(\frac{1+B_1\rho}{1+B_1\rho_\infty}\right)+\left(1-\frac{\rho}{\rho_\infty}\right)\left(1+B_1\rho_\infty\right)+B_1^2\frac{\rho}{\rho_\infty}\left(\rho^2-\rho_\infty^2\right)\right\} \qquad \text{(IV-16)}$$

Now $$\ln\left(\frac{1+B_1\rho}{1+B_1\rho_\infty}\right) = \ln\left(1+B_1\rho\right)-\ln\left(1+B_1\rho_\infty\right) \qquad \text{(IV-17)}$$

We may exnand according to the series

$$\ln(1+X) = X-\frac{X^2}{2}+\frac{X^3}{3}-\frac{X^4}{4}+-\cdots \qquad (-1\le X\le+1) \qquad \text{(IV-18)}$$

So $$\ln\left(\frac{1+B_1\rho}{1+B_1\rho_\infty}\right) \simeq B_1(\rho-\rho_\infty)-\frac{B_1^2}{2}\left(\rho^2-\rho_\infty^2\right) \qquad \text{(IV-19)}$$

Combining (IV-16) and (IV-19),

$$\frac{\Delta F_{gas}}{kT} = \rho_\infty\int d^3r\left\{\frac{\rho}{\rho_\infty}\ln\left(\frac{\rho}{\rho_\infty}\right)+\left(1-\frac{\rho}{\rho_\infty}\right)+B_1\rho_\infty\left(1-\frac{\rho}{\rho_\infty}\right)^2-\frac{\rho}{\rho_\infty}\frac{B_1^2}{2}\left(\rho_\infty^2-\rho^2\right)\right\} \qquad \text{(IV-20)}$$

The term going as B_1^2 is a scond-order correction.

Note that (IV-20) reduces to the simple PV term for F_{gas} for the square well case.

APPENDIX V

EVALUATION OF ΔF FOR THE POTENTIAL $U=-U_o/\cosh^2(r/r_o)$

We have from equation (IV-19) of Appendix IV the expression for ΔF_{gas}. Adding on the electronic energy, and not including the second-order correction (second order in B_1), we have

$$\frac{\Delta F}{kT} = \frac{\langle T+V\rangle}{kT} + \rho_\infty \int d^3r \left\{ \frac{\rho}{\rho_\infty} \ln\left(\frac{\rho}{\rho_\infty}\right) + \left(1-\frac{\rho}{\rho_\infty}\right) + B_1 \rho_\infty \left(1-\frac{\rho}{\rho_\infty}\right)^2 \right\} \quad (V-1)$$

Now the potential we are interested in, $U=-U_o/\cosh^2(r/r_o)$, is discussed in reference 85. However, it is done for the one-dimensional case whereas we want the three-dimensional case. The radial equation for the three-dimensional case, after the separation of variables is

$$\frac{1}{r^2}\frac{d}{dr}\left(r^2\frac{d\psi_r}{dr}\right) + \frac{2m}{\hbar^2}\left[E + \frac{U_o}{\cosh^2(r/r_o)} - \frac{\hbar^2 \ell(\ell+1)}{2mr^2}\right]\psi_r = 0 \quad (V-2)$$

We are interested in the s-wave case, for which $\ell=0$. Making the substitution $\psi_r = R/r$, after a little algebra we find

$$\frac{d^2R}{dr^2} + \frac{2m}{\hbar^2}\left[E + \frac{U_o}{\cosh^2(r/r_o)}\right]R = 0 \quad (V-3)$$

which is the same as the one-dimensional starting equation. Thus, the eigenvalues will be the same as for the one-dimensional case, and the eigenfunctions will also be the same after being multiplied by $1/r$.

The lowest energy level in the one-dimensional case is forbidden in the three-dimensional case because the wave function goes as $1/r$ near the origin. For a finite potential, the wave function must not only be square integrable--it must be finite everywhere also.[85] So the first allowed level is actually the second one in the one-dimensional case. The energy is

$$\langle T+V\rangle = -\frac{\hbar^2}{8mr_o^2}\left[-3+\left(1+\frac{8mU_or_o^2}{\hbar^2}\right)^{1/2}\right]^2 \quad (V-4)$$

(Note that this level is incorrectly stated as being forbidden in reference 85, but is given correctly in the companion book of problems, reference 86.)

Now we assume the density follows the shape of the potential exactly, so we put

$$g(r) \equiv \frac{\rho}{\rho_\infty} = 1 - \frac{1}{\cosh^2(r/r_0)} \qquad \text{(V-5)}$$

Combining (V-1), (V-4), and (V-5) we obtain

$$\frac{\Delta F}{kT} = -\frac{\hbar^2}{8mr_0^2}\left[-3+\left(1+\frac{8mV_2r_0^2}{\hbar^2}\right)^{1/2}\right]^2 + \rho_\infty \int d^3r \left\{(1-g) + B_1\rho_\infty (1-g)^2 + g\ln g\right\} \qquad \text{(V-6)}$$

Let us first evaluate the most difficult term, the gln(g) term.

$$g(r) = 1 - \frac{1}{\cosh^2(r/r_0)} = \tanh^2(r/r_0) \qquad \text{(V-7)}$$

So we have

$$\int d^3r\, g\ln g = 4\pi \int_0^\infty r^2 dr \tanh^2(r/r_0) \ln\{\tanh^2(r/r_0)\} \qquad \text{(V-8)}$$

$$= 4\pi r_0^3 \int_0^\infty x^2 \tanh^2 x \ln\{1-\operatorname{sech}^2 x\}\, dx \qquad \text{(V-9)}$$

Now, as in (IV-17),

$$\ln(1+x) = x - \frac{x^2}{2} + \frac{x^3}{3} - \frac{x^4}{4} + \cdots = \sum_{n=1}^{\infty} \frac{(-1)^{n+1}}{n} x^n \qquad \text{(V-10)}$$

So $$\int d^3r\, g\ln g = -4\pi r_0^3 \sum_{n=1}^{\infty} \frac{1}{n} \int_0^\infty x^2 \tanh^2 x \operatorname{sech}^{2n} x\, dx \qquad \text{(V-11)}$$

$$= -4\pi r_0^3 \sum_{n=1}^{\infty} \frac{1}{n} \int_0^\infty x^2 \left[\operatorname{sech}^{2n} x - \operatorname{sech}^{2n+2} x\right] dx \qquad \text{(V-12)}$$

(Notice we have interchanged the summation and integration in arriving at (V-11)--hopefully no problems will result from this.) We must evaluate integrals of the type

$$I_{2n} = \frac{1}{2}\int_{-\infty}^{+\infty} \frac{x^2\, dx}{\cosh^{2n} x} \qquad \text{(V-13)}$$

$$= -\frac{1}{2}\frac{d^2}{d\alpha^2}\left\{\int_{-\infty}^{+\infty} \frac{e^{i\alpha x}}{\cosh^{2n} x}\, dx\right\}\Bigg|_{\alpha=0} \qquad \text{(V-14)}$$

We shall use the following contour to evaluate this integral:

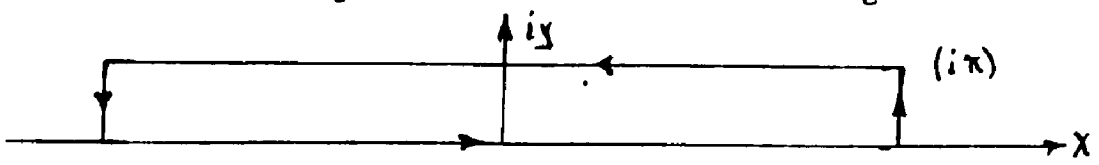

$$\oint = \int_{-\infty}^{+\infty} \frac{e^{i\alpha x}}{\cosh^{2n} x}\, dx - \int_{-\infty}^{+\infty} \frac{e^{i\alpha (i\pi + x)}}{\cosh^{2n} (i\pi + x)}\, dx \qquad \text{(V-15)}$$

The contribution to the contour integral from the "ends" clearly goes to zero. Now we have the identity

$$\cosh (x + i\pi) = -\cosh x \qquad \text{(V-16)}$$

So $$\oint = \int_{-\infty}^{+\infty} \frac{e^{i\alpha x}}{\cosh^{2n} x}\, dx - e^{-\pi\alpha} \int_{-\infty}^{+\infty} \frac{e^{i\alpha x}}{\cosh^{2n} x}\, dx \qquad \text{(V-17)}$$

Thus, $$I_{2n} = -\frac{1}{2} \frac{d^2}{d\alpha^2} \left\{ \frac{1}{1 - e^{-\pi\alpha}} \oint \frac{e^{i\alpha x}}{\cosh^{2n} x}\, dx \right\} \Big|_{\alpha = 0} \qquad \text{(V-18)}$$

The only pole of cosh(z)=0 within the contour is at $z = i\pi/2$. Let

$$w = e^{2x} \qquad \text{(V-19)}$$

After a little algebra,

$$I_{2n} = -2^{2(n-1)} \frac{d^2}{d\alpha^2} \left\{ \frac{1}{1 - e^{-\pi\alpha}} \oint \frac{w^{n + \frac{i\alpha}{2} - 1}}{(w+1)^{2n}}\, dw \right\} \Big|_{\alpha = 0} \qquad \text{(V-20)}$$

Evaluating the contour integral,

$$\oint \frac{w^{n + \frac{i\alpha}{2} - 1}}{(w+1)^{2n}}\, dw = \frac{2\pi i}{(2n-1)!} \left\{ \frac{d^{2n-1}}{dw^{2n-1}} \left(w^{n + \frac{i\alpha}{2} - 1} \right) \right\} \Big|_{w = 1} \qquad \text{(V-21)}$$

$$= \frac{2\pi i}{(2n-1)!} \left(\frac{i\alpha}{2} + n - 1 \right) \left(\frac{i\alpha}{2} + n - 2 \right) \cdots \left(\frac{i\alpha}{2} - (n-1) \right) (-1)^{\frac{i\alpha}{2} - n} \qquad \text{(V-22)}$$

$$= \frac{2\pi i}{(2n-1)!} (-1)^{n-1} \frac{i\alpha}{2} \prod_{j=1}^{n-1} \left[\left(\frac{\alpha}{2} \right)^2 + j^2 \right] \qquad \text{(V-23)}$$

Putting (V-23) back into (V-20) yields

$$I_{2n} = -\frac{2^{2(n-1)} \pi}{(2n-1)!} \frac{d^2}{d\alpha^2} \left\{ \frac{\alpha}{e^{\frac{\pi\alpha}{2}} - e^{-\frac{\pi\alpha}{2}}} \prod_{j=1}^{n-1} \left[\left(\frac{\alpha}{2} \right)^2 + j^2 \right] \right\} \Big|_{\alpha = 0} \qquad \text{(V-24)}$$

$$= -\frac{2^{2(n-2)}}{(2n-1)!} \pi^2 \frac{d^2}{dx^2} \left\{ \frac{x}{\sinh x} \frac{1}{\pi^{2(n-1)}} \prod_{j=1}^{n-1} \left[x^2 + (\pi j)^2 \right] \right\} \Big|_{x = 0} \qquad \text{(V-25)}$$

$$\left(x = \frac{\alpha\pi}{2} \right)$$

$$= \frac{2^{2n-3} \pi^2 [(n-1)!]^2}{(2n-1)!} \left\{ \frac{1}{6} - \frac{1}{\pi^2} \sum_{j=1}^{n-1} \frac{1}{j^2} \right\} \qquad \text{(V-26)}$$

Returning to (V-13) and (V-14), we find

$$\int d^3r\, g \ln g = -4\pi r_0^3 \sum_{n=1}^{\infty} \frac{1}{n} (I_{2n} - I_{2n+2}) \qquad \text{(V-27)}$$

Combining the last two equations,

$$\int d^3r\, g\ln g = -4\pi^3 r_0^3 \sum_{n=1}^{\infty} \frac{1}{n} \left[\begin{array}{l} \dfrac{2^{2n-3}[(n-1)!]^2}{(2n-1)!} \left\{ \frac{1}{6} - \frac{1}{\pi^2} \sum_{j=1}^{n-1} \frac{1}{j^2} \right\} \\ - \dfrac{2^{2n-1}[n!]^2}{(2n+1)!} \left\{ \frac{1}{6} - \frac{1}{\pi^2} \sum_{j=1}^{n} \frac{1}{j^2} \right\} \end{array} \right] \qquad \text{(V-28)}$$

Combining the two series,

$$\int d^3r\, g\ln g = -4\pi^3 r_0^3 \left[\frac{1}{\pi^2} \int_0^{\infty} \frac{x^2 dx}{\cosh^2 x} - \sum_{n=1}^{\infty} \frac{2^{2n-1}[n!]^2}{n(n+1)(2n+1)!} \left\{ \frac{1}{6} - \frac{1}{\pi^2} \sum_{j=1}^{n} \frac{1}{j^2} \right\} \right] \qquad \text{(V-29)}$$

Returning to (V-7)

$$\frac{\Delta F}{kT} = \frac{\langle T+V \rangle}{kT} + 4\pi^3 r_0^3 \rho_\infty \left[\begin{array}{l} -\frac{1}{\pi^2} \int_0^{\infty} \frac{x^2 dx}{\cosh^2 x} + \sum_{n=1}^{\infty} \frac{2^{2n-1}[n!]^2}{n(n+1)(2n+1)!} \left\{ \frac{1}{6} - \frac{1}{\pi^2} \sum_{j=1}^{n} \frac{1}{j^2} \right\} \\ + \frac{1}{\pi^2} \int_0^{\infty} \frac{x^2 dx}{\cosh^2 x} + \frac{B_1 \rho_\infty}{\pi^2} \int_0^{\infty} \frac{x^2 dx}{\cosh^4 x} \end{array} \right] \qquad \text{(V-30)}$$

Using reference 87 we find

$$\int_0^{\infty} \frac{x^2 dx}{\cosh^4 x} = \frac{\pi^2}{18} - \frac{1}{3} \qquad \text{(V-31)}$$

So together

$$\frac{\Delta F}{kT} = -\frac{h^2}{8m r_0^2 kT} \left[-3 + \left(\frac{8m r_0^2 V_0}{h^2} \right)^{1/2} \right]^2 + \frac{\pi^3 \rho_\infty r_0^3}{3} \left[\begin{array}{l} B_1 \rho_\infty \left(\frac{2}{3} - \frac{4}{\pi^2} \right) \\ + \sum_{n=1}^{\infty} \frac{2^{2n}[n!]^2}{n(n+1)(2n+1)!} \left\{ 1 - \frac{6}{\pi^2} \sum_{j=1}^{n} \frac{1}{j^2} \right\} \end{array} \right] \qquad \text{(V-32)}$$

Defining the dimensionless quantity

$$z = \frac{8m V_0 r_0^2}{h^2} \qquad \text{(V-33)}$$

and adding up the first 12 terms in the series results in

$$\frac{\Delta F}{kT} = -\frac{V_0}{zkT} \left[-3 + (1+z)^{1/2} \right]^2 + \frac{\pi^3 \rho_\infty r_0^3}{3} \left[.1647 + .26138\, B_1 \rho_\infty \right] \qquad \text{(V-34)}$$

What error results from cutting off the series after a certain number of terms? We estimate this as follows:

From reference 88

$$\sum_{k=1}^{\infty} \frac{1}{k^2} = \frac{\pi^2}{6} \qquad \text{(V-35)}$$

So

$$1 - \frac{6}{\pi^2} \sum_{j=1}^{n} \frac{1}{j^2} = \frac{6}{\pi^2} \sum_{j=n+1}^{\infty} \frac{1}{j^2} \qquad \text{(V-36)}$$

$$\leq \frac{6}{\pi^2} \int_{n+1}^{\infty} \frac{dj}{j^2}$$

$$\leq \frac{6}{\pi^2 n} \qquad \text{(V-37)}$$

Using Stirling's approximation,

$$n! \simeq (2\pi n)^{1/2} \left(\frac{n}{e}\right)^n \tag{V-38}$$

$$\frac{2^{2n}[n!]^2}{n(n+1)(2n+1)!} \simeq \frac{\pi^{1/2}}{2n^{5/2}} \tag{V-39}$$

Thus we have approximately

$$\int_n^\infty \frac{6}{\pi^2 n} \frac{\pi^{1/2}}{2n^{5/2}} dn = \frac{6}{5\pi^{3/2}} \frac{1}{n^{5/2}} \tag{V-40}$$

For n=12, this is roughly 5×10^{-4}, which is small compared to 1, so it is a good approximation.

Now to return to the problem, we must find the minimum ΔF in (V-34). Differentiating with respect to r_o, and setting the derivative equal to zero yields the following after some algebra:

$$q(z) = \Delta F(z)/U_o \tag{V-41}$$

$$= -\frac{\left[(1+z) - 3\sqrt{1+z}\right]\left[(1+z) + \sqrt{1+z} + \frac{2}{3}\right]}{z\,(1+z)} \tag{V-42}$$

and z (given by (V-33)) is determined from

$$f(z) = \left(\frac{2m}{\hbar^2}\right)\left(\frac{\pi^3}{16}\right)\left[.1647 + .26138\, B_1 \rho_\infty\right] kT \frac{\rho_\infty}{k_o^5} \tag{V-43}$$

$$= \frac{1}{z^{5/2}} \left[\sqrt{1+z} - 3\right]^2 \left[\frac{3\sqrt{1+z} - 1}{(1+z) - 3\sqrt{1+z}}\right] \tag{V-44}$$

$$\left(k_o = \frac{2m}{\hbar^2} U_o^{1/2}\right)$$

Thanks are due to L.M. Sander who worked out all of Appendix IV and the bulk of Appendix V.

APPENDIX VI

SELF-CONSISTENCY CALCULATION FOR THE ROUNDED WELL BUBBLE MODEL

First I will show that the potential from the optical model as given in (4-38) is essentially the same as that obtained from the Wigner-Seitz model, (4-7):

$$V_o = \frac{\hbar^2 k_o^2}{2m} \tag{VI-1}$$

Now k_o is given by (4-8),

$$\tan k_o(r_s - a) = k_o r_s \tag{VI-2}$$

Using the expansion of the tangent function

$$\tan x = x + \frac{x^3}{3} + \frac{2x^5}{15} + \cdots \qquad x^2 < \frac{\pi^2}{4} \tag{VI-3}$$

we have

$$k_o r_s - k_o a + \frac{k_o^3 (r_s - a)^3}{3} \simeq k_o r_s \tag{V-4}$$

This reduces to

$$k_o^2 \simeq \frac{3a}{r_s^3}\left[1 + \frac{3a}{r_s}\right] \tag{VI-5}$$

Using (4-1) for r_s

$$r_s = \left(\frac{3}{4\pi\rho_o}\right)^{1/3} \tag{VI-6}$$

we find

$$V_o = \frac{\hbar^2 k_o^2}{2m} = \left(\frac{\hbar^2}{2m}\right) 4\pi a \rho_o \left[1 + \frac{3a}{r_s}\right] \tag{VI-7}$$

This is the same as the optical model except for the correction factor $\left[1 + \frac{3a}{r_s}\right]$. This factor is as large as 1.455 at a density of 35×10^{20} cm^{-3}.

Now we must evaluate the actual wave function for the rounded well bubble model to be used in (4-43). The wave functions for the one-dimensional case are given in reference 84. For the three-dimensional case, all even wave functions (that is, those symmetric about the origin) are forbidden because we introduce a 1/r factor into the wave functions, and still require them to be finite everywhere, as pointed out in

Appendix V. The odd wave function lowest in energy is

$$\psi(r) = \frac{C}{(r/r_0)\cosh^s(r/r_0)}\, W_2 \qquad \text{(VI-8)}$$

where C=normalization constant

$s = \frac{1}{2}\left[-1+\left(1+\frac{8mr_0^2V_0}{\hbar^2}\right)^{1/2}\right]$

$W_2 = \sinh(r/r_0)\, F\left(-\tfrac{1}{2}s+\tfrac{1}{2}\epsilon+\tfrac{1}{2}, -\tfrac{1}{2}s-\tfrac{1}{2}\epsilon+\tfrac{1}{2}, \tfrac{3}{2}, -\sinh(r/r_0)\right)$

F=hypergeometric function

$\epsilon = \sqrt{-2mEr_0^2/\hbar^2}$

with the condition $-\frac{1}{2}s+\frac{1}{2}\epsilon+\frac{1}{2} = -n \qquad (n=0,1,2\ldots)$ (VI-9)

The hypergeometric series is defined in reference 89 as

$$F(\alpha,\beta;\gamma;z) = 1+\frac{\alpha\cdot\beta}{\gamma\cdot 1}z+\frac{\alpha(\alpha+1)\beta(\beta+1)}{\gamma(\gamma+1)\cdot 1\cdot 2}z^2+\frac{\alpha(\alpha+1)(\alpha+2)\beta(\beta+1)(\beta+2)}{\gamma(\gamma+1)(\gamma+2)\cdot 1\cdot 2\cdot 3}z^3+\cdots \qquad \text{(VI-10)}$$

In our case (m=0),

$$F\left(0, -s+1, \tfrac{3}{2}, -\sinh(r/r_0)\right) = 1 \qquad \text{(VI-11)}$$

The series breaks off immediately. (For the next level, the z term would be included; for the third level, the z^2 term; and so one.)

So our wave function is

$$\psi(r) = C\,\frac{\sinh(r/r_0)}{(r/r_0)\cosh^s(r/r_0)} \qquad \text{(VI-12)}$$

C is determined by the usual condition

$$\int_0^\infty d^3r\ |\psi(r)|^2 = 1 \qquad \text{(VI-13)}$$

Now s>1 because of (VI-9), s=1+ϵ, and the fact that $\epsilon>0$. So we evaluate (VI-13) using reference 90 to yield

$$\psi(r) = \left[4^{s-1}\pi r_0^3\left\{B(s-1,s-1)-4B(s,s)\right\}\right]^{-1/2}\frac{\sinh(r/r_0)}{(r/r_0)\cosh^s(r/r_0)} \qquad \text{(VI-14)}$$

where the beta function is defined in terms of the more customary gamma function by reference 91 as

$$B(x,y) = \frac{\Gamma(x)\,\Gamma(y)}{\Gamma(x+y)} \qquad \text{(VI-15)}$$

APPENDIX VII

CALCULATION OF YOUNG'S μ_o FROM SCATTERING THEORY

The electron wave function in a homogenous medium has a translational part represented by a complex wave vector $\underline{k}$ given by

$$k^2 = k_o^2 - 4\pi\rho a + i\,4\pi a^2 \rho k_o \qquad \text{(VII-1)}$$

The electron has an energy

$$E = \frac{\hbar^2 k_o^2}{2m^*} = \frac{\hbar^2}{2m^*}\left(k^2 + 4\pi\rho a - i\,4\pi a^2\rho k_o\right) \qquad \text{(VII-2)}$$

The translational part of the wave function is then

$$\psi_{translational} = \exp i\left(\frac{Et}{\hbar} + \underline{k}\cdot\underline{r}\right) \qquad \text{(VII-3)}$$

Rearranging this and assuming $\rho a^3 \ll 1$, Legler[40] finds a relaxation time

$$\tau^{-1} = 4\pi a^2 \rho \hbar \left(k^2 + 4\pi\rho a\right)^{1/2}/m \qquad \text{(VII-4)}$$

and the real part of the energy

$$E_{real} = \hbar^2\left(k^2 + 4\pi\rho a\right)/2m \qquad \text{(VII-5)}$$

Rewriting a little, we recognize these as

$$\tau = \lambda/\left(v^2 + \frac{\hbar^2}{m^2}4\pi\rho a\right)^{1/2} = \frac{\lambda}{\left(v^2 + \frac{2V_o}{m}\right)^{1/2}} \qquad \text{(VII-6)}$$

where $v = \hbar k/m$

V_o = optical potential

In the usual case $\tau = \lambda/v$, so what we are saying is that in the dense medium, the electron has a ground state energy V_o, in which state it undergoes many collisions; it has also some thermal energy represented by k and its actual velocity is $\hbar k_o/m$. I found it more convenient to write

$$\tau = \lambda\left(v^2 + \frac{\hbar^2}{m^{*2}\lambda}\right)^{1/2} \qquad \text{(VII-7)}$$

The first approximation to the Boltzmann equation with a distribution function f is

$$\frac{e\mathcal{E}}{m}\frac{\partial f}{\partial v_x} = \frac{f^{(o)} - f}{\tau(v)} \qquad \text{(VII-8)}$$

where $f^{(o)}$ = unperturbed distribution function

We expand f in powers of $\mathcal{E}$ -

$$f = f^{(0)} + \mathcal{E} f^{(1)} + \mathcal{E}^2 f^{(2)} + \mathcal{E}^3 f^{(3)} + \cdots \qquad \text{(VII-9)}$$

then equate powers of $\mathcal{E}$, leading to

$$f^{(1)} = -\frac{e\tau}{m}\frac{\partial f^{(0)}}{\partial v_x}\ ;\quad f^{(2)} = \frac{e^2\tau^2}{m^2}\frac{\partial^2 f^{(1)}}{\partial v_x^2}\ ;\quad f^{(3)} = -\left(\frac{e\tau}{m}\right)^3\frac{\partial^3 f^{(0)}}{\partial v_x^3} \qquad \text{(VII-10)}$$

$f^{(3)}$ is the term that gives the field dependence. Then we have

$$\langle v_d \rangle = \frac{\int_0^\infty v_x f\, d^3v}{\int_0^\infty f\, d^3v} \qquad \text{(VII-11)}$$

with (to first order)

$$f = f^{(0)} - \frac{e\mathcal{E}\tau}{m}\frac{\partial f^{(0)}}{\partial v_x} \qquad \text{(VII-12)}$$

and $$f^{(0)} = A e^{-\frac{1}{2}m\beta(v_x^2+v_y^2+v_z^2)} \qquad \left(\beta = \frac{1}{k_B T}\right) \qquad \text{(VII-13)}$$

Performing the angular integration leads to

$$\mu = \frac{\langle v_d \rangle}{\mathcal{E}} = \frac{\frac{1}{3}\beta e\lambda \int_0^\infty dv\ v^4\left(v^2 + \frac{\hbar^2}{m^2 a\lambda}\right)^{-1/2} e^{-\frac{1}{2}m\beta v^2}}{\int_0^\infty dv\ v^2 e^{-\frac{1}{2}m\beta v^2}} \qquad \text{(VII-14)}$$

Now make the substitution

$$v^2 = \left(\frac{\hbar^2}{m^2 a\lambda}\right)t\ ;\quad \gamma = \frac{\hbar^2}{2m}\frac{\beta}{a\lambda} = \frac{\hbar^2}{2m}(4\pi a\rho)/kT = \frac{V_0}{kT} \qquad \text{(VII-15)}$$

and do the integral in the denominator. This process yields

$$\mu = \mu^{(0)}\left(\frac{V_0}{kT}\right)^2 \Gamma(5/2)\, U(5/2, 3, \gamma) \qquad \text{(VII-16)}$$

where $$\mu^{(0)} = \frac{4}{3\sqrt{2\pi}} e \left(\frac{\beta}{m}\right)^{1/2}\lambda \qquad \text{(VII-17)}$$

the "classical" result and

$$\Gamma(5/2)\, U(5/2, 3, \gamma) = \int_0^\infty dt\ t^{3/2}(t+1)^{-1/2} e^{-\gamma t} \qquad \text{(VII-18)}$$

(This last is Legler's equation (7).) This is a Kummer function. This final expression has the correct limit for $V_0/kT \to 0$, but I can not find any analytic function to bridge the gap between the low and high values of V_0/kT. For $V_0/kT \to \infty$

$$U(5/2, 3, \gamma) = \left(\frac{V_0}{kT}\right)^{-5/2}\left\{\sum_{n=0}^{R}\frac{[a(a+1)(a+2)\cdots(a+n-1)]\{(1+a-b)\cdots(1+a-b+n-1)\}}{n!\,(-V_0/kT)^n} + O[(-V_0/kT)^R]\right\} \qquad \text{(VII-19)}$$

If we just take the first term of this series, we obtain

$$\mu = \mu^{(0)}\ \frac{3\sqrt{\pi}}{4}\left(\frac{V_0}{kT}\right)^{-1/2} \qquad \text{(VII-20)}$$

i.e., no temperature dependence.

Including the second term gives

$$\mu = \mu^{(0)} \frac{3\sqrt{\pi}}{4} \left(\frac{V_0}{kT}\right)^{-1/2} \left[1 - \frac{5}{4} \left(\frac{V_0}{kT}\right)^{-1/2}\right] \qquad \text{(VII-21)}$$

which means that at fixed ρ, an increase in T decreases μ. But this expansion is unfortunately only really useful for $V_0/kT > 10$, if then, because terms alternate in sign.

This result means roughly

$$\mu \propto \mu^{(0)} \left(\frac{kT}{V_0}\right)^{1/2} \qquad \text{(VII-22)}$$

We work with (roughly) $kT/V_0 \approx 1/200$, so this expression depresses μ by roughly an order of magnitude, which is probably what we need. Actually, there are severe convergence problems. To get the field dependence one has to write f out up to terms in $f^{(3)}$.

If we make the substitution x=qt, we may rewrite equations (VII-15), (VII-16), and (VII-18) as

$$\mu = \mu^{(0)} \int_0^\infty x^{3/2} (x+\beta)^{-1/2} e^{-x} dx \qquad \text{(VII-23)}$$

This function was integrated on a computer, and the results are shown in Figure 35. Also shown in this figure are arbitrarily selected data points from Grünberg[30] and myself from both helium-4 and hydrogen data. In selecting my helium data points, I never went to densities higher than those marked by the upright arrows in Figure 12 (which indicate where binding begins for the rounded well). Notice that Grünberg's hydrogen data, discussed earlier, is fitted quite well by this theory, using a scattering length of a=.85Å, the value recommended by Legler,[40] who also used Grünberg's data. None of the other data is fitted nearly so well by this theory. Notice however that the pattern of my hydrogen data is roughly that of my helium data, which offers some support to the idea that bubbles were just about ready to form in

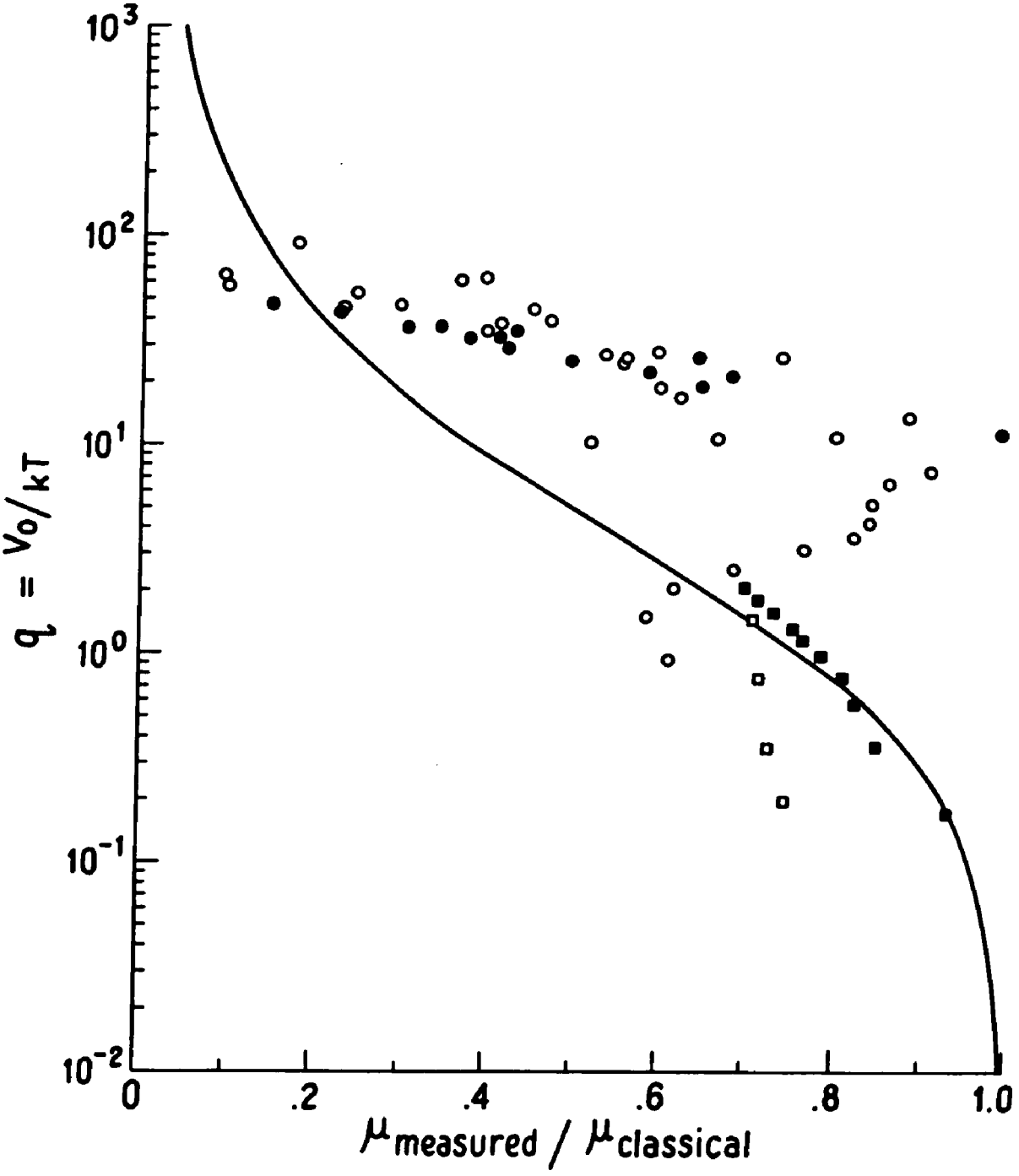

Fig. 35: Solid curve, $I(q) = \int_0^\infty \frac{x^{\nu_1}}{\Gamma(\nu+1)} e^{-x}\, dx$. Open and solid circles--my data for helium and hydrogen, repectively. Open and solid squares--Grünberg's data for helium and hydrogen, respectively.

hydrogen when experimental difficulties prevented going any further.

The prediction of this theory is also shown in Figure 26, for helium-4 at 3.96K, marked $\mu_{\text{Legler theory}}$. Notice first of all that this theory does not predict any sort of collapse or other sort of low mobility behavior as do the Neustadter-Coopersmith and Eggarter-Cohen theories shown in Figure 24. However, it does not yield Young's μ_0 either, as shown in Figure 26.

Thanks are due to L.M. Sander for performing the numerical integration of equation (VII-23) and to B.E. Springett for suggesting comparing the helium and hydrogen data as was done in Figure 35.

LIST OF REFERENCES

1. J.L. Levine and T.M. Sanders, Jr., Phys. Rev. 154, 138 (1967).

2. J.L. Levine, Thesis (University of Minnesota, Minneapolis, Minnesota, 1965).

3. C.G. Kuper, Phys. Rev. 122, 1007 (1959).

4. R.A. Ferrell, Phys. Rev. 108, 167 (1957).

5. B.E. Springett, J. Jortner, and M.H. Cohen, J. Chem. Phys. 48, 2720 (1968).

6. T. Miyakawa and D.L. Dexter, Phys. Rev. 184, 168 (1969).

7. G.K. White, Experimental Techniques of Low Temperature Physics (Clarendon Press, Oxford, 1968, 2nd ed.).

8. A.C. Rose-Innes, Low Temperature Techniques (The English Universities Press, Ltd., London, 1964).

9. P.V.E. McClintock, Phys. Letters 29A, 453 (1968).

10. T.J. Greytak, private communication.

11. J.P. Hernandez and M. Silver, Phys. Rev. A (to be published).

12. R.R. Verderber, J.G. Simmons, and B. Eales, London Philosophical Magazine 16, 1049 (1967).

13. J.G. Simmons and R.R. Verderber, Proc. Roy. Soc. A 301, 77 (1967).

14. R.R. Verderber and J.G. Simmons, Radio and Electronic Engineer 33, 347 (1967).

15. J.G. Simmons, R.R. Verderber, J. Lytollis, and R. Lomax, Phys. Rev. Letters 17, 675 (1966).

16. J.G. Simmons and R.R. Verderber, Applied Phys. Letters 10, 197 (1967).

17. R.A. Cola, J.G. Simmons, and R.R. Verderber, Proceedings of the National Aerospace Electronics Conference (Dayton, Ohio, 1964).

18. J.G. Simmons, "Chapter 14: Electronic Conduction through Thin Insulating Films" in Handbook of Thin Film Technology (McGraw-Hill, New York, 1970).

19. M. Silver, private communication.

20. G.G. Ihas and S.R. Ryan, private communication.

21. Cryogenic Materials Data Handbook, Vol. II, Technical Documentary Report No. AFML-TDR-64-280 (revised) (Air Force Materials Laboratory, Air Force Systems Command, Wright-Patterson Air Force Base, Ohio, 1967).

22. Rose-Innes, op. cit., p. 135.

23. J.E. Kilpatrick, W.E. Keller, and E.F. Hammel, Phys. Rev. 97, 9 (1955).

24. W.H. Keesom, Helium (Elsevier, New York, 1942), p. 49.

25. H.W. Woolley, R.B. Scott, and F.G. Brickwedde, J. Research NBS 41, 379 (1948).

26. H.M. Roder, L.A. Weber, and R.D. Goodwin, NBS Monograph 94; Thermodynamic and Related Properties of Parahydrogen from the Triple Point to 100°K at Pressures to 340 Atmospheres (U.S. Government Printing Office, Washington, D.C., 1965).

27. G.L. Schofield, private communication.

28. J.A. Northby, Thesis (University of Minnesota, Minneapolis, Minnesota, 1966).

29. S. Gunsolo, Nuovo Cimento 21, 2644 (1961).

30. R. Grünberg, Z. Natur. 23, 1994 (1968).

31. J. Lekner, Phys. Rev. 158, 130 (1967).

32. M.H. Cohen and J. Lekner, Phys. Rev. 158, 305 (1967).

33. T.F. O'Malley, Phys. Rev. 130, 1020 (1963).

34. W.F. Schmidt and A.O. Allen, J. Chem. Phys. 52, 4788 (1970).

35. L.B. Loeb, Fundamental Processes of Electrical Discharges in Gases (John Wiley & Sons, New York, 1939), pp. 182-185.

36. P.D. Goldan and L. Goldstein, Phys. Rev. 138, A39 (1965).

37. P.D. Goldan, J.H. Cahn, and L. Goldstein, Electron Interactions in Cryogenic Helium Plasmas, AFCRL-64-67 (Air Force Cambridge Research Laboratories, Office of Aerospace Research, U.S.A.F., Bedford, Massachusetts).

38. R.J. Donnelly, Experimental Superfluidity (University of Chicago Press, Chicago, 1967), pp.214-224.

39. J. Wilks, The Properties of Liquid and Solid Helium (Clarendon Press, Oxford, 1967), p. 666.

40. W. Legler, Phys. Letters 31A, 129 (1970).

41. C.V. Briscoe, S.I. Choi, and A.T. Stewart, Phys. Rev. Letters 20, 493 (1968).

42. L.O. Roellig and T.M. Kelly, Phys. Rev. Letters 18, 387 (1967).

43. W. Triftshauser, J. Legg, A.T. Stewart, and C.V. Briscoe, Proceedings of the Eleventh International Conference on Low Temperature Physics (St. Andrews Printing Department, St. Andrews, Scotland, 1968), p. 304.

44. P.G. Varlashkin, Phys. Rev. A (to be published).

45. H. Schnyders, S.A. Rice, and L. Meyer, Phys. Rev. 150, 127 (1966).

46. L.S. Miller, S. Howe, and W.E. Spear, Phys. Rev. 166, 871 (1968).

47. G. Lepoutre and N.J. Sienko (eds.), Metal Ammonia Solutions (W.A. Benjamin, New York, 1964).

48. E.J. Hart and J.W. Boag, J. Am. Chem. Soc. 84, 4090 (1962).

49. J.W. Johnson and M.A. Bredig, J. Phys. Chem. 62, 604 (1958).

50. R.M. Minday, L.D. Schmidt, and H.T. Davis, Phys. Rev. Letters 26, 360 (1971).

51. B. Halpern and R. Gomer, J. Chem. Phys. 43, 1069 (1965).

52. R.A. Young, Phys. Rev. A 2, 1983 (1970).

53. W.E. Keller, Phys. Rev. 105, 41 (1957).

54. H.E. Neustadter and M.H. Coopersmith, Phys. Rev. Letters 23, 585 (1969).

55. H. Margenau, Phys. Rev. 69, 508 (1946).

56. L.D. Landau and E.M. Lifshitz, Statistical Physics (Addison-Wesley Publishing Company, Reading, Mass., 1958), p. 223.

57. R.C. Clark, Phys. Letters 16, 42 (1965).

58. R.C. Clark, Quantum Fluids: Proceeding of the Sussex University Symposium, 1965, ed. D.F. Brewer (North-Holland Publishing Co., Amsterdam, 1966), p. 337.

59. E.P. Gross, Nuovo Cimento 20, 454 (1961).

60. L.P. Pitaevskii, Soviet Physics JETP 13, 451 (1961).

61. J. Jortner, N.R. Kestner, S.A. Rice, and M.H. Cohen, J. Chem. Phys. 43, 2614 (1965).

62. K. Hiroike, N.R. Kestner, S.A. Rice, and J. Jortner, J. Chem. Phys. 43, 2625 (1965).

63. T.M. Sanders, Jr., private communication.

64. T.P. Eggarter and M.H. Cohen, Phys. Rev. Letters 25, 807 (1970).

65. M.H. Cohen, private communication.

66. S. Dushman, Scientific Foundations of Vacuum Technique, second ed. (John Wiley & Sons, New York, 1966), pp. 30-32.

67. Donnelly, op. cit., pp. 183-196.

68. S. Chandrasekhar, Rev. Mod. Phys. 15, 1 (1943).

69. H.S.W. Massey, Negative Ions (Cambridge Monographs on Physics Series, Cambridge University Press, second ed., 1950), p. 9 and p.27.

70. J.L. Levine and T.M. Sanders, Jr., Phys. Rev. Letters 8, 159 (1962).

71. A.A. Dougal and L. Godstein, Energy Exchange Processes Through Coulomb Collisions in Gaseous Discharge Plasmas Studied by Microwave Interaction Techniques, AFCRC-TN-57-388, ASTIA, Document Number AD-117096.

72. Goldan, Cahn, and Goldstein, op. cit., p. 102.

73. C.L. Zipfel, Thesis (The University of Michigan, Ann Arbor, Michigan, 1969).

74. C.L. Zipfel and T.M. Sanders, Jr., Proceedings of the Eleventh International Conference on Low Temperature Physics (St. Andrews Printing Department, St. Andrews, Scotland, 1968), p. 296.

75. K.W. Schwarz, private communication.

76. I. Modena and F.P. Ricci, Phys. Rev. Letters 19, 347 (1967).

77. R. Cantelli, I. Modena, and F.P. Ricci, Phys. Rev. 171, 236 (1968).

78. R.B. Leighton, Principles of Modern Physics (McGraw-Hill, New York, 1959), p. 518 and pp. 536-539.

79. M.J. Berger and S.M. Seltzer, Tables of Energy Losses and Ranges of Electrons and Positrons (Scientific and Technical Information Division, NASA SP 3012, part of NAS-NRC Pub. 1133), pp. 46-124.

80. J.S. Blakemore, J. Winstel, and R.V. Edwards, Rev. Sci. Inst. 41, 835 (1970).

81. White, op. cit., pp. 367-368.

82. H. Wayland, Differential Equations Applied in Science and Engineering (D. Van Nostrand, Princeton, 1957), pp. 5-7.

83. R.L. Powell and W.A. Blanpied, NBS Circular 556: Thermal Conductivity of Metals and Alloys at Low Temperatures--A Review of the Literature (U.S. Government Printing Office, Washington, D.C., 1954).

84. F.H. Stillinger, Jr. and F.P. Buff, J. Chem. Phys. 37, 1 (1962).

85. L.D. Landau and E.M. Lifshitz, Quantum Mechanics: Non-Relativistic Theory (Addison-Wesley Publishing Company, Reading, Mass., 1958), pp. 69-70 and pp. 108-109.

86. I.I. Gol'dman, V.D. Krivachenkov, V.I. Kogan, and V.M. Galitskii, Problems in Quantum Mechanics (Infosearch Ltd., London, 1950), pp. 64-68.

87. I.S. Gradshteyn and I.M. Ryzhik, Tables of Integrals, Series, and Products (Academic Press, New York, fourth ed., 1965), p. 124 (#2.477 (2)).

88. Ibid., p. 7 (#0.233 (3)).

89. Ibid., p. 1039 (#9.100 and #9.101).

90. Ibid., p. 344 (#3.512 (1)).

91. Ibid., p. 950 (#8.384 (1)).